Spring 2023

NOVEL QUANTUM MATERIALS FOR SPINTRONIC AND OPTO-ELECTRONIC APPLICATIONS

Ali Sarikhani
Missouri University of Science and Technology

Department: Physics

NOVEL QUANTUM MATERIALS FOR SPINTRONIC AND OPTO-ELECTRONIC APPLICATIONS

by

ALI SARIKHANI

A DISSERTATION

Presented to the Graduate Faculty of the

MISSOURI UNIVERSITY OF SCIENCE AND TECHNOLOGY

In Partial Fulfillment of the Requirements for the Degree

DOCTOR OF PHILOSOPHY

in

PHYSICS

2023

Approved by:

Dr. Yew San Hor, Advisor
Dr. Julia Medvedeva
Dr. Amitava Choudhury
Dr. Alexey Yamilov
Dr. Daniel Fischer

PUBLICATION DISSERTATION OPTION

This dissertation consists of the following three articles, formatted in the style used by the Missouri University of Science and Technology:

Paper I: Pages 18-38 have been published in Alloys and Compounds Journal with the title of "*Transparency and room temperature ferromagnetism in diluted magnetic polycrystalline $Zn_{1-x}Cr_xTe$ non-oxide II-VI semiconductor compounds"*, J. of Alloys and Compounds 924, 166478 (2022).

Paper II: Pages 39-57 have been published in Royal Society of Chemistry Advances Journal with the title of "*Chemically induced ferromagnetism near room temperature in single crystal ($Zn_{1-x}Cr_x$)Te half-metal"*, J. of RSC Adv. 13, 8551 (2023).

Paper III: Pages 58-91 have been published in Advanced Functional Materials Journal with the title of "*Self-Intercalation Tunable Interlayer Exchange Coupling in a Synthetic van der Waals Antiferromagnet*", J. of Adv. Func. Mater. 32, 2202977 (2022).

ABSTRACT

Multi-functional quantum materials play a crucial role in the development of spintronics and opto-electronics, as their properties can greatly influence device performance. For instance, in spintronics, materials such as ferromagnetic half-metals, Giant Magnetoresistants (GMR), and magnetic semiconductors have been extensively studied due to their ability to manipulate the spin of electrons for applications in magnetic storage. In opto-electronics, materials such as Diluted Magnetic Semiconductors (DMS) and non-oxide Transparent Conductors (TC) offer advantages such as tunable bandgap and high absorption coefficients, which enable improved device performance.

For this purpose, we have experimentally investigated the compounds that have shown theoretically interesting physical properties. In the current study, we have synthesized, characterized, and studied some novel single crystals and polycrystalline structures of Cr-doped ZnTe, $CrTe_x$, and etc. to explore for the future candidate quantum materials for spintronic and opto-electronic purposes. Cr-doped ZnTe polycrystalline have depicted transparent conductivity as well as room temperature ferromagnetism for both polycrystalline and single crystalline structures. Also, the electrical transport properties of these compounds enhance along with the increase of the dopant (Cr) concentrations. On the other hand, DFT calculations have come to the conclusion of room temperature ferromagnetic half-metallicity for Cr-doped ZnTe monocrystalline. Furthermore, Cr_5Te_8 single crystals have exhibited promising high magnetoresistance up to %10 at low external magnetic field due to their self-intercalated van der Waals structures.

ACKNOWLEDGMENTS

I would like to express my deepest gratitude to my Ph.D. advisor, Dr. Yew San Hor, for his great support and guidance throughout my Ph.D. journey. His insightful feedback and rigorous mentorship have been instrumental in shaping the direction of my research and in enabling me to navigate the various challenges and being an independent researcher.

I am also deeply appreciative of the members of my Ph.D. committee, Dr. Julia Medvedeva, Dr. Amitava Choudhury, Dr. Alexey Yamilov, and Dr. Daniel Fischer for their valuable feedback and constructive criticism, which have greatly improved the quality of my work. Also, I would like to greatly thank my collaborators Dr. J. Medvedeva, Dr. Lily Avazpour, Mr. Mathew Pollard, Dr. A. Choudhury, Dr. Eric Bohannan, and Dr. Ulrich Jentschura for their helps and trainings. Special thanks to the faculty and staff of the Department of Physics and Materials Research Center at Missouri University of Science and Technology, especially Dr. Thomas Vojta and Dr. William Fahrenholtz who have provided me with great academic environments and resources to support my research.

I would like to acknowledge my fellow graduate students, who have become dear friends and who have provided me with a sense of community and camaraderie during the ups and downs of graduate school.

Last but not least, I would like to express my appreciation to my family, for their never-ending love and support throughout my academic journey. I am very grateful to my parents and siblings for their constant encouragement. And special thanks to my loving and supportive fiancé and her family whose faithful support throughout this Ph.D. pursuit is so appreciated.

TABLE OF CONTENTS

Page

LIST OF ILLUSTRATIONS

SECTION Page

PAPER I

PAPER II

PAPER III

NOMENCLATURE

Symbol	Description
E_g	Bandgap energy
α	Absorption coefficient
v	Frequency
h	Planck's constant
χ'	Real component of AC magnetic susceptibility
χ''	Imaginary component of AC magnetic susceptibility

1. INTRODUCTION

Condensed Matter and Materials Physics is a rapidly expanding field that plays a significant role in the development of new technologies. The properties and behavior of materials at the atomic and molecular scale determine their desirability for various applications. By comprehending and manipulating these behaviors, scientists can fabricate new materials with improved performance, helping technology advancements in a wide variety of industries.

Quantum Materials is a subfield of Physics that addresses the study of materials that depict quantum mechanical behaviors, such as semiconductivity, ferromagnetism, optical transparency, half-metallicity, and magnetoresistance. A vast range of technology advancement stems from promising Quantum Materials, as in electronics, data storage, and computing. For example, semiconducting materials play the role as the foundation of many electronic devices such as transistors, diodes, and solar cells. As another example, in the realm of spintronics and data storage, quantum materials have the potential to develop electronic devices by offering new ways to store, process and transfer information [1-4].

Over the past few decades, it has been revealed that materials with combinations of the designated quantum behaviors have inevitable contributions to technology progress such as spintronic purposes and opto-electronic devices. To point out some of the most significant types of these multi-functioning quantum materials, magnetic semiconductors and transparent conductors play an important role in the groundbreaking advances. In this regard, ferromagnetic half-metals and magnetoresistance materials are of great significance for future technology developments [5-10].

1.1. MULTI-FUNCTIONAL QUANTUM MATERIALS

For the purpose of investigating novel quantum materials, a brief review of their concepts and previous studies is necessary. Some of these multi-functional quantum materials are as follows.

1.1.1. Transparent Conductors (TCs). Transparent conductors are materials that have the unique combination of being both optically transparent and electrically conductive, making them ideal for a wide range of applications, from touch screens and displays to solar panels [11-15]. The optical transparency of a material can be measured by its transmittance, i.e., the ratio of incident light that passes through the material. High-transmittance materials allow the light to pass through with little or even no scattering or absorption, which results in good optical clarity.

One of the most commonly utilized types of transparent conductors is Transparent Conductive Oxide (TCO), which is a class of materials that have both high transparency and high electrical conductivity, widely used in various electronic applications such as touch screens, displays, and solar cells. Due to its high ratio of transmission to absorption under light, it is a great candidate as an electrode for optoelectronic devices requiring materials with both electrical conductivity and light transmittance [16-21].

However, these TCOs also have some limitations and downsides such as fragility to mechanical shocks and vulnerability to high temperatures [12], and also low performance of p-type transparent conductors due to the heavy holes in the valence band [21]. On the other hand, chalcogenide-based semiconductors, i.e., sulfides, selenides, and tellurides (group VI compounds except for oxides) with lager band gaps are attracting more

attentions because of their higher p-type concentrations and optical transparency for optoelectronic applications e.g., ZnTe solar cells [23-25, 41].

1.1.2. Magnetic Semiconductors. Magnetic semiconductors are a class of materials that have both magnetic and semiconducting properties, which makes them highly useful for a wide range of applications in electronics and information technology. These types of materials are typically composed of transition metal ions or rare earth elements, doped into a semiconducting host material, such as silicon, gallium arsenide, and zinc telluride. The magnetic properties of these compounds can be controlled by tuning the concentration of magnetic ions or applying an external magnetic field. This makes magnetic semiconductors promising for the applications in magnetic sensors, magnetic memory devices, and spintronics applications, in which the control of magnetic properties is crucial [26-30].

One of the most interesting, widely investigated types of magnetic semiconductors is Diluted Magnetic Semiconductor (DMS), a class of materials that have both magnetic and semiconducting properties, but with a low concentration of magnetic atoms in a semiconducting host structure [31,32]. As shown in Figure 1.1, doping a metal with a relatively high magnetic moment into a non-magnetic semiconductor lattice will result in a DMS structure with ferromagnetic behavior [33,34]. This ferromagnetic property can be measured through the M-H hysteresis loop, i.e., the tendency of a ferromagnetic material to retain some magnetization even after the magnetic field has been removed. Furthermore, the temperature above which a ferromagnetic material undergoes a phase transition and loses its ferromagnetic properties is called the Curie temperature (T_C). This is an important parameter in the study and use of ferromagnetic materials [35].

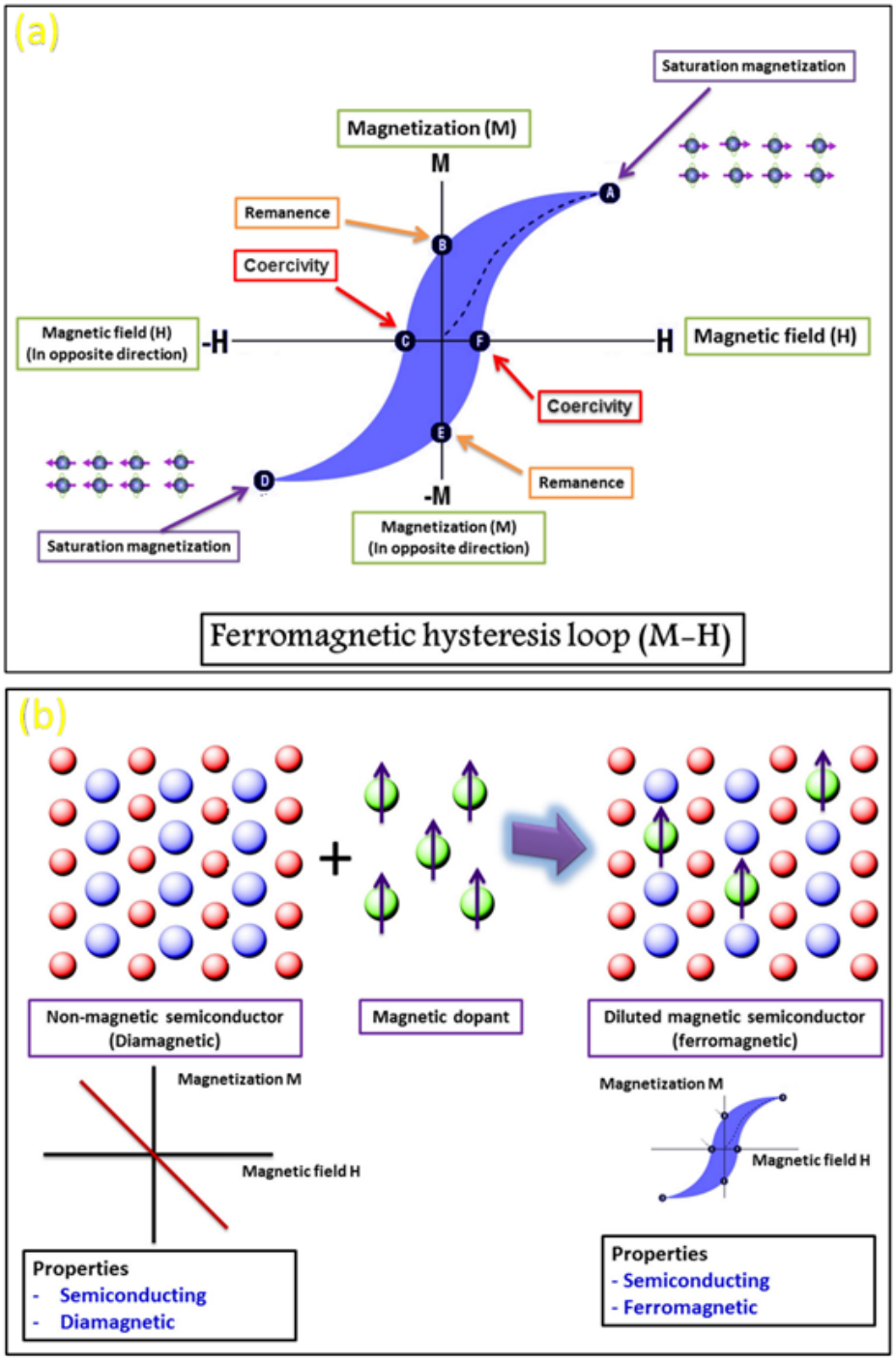

Figure 1.1. Ferromagnetism and Diluted Magnetic Semiconductor (DMS). (a) M-H hysteresis loop for a ferromagnetic material (b) Formation of a Diluted Magnetic Semiconductor (DMS) via doping of a relatively high magnetic moment material into a semiconductor host lattice. Adapted from [35], Jour. of Superconductivity and Novel Magnetism 33, 2557 (2020).

1.1.3. Room-Temperature Ferromagnetic Half-Metal. Room temperature ferromagnetic materials are structures that depict a strong, permanent magnetic moment in the absence of an external magnetic field at or near room temperature. On the other hand, half-metals are materials that have a metallic behavior for one spin channel, and an insulating property for the other, resulting in 100% spin polarization at the Fermi level [36], as depicted on Figure 1.2. The combination of these two properties in a single material has potential applications in spintronics, where the spin of the electrons is used for information storage and processing, as well as in magnetic sensors and magnetic memory devices.

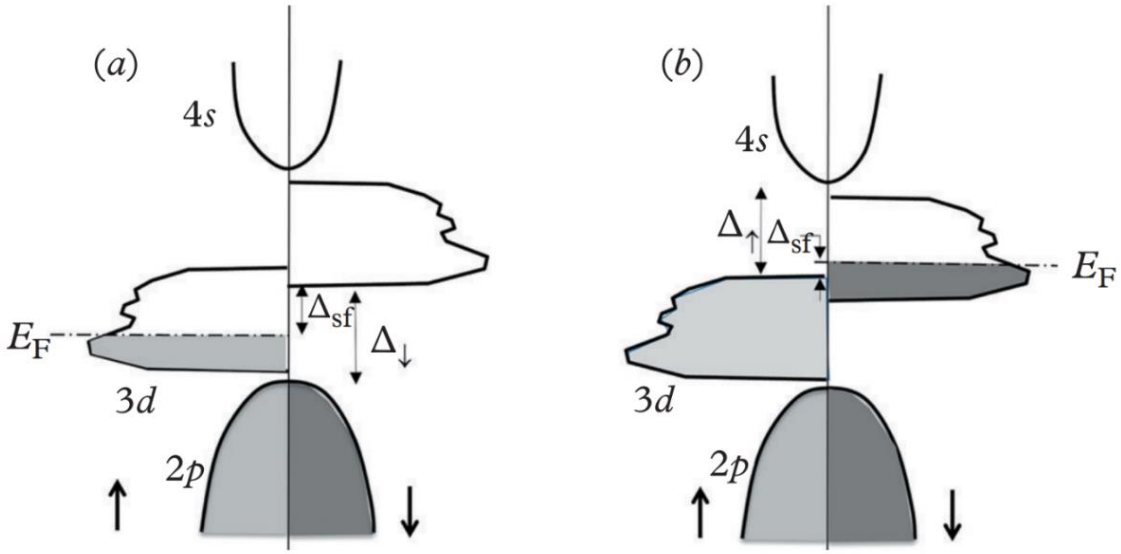

Figure 1.2. Density of states for a two-channel spin representation of a conventional half-metallic ferromagnets. In (a) there are only spin up electrons at E_F, whereas in (b), there are only spin down electrons at E_F. The spin gap is indicated by $\Delta_{\downarrow}$ (or $\Delta_{\uparrow}$) and the spin-flip excitation energy by Δ_{sf}. Adapted from [36], Jour. Phys. D: Appl. Phys., 37, 988 (2004).

1.1.4. Giant Magnetoresistant (GMR). Magnetoresistance is a fundamental property of materials that describes the change in electrical resistance in response to an applied magnetic field. The principle of magnetoresistance is that the magnetic field causes a change in the electronic structure of the material, leading to a change in its resistance.

Giant magnetoresistance (GMR) is a phenomenon that describes a large change in electrical resistance in response to a magnetic field. It is a type of magnetoresistance that has received significant attention in recent decades due to its potential for revolutionizing data storage technology. As exhibited in Figure 1.3, a typical GMR is made of a non-magnetic conductive material being sandwiched between two magnetic materials, either in ferromagnetic state (FM) or antiferromagnetic (AFM). The basic principle of GMR is that the magnetic field causes a change in the alignment of the magnetic layers in a multi-layered material, leading to a change in its electrical resistance [37]. In this case, an incoming electron with one of the two spin channels (up or down) can be scattered depending on its own spin and the magnetic layer spin polarization, shown in Figure 1.3.

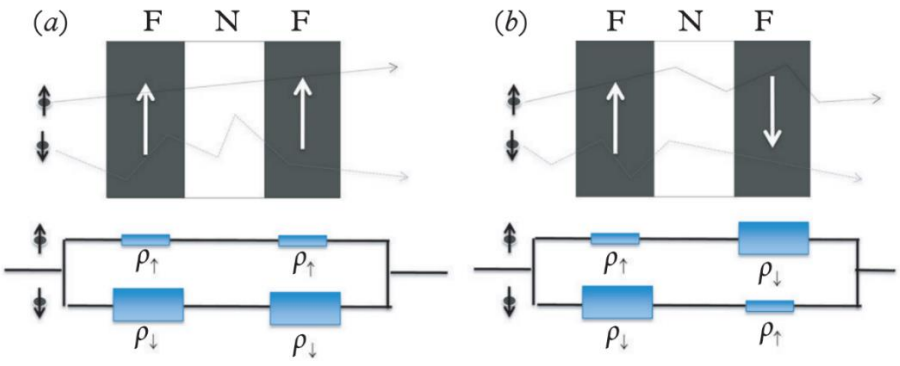

Figure 1.3. A simple resistor network model for GMR. (a) Parallel alignment of the two ferromagnetic layers. (b) antiparallel alignment. Adapted from [37], Fundamentals and Applications of Magnetic Materials by K. M. Krishnan, Oxford University Press (2016).

1.2. EXPERIMENTAL SYNTHESIS OF SINGLE CRYSTALS

Single crystal synthesis techniques are methods used to grow a homogeneous monocrystalline from a solution or melt or solid state. The goal of single crystal synthesis is to produce a well-defined and uniform monocrystal structure, composition, and orientation. Single crystals have unique physical and chemical properties compared to polycrystalline materials, which are made up of many small, randomly oriented crystals. This makes single crystals valuable for a wide range of applications, including electronic devices, optical materials, and catalysts.

The process of single crystal synthesis is often challenging, as it requires precise control over temperature, pressure, composition, and other conditions to produce a single crystal with the desired properties. There are several methods for single crystal synthesis, including Modified Bridgman method, Solid State Reaction, and Chemical Vapor Transport (CVT). The choice of method depends on the material being synthesized, the desired size and shape of the crystal, and the desired purity.

1.2.1. Modified Bridgman Method. The modified Bridgman method is a crystal growth technique used to produce high-quality single crystals from a wide range of materials, including metals, semiconductors, and ceramics. This method involves heating a material in a sealed container and then slowly cooling it to cause it to solidify into a single crystal. The crystal is grown along the length of the quartz tube as it is being withdrawn, and the temperature gradient is carefully controlled to ensure that the material solidifies in a controlled manner, with no defects or impurities. Figure 1.4 indicates different steps of the modified Bridgman process, during which it is necessary to keep the sample clean and avoid mixing with any moisture.

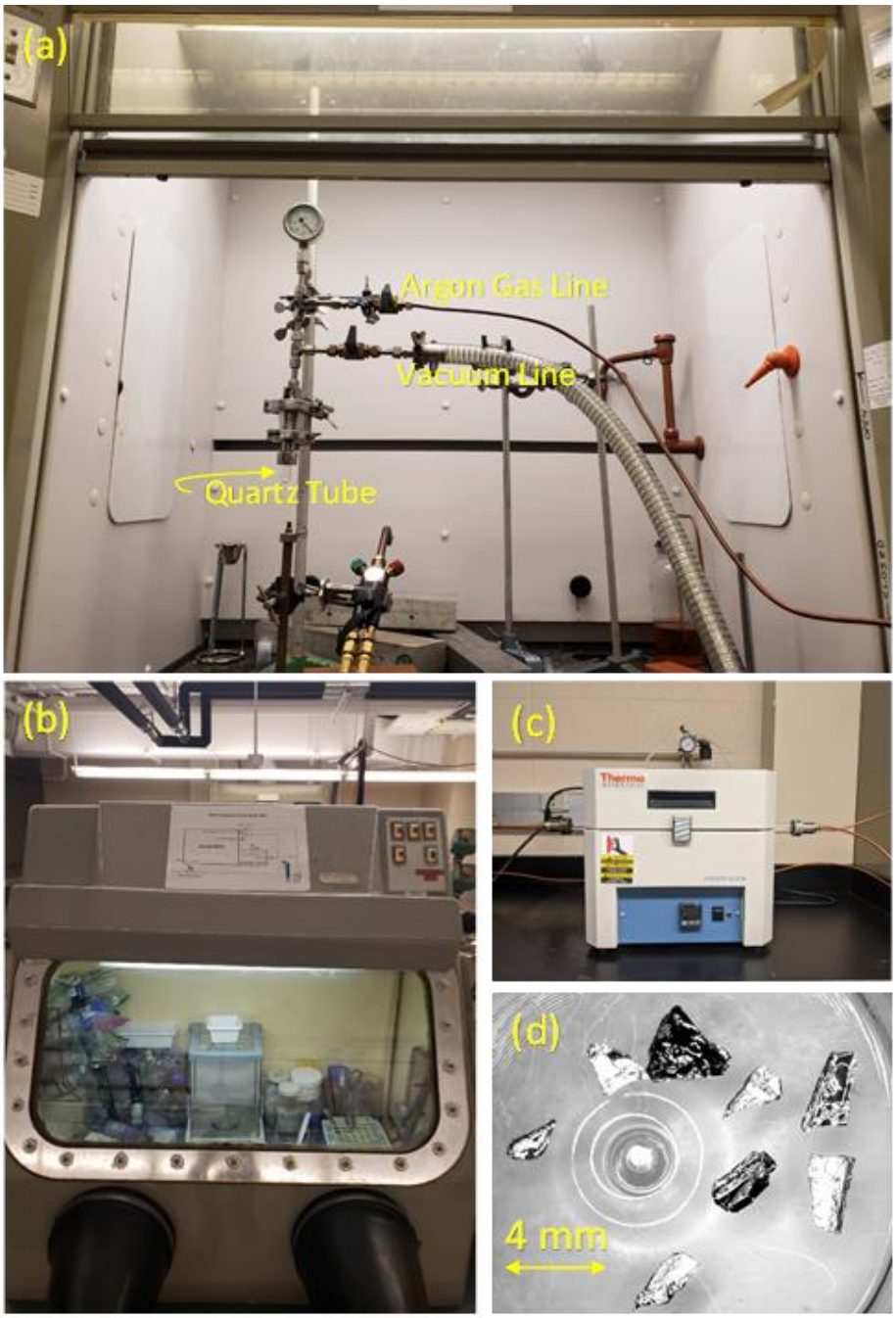

Figure 1.4. Modified Bridgman Method Process. (a) Vacuum sealing setup using a methane-oxygen blow torch and Argon flow. (b) Clean glove box for weighing and grinding high-purity materials. (c) Tube furnace with an Argon line. (d) Cr_5Te_8 single crystals grown using modified Bridgman method.

1.2.2. Solid State Reaction. Solid-state reactions can also play a crucial role in the crystal growth of materials. In crystal growth, atoms or ions assemble into a highly ordered arrangement to form a single crystal. The process of crystal growth can be divided into two main stages: nucleation and growth.

In the nucleation stage, a small number of atoms or ions come together to form a nucleus, which serves as the seed for further crystal growth. The nucleation process is often the rate-limiting step in crystal growth and can be influenced by various factors, including the purity and composition of the starting materials and the conditions under which they are mixed. In the growth stage, the nucleus grows by the addition of more atoms or ions to the surface of the crystal. This stage can also be influenced by various factors, including the temperature, pressure, and concentration of the reactants, as exhibited in Figure 1.5.

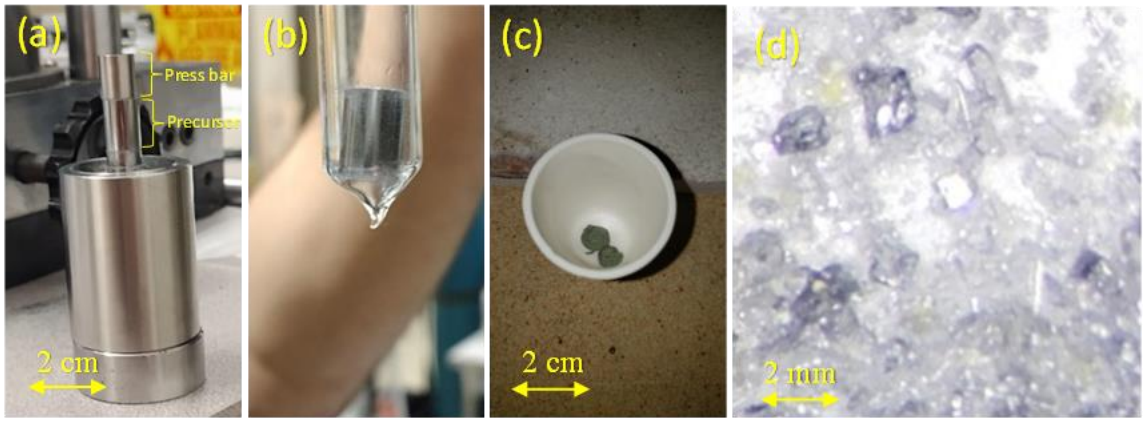

Figure 1.5. Solid State Reaction Process. (a) Dies set with a Yb_2MoO_6 pellet on top ready to vacuum seal. This sample has been pressed under 10 MPa for 15 min. (b) Yb_2MoO_6 pellet sealed inside a quartz tube to provide a precursor via annealing at 1100 °C for 24 hours. (c) Annealed precursor in an Alumina crucible at 1400 °C for 36 hours. (d) Colorless polycrystalline Yb_2MoO_6 can be seen with the size of <1mm. The optical transparency of these single crystals concludes relatively large optical bandgaps of orders of 3-4 eV.

1.2.3. Chemical Vapor Transport (CVT). Chemical vapor transport (CVT) crystal growth is a technique used for the growth of single crystals, where a material is transported from a source to a growth region by a carrier gas. In CVT, the source material is typically placed in a high-temperature zone, and a reactive gas, such as iodine, bromine, or an organic compound, is introduced into the chamber to transport the source material to the growth region, where the single crystal is formed.

The process of CVT crystal growth is driven by the vapor pressure difference between the source and growth regions. The material evaporates from the source and reacts with the carrier gas to form a volatile complex, which is then transported to the growth region, where it condenses to form a single crystal.

CVT crystal growth has several advantages over other crystal growth methods, including the ability to grow large, high-quality single crystals, the ability to grow single crystals of materials that are difficult to grow by other methods, and the ability to control the composition and doping of the single crystals.

The CVT procedure includes preparing a homogeneous precursor using modified Bridgman method or other techniques, inserting the transport agent (like Iodine chunks) on the precursor, and then vacuum-sealing the quartz tube for annealing. Iodine weight is dependent on the size of the ampule and can be of orders of $3mg/cm^3$ in order to provide a sufficient amount of mobility for the precursor crystallization. As depicted in Figure 1.6, the measured temperature profile shows the desired positions of the precursor and the nucleation at the hot and cold zones, respectively, i.e., the peak and the trough of the temperature profile graph.

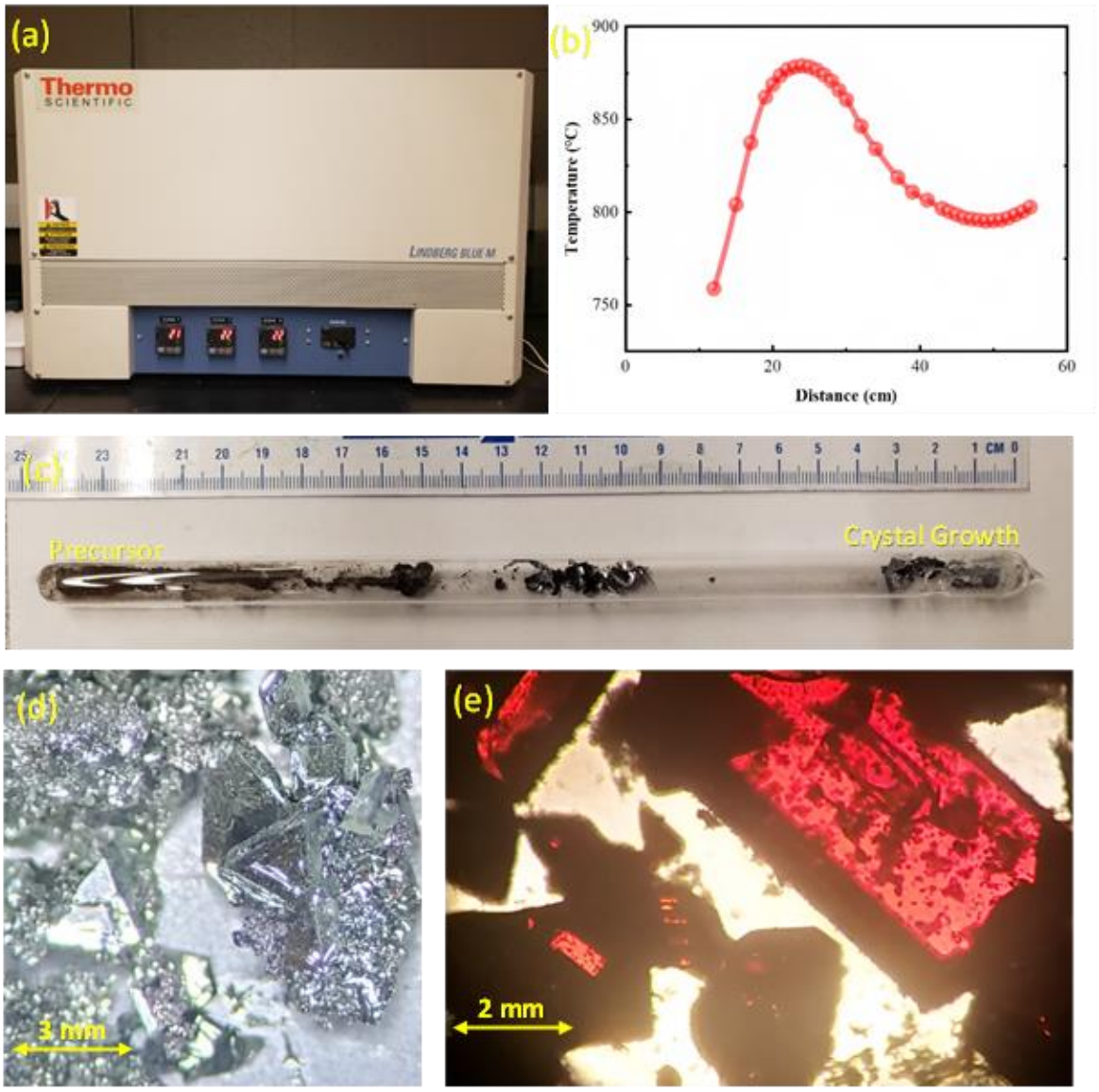

Figure 1.6. Chemical Vapor Transport Process. (a) 3-zone furnace. (b) A typical temperature profile for a 3-zone furnace measured using long thermocouple rod at each position inside the furnace, where the zones were set at 900, 600, and 850 °C. (c) CVT-grown single crystals. As shown, the precursor has been transported and crystalized at the colder zones using Iodine as the transport agent. (d) Transparent $Zn_{0.8}Cr_{0.2}Te$ single crystals grown using CVT. (e) Transparent ZnTe single crystals grown using CVT.

1.3. CHARACTERIZATION AND MEASUREMENT

1.3.1. X-Ray Diffraction (XRD). X-ray diffraction (XRD) is a non-destructive analytical technique used to determine the crystal structure of a material. It is based on the interaction between X-rays and matter, and the resulting diffraction patterns, determining the arrangement of atoms within a crystal. In XRD, a material is exposed to X-rays, which interact with the atoms within the material, causing the X-rays to diffract in a characteristic pattern. The diffracted X-rays are then collected and analyzed to determine the crystal structure of the material [38]. XRD can be used to identify the crystalline phase of a material, determine its crystal structure, and quantify the amount of each phase present. As demonstrated in Figure 1.7, the angle between the incident and the diffracted photon is 2θ. The photons reflecting from the top layer of the crystal and the next layer can interfere with each other constructively, or destructively. The equation shown in Figure 1.7(b), i.e., Bragg's diffraction relation, satisfies the constructive interference.

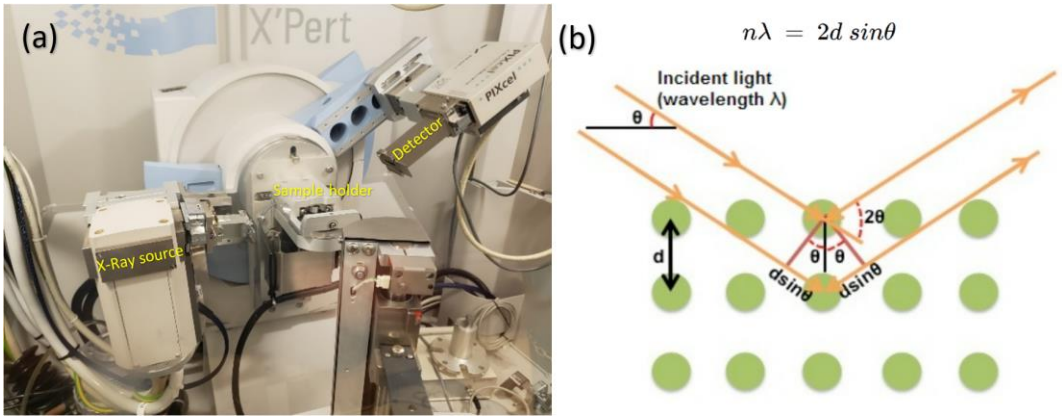

Figure 1.7. X-Ray Diffraction (XRD). (a) A typical powder XRD machine. (b) Schematic of Bragg's diffraction and the formula used for XRD data refinement, where d is the spacing between crystal layers as shown and n is an integer, adapted from [38].

1.3.2. Physical Property Measurement System (PPMS). A Physical Property Measurement System (PPMS) is an experimental platform used to measure various physical properties of materials. PPMS systems are commonly used in the fields of materials science, condensed matter physics, and nanotechnology, to study the behavior of materials at the micro- and nanoscale.

PPMS systems typically use a combination of experimental techniques, including magnetic, electrical, and thermal property measurements, to study the properties of materials over a wide range of temperatures and magnetic fields. The properties that can be measured using a PPMS system include:

- Magnetic properties, such as susceptibility, magnetization, and magnetic ordering
- Electrical properties, such as conductivity, resistivity, and Hall effect
- Thermal properties, such as specific heat and thermal conductivity
- Mechanical properties, such as elastic modulus, hardness, and tensile strength

PPMS utilizes liquid nitrogen and liquid helium to obtain very low temperatures (~ 2K) and simultaneously, it is capable of varying the external magnetic field applied on the sample up to 9 T. A schematic of the sample chamber and the probe in a typical PPMS is depicted in Figure 1.8 (a). The probe is immersed in the liquid-helium bath inside the dewar. A sophisticated device with delicate components, the probe incorporates the basic temperature-control hardware, the superconducting magnet, the helium-level meter, the gas lines, the sample puck connectors, and various electrical connections. The probe is composed of several concentric stainless-steel tubes and other important elements. Its outer layer isolates the sample chamber from the liquid-helium bath.

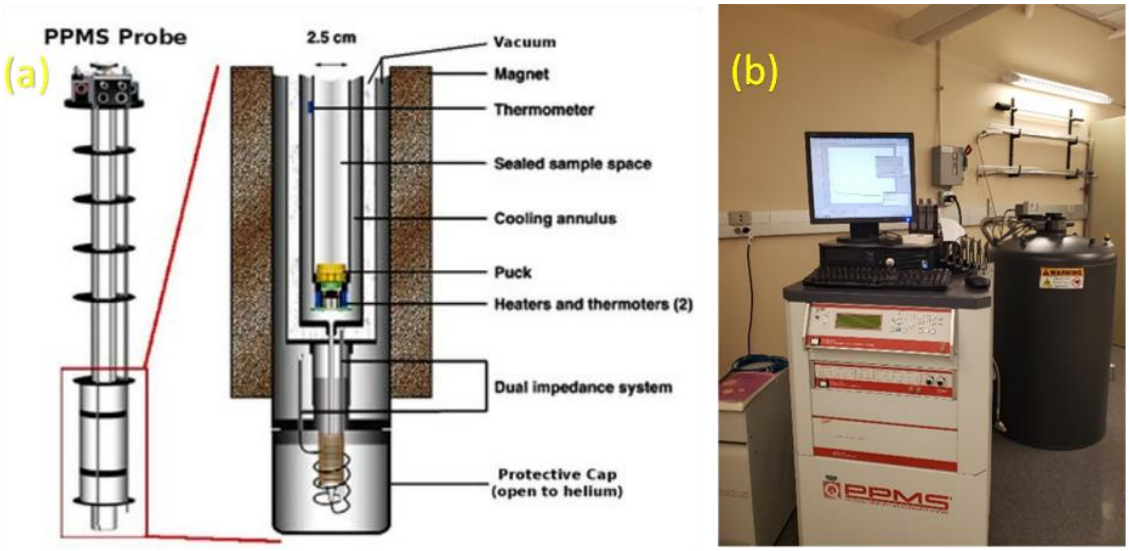

Figure 1.8. Physical Property Measurement System (PPMS). (a) Schematic of the sample chamber setup and PPMS probe. (b) PPMS tank of liquid nitrogen and liquid helium (right) and the vacuum pump (left).

1.3.3. UV-Visible Absorption Spectroscopy and Tauc Plots. UV-Visible Absorption Spectroscopy is a technique used to determine the absorption spectra of a substance in the ultraviolet (UV) and visible regions of the electromagnetic spectrum. The technique is based on the measurement of the amount of light absorbed by a sample at different wavelengths. Furthermore, this technique is utilized in some cases to measure the transmittance and reflectance of a sample.

In UV-Visible Absorption Spectroscopy, a sample is exposed to a beam of light in the UV or visible regions of the spectrum. Some of the light is absorbed by the sample, and the remaining light is detected by a detector. The amount of light absorbed by the sample is then measured as a function of wavelength, and the resulting absorption spectrum is plotted.

UV-Visible Absorption Spectroscopy is also advantageous for the calculation of the optical bandgap of a material using Tauc's relation [39] defined as

$$(\alpha h\nu)^2 = A\left(h\nu - E_g\right), \quad (1)$$

where α is the absorption coefficient, $h\nu$ is the energy of the incident photon, A is the proportionality constant, and E_g is the bandgap energy. To find E_g from the UV-vis. Data, the linear extrapolation of the left side of this equation will have an x-intercept equal to the optical bandgap. Furthermore, the power of the left side of this equation (in this case: 2) can vary depending on the type of the electron transition. For a direct allowed transition, an indirect allowed transition, a direct forbidden transition, and an indirect forbidden transition, it is equal to 2, 1/2, 2/3, and 1/3, respectively.

1.3.4. Neutron Diffraction. Neutron diffraction is a powerful analytical technique used to determine the crystal structure of materials. It is based on the interaction of neutrons with the atomic nuclei of a sample, which results in the scattering of the neutrons. The scattered neutrons can then be detected and used to determine the crystal structure of the sample.

Neutron diffraction is particularly useful for the study of materials that are difficult to study using other techniques, such as X-ray diffraction. For example, neutron diffraction can be used to study materials that have light atoms, such as hydrogen, which are difficult to detect using X-rays. Neutron diffraction can also be used to study materials that are sensitive to radiation damage, such as organic materials, which can be damaged by X-rays.

In neutron diffraction, a beam of neutrons is directed at a sample, and the resulting scattered neutrons are detected using a neutron detector. The pattern of scattered neutrons can then be used to determine the crystal structure of the sample. The information obtained

from neutron diffraction can be used to study the structure of materials at the atomic and molecular level, and to understand their physical and chemical properties [40].

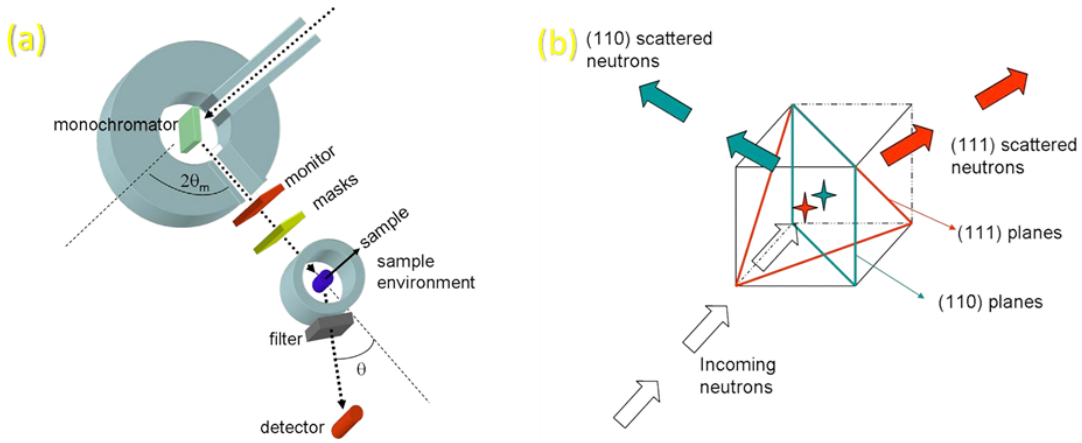

Figure 1.9. Neutron Scattering. (a) A schematic representation of a 3-axis neutron spectrometer. (b) Schematic depiction of a crystal orienting with a high symmetry direction parallel to the incoming beam. Adapted from [40], Practical Neutron Scattering at a Steady State Source by T. Heitmann and W. Montfrooij, Mizzou Media Press (2012).

As indicated in Figure 1.9 (a), The first axis is where the monochromator crystal is placed on, then the sample is on the second axis, and the analyzer crystal is located on the third axis. The purple line shows the path of the neutron that is being detected. Figure 1.9 (b) schematically depicts a crystal orienting with a high symmetry direction parallel to the incoming beam. The different sets of lattice planes select a neutron wavelength out of a white beam and diffract it at the corresponding Bragg angle. This figure shows neutrons coming in (open arrows) parallel to the a-axis and being diffracted by the (110) planes (green and green arrows), and by the (111) planes (red, red arrows).

For the purpose of magnetic study of different structures, neutron scattering can be performed using a spin-polarized monochromatic incident neutron beam. In this case, the

spin state of the incident neutron will interact with the spin structure of the sample and will scatter off of the sample in different direction based upon the momentum change of the beam. These diffracted beams of neutron can be counted in different directions on a target screen of many detectors. For instance, a ferromagnetic structure tends to scatter most of the incident spin-polarized beams in a specific direction, which demonstrates a robust magnetic order in that specific plane direction.

PAPER

I. TRANSPARENCY AND ROOM TEMPERATURE FERROMAGNETISM IN DILUTED MAGNETIC POLYCRYSTALLINE $Zn_{1-x}Cr_xTe$ NON-OXIDE II-VI SEMICONDUCTOR COMPOUNDS

Ali Sarikhani [a,e,*], Laleh Avazpour [b], Wipula Liyanage [c], Raul Florez [d], Eric Bohannan [e], Dave Satterfield [c], Manashi Nath [c], Julia E. Medvedeva [a], Yew San Hor [a,e,*]

[a] Department of Physics, Missouri University of Science and Technology, Rolla, MO 65409, USA

[b] Department of Electrical and Computer Engineering, University of Wisconsin-Madison, 1415 Engineering Dr., Madison, WI 53706, USA

[c] Department of Chemistry, Missouri University of Science and Technology, Rolla, MO 65409, USA

[d] Department of Nuclear Engineering, Missouri University of Science and Technology, Rolla, MO 65409, USA

[e] Materials Research Center, Missouri University of Science and Technology, Rolla, MO 65409, USA

* Corresponding author

Keywords: Cr-doped ZnTe, Half metal, Room temperature ferromagnetism, Non-oxide transparent conductor, ZnCrTe, Spintronics, Diluted magnetic semiconductor (DMS), Transition Metal Dichalcogenide (TMD).

ABSTRACT

Polycrystalline $Zn_{1-x}Cr_xTe$ samples for x = 0.00, 0.05, 0.10, 0.15, 0.18, and 0.20 were synthesized by solid-state reaction, and their physical properties were studied for the purpose of identifying a novel non-oxide transparent diluted magnetic semiconductor

(DMS). Their transport properties exhibit semiconducting behavior for low Cr concentrations and become conductors for higher Cr concentrations. Ferromagnetic behavior was observed in Cr-doped ZnTe with Curie temperature T_C increasing as Cr concentration increases. At x = 0.20 Cr concentration, the system has T_C above room temperature, indicating an interesting II-VI ferromagnetic semiconductor. Furthermore, optical transparency in the visible light range was found to be 30–85 % for different Cr concentration concentrations. Also, according to the electrical transport measurement data in this study, the resistivity doesn't exhibit any significant change as the temperature increases for x = 0.20. This consistent resistivity exhibits a possible candidacy for further studies of the sample $Zn_{0.80}Cr_{0.20}Te$ for half-metallic ferromagnetic properties.

1. INTRODUCTION

Interesting characteristics of materials such as semiconductivity, room temperature ferromagnetism and transparency are of great importance in technology advancement [1–4]. In this regard, materials with combinations of the designated properties are getting attention for the purpose of spintronics and data storage devices [5–10]. One of the ground-breaking types of these multi-functioning materials is transparent conducting oxides (TCOs), which are structures of optically transparent and electrically conductive material. These structures play an important role in many electronic devices e.g., touchscreens, liquid-crystal displays, OLEDs, and photovoltaics [11–21]. These types of oxides have a high ratio of transmission to absorption under light, which makes them a great candidate as electrodes for optoelectronic devices requiring materials with both electrical

conductivity and light transmittance [19]. One of the major drawbacks with TCOs is the low performance of p-type transparent conductors, which results from the heavy holes in the valence band due to localized p states of oxygen [21]. Also, TCO glasses are fragile and vulnerable to high temperatures [12]. However, large band gap semiconductors such as chalcogenides (sulfides, selenides, and tellurides) are interesting, less investigated materials due to their tendencies for p-type concentration and wide applications in optoelectronic devices e.g., ZnTe solar cells [49]. The previous studies address a suite of compounds including different combinations of II group cations (Zn, Cd, and Hg) and VI-group anions (S, Se, and Te), whose applications in magneto-optical devices have been investigated [23–25]. Moreover, Cr-doped II-VI DMS, as one of the most highlighted DMS due to the ferromagnetic behavior reported by experiments and calculations [26–32], has exhibited the ferromagnetic transition around room temperature for thin films [33,34]. For this purpose, there has been a great deal of attention on the structure of $Zn_{1-x}Cr_xTe$ thin films [35–41]. So far, there has not been any UV–Visible transparency report of Cr-doped ZnTe single crystals or polycrystalline structures. However, the crystalline bulk structure of $Zn_{1-x}Cr_xTe$ has been claimed to have ferromagnetic characteristic at room temperature for $x = 0.05$ [22,42]. Furthermore, there has been a great deal of attention on the transparency of the oxide semiconductors as the host of DMS [43], but there has been a lack of optical transparency in chalcogenides of DMS. Developing optically transparent magnets at room temperature will result in a great deal of progress in different industries, not only for electronic and magnetic devices but also for optical applications [48]. Based on room temperature ferromagnetism as well as favorable memory effect of fabricated devices, these structures could be a potential material for future spintronic nano-devices

and opto- electronics. Nonetheless, by clearly showing this ferromagnetic semiconductivity, the results of transparency probably open up an unexpected and important new direction for optical spintronics research in DMSs. Magnetic materials in electric devices are not optically transparent. With the synthesis of a transparent magnet, more advanced display devices will be innovated. As an example, speed and fuel meters and a map can be displayed directly on the front glass of a car or an airplane. In the present work, we have investigated $Zn_{1-x}Cr_xTe$ with x = 0.00, 0.05, 0.10, 0.15, 0.18, and 0.20 for identifying a novel non-oxide transparent DMS with the purpose of playing a role in interdisciplinary materials science and future spintronics and opto-electronics. Transparent $Zn_{1-x}Cr_xTe$ bulks in the visible region are required in applications with optoelectronics. Also, according to the electrical transport data in this study, the resistivity does not exhibit any significant change as the temperature increases for x = 0.20. This flat resistivity can be a possible candidate for further studies of the sample $Zn_{0.80}Cr_{0.20}Te$ for half-metallic ferromagnetic properties.

2. EXPERIMENTAL

Polycrystalline samples of $Zn_{1-x}Cr_xTe$ with x = 0.00, 0.05, 0.10, 0.15, 0.18, and 0.20 were synthesized using high-purity Zn (99.99%), Te (99.999%) and Cr (99.99%) powders (Alfa Aesar). The reactant powders were stoichiometrically mixed to the desired ratio. The mixed powders were ground using mortar and pestle for about 30 min and then pressed into pellets (~ 2 g) for solid state reaction. Each pellet was vacuum sealed in a 10 cm diameter quartz ampoule. For the synthesis of the ZnTe sample, the quartz ampoule

containing the ZnTe pellet was gradually heated up at the rate of 1 °C/min to 950 °C and kept at the temperature for 24 h. The $Zn_{1-x}Cr_xTe$ samples with $x > 0$ were heated up to 1100 °C at the same heating rate and sintered at the temperature for 24 h. After the first sintering, the samples were slowly cooled at 1 °C/min down to room temperature. The samples were then ground into powders and compressed into pellets and vacuum-sealed in quartz ampoules separately for the second sintering at 950 °C (for ZnTe) and 1100 °C (for $Zn_{1-x}Cr_xTe$ samples with $x > 0$) for 48 h. This resulted in polycrystalline samples ZnTe and Cr-doped ZnTe with dark orange and black color, respectively. Crystal structure of $Zn_{1-x}Cr_xTe$ was characterized by using PANalytical X'Pert Multi-purpose Diffractometer with Cu source of $\lambda = 0.15418$ nm with minimum step size of $2\theta = 0.026°$. To realize the atomic rearrangement and dopant location in the ZnTe host lattice, Room temperature Raman Spectra were performed by using HORIBA Jobin Yvon LabRAM ARAMIS Micro Raman Spectrophotometer of 10 mW and $\lambda = 532$ nm. Quantum Design Physical Property Measurement System (PPMS) was used to measure the temperature dependence of electrical resistivity and magnetic properties of the polycrystalline $Zn_{1-x}Cr_xTe$ samples in the temperature range of 2–300 K. For resistivity measurement, the samples were cut into $1 \times 1 \times 4$ mm^3 rectangular shape. Room temperature cured silver paste was used for the four-probe resistivity contacts. DC magnetization measurements were performed using the PPMS. Zero-field cooled (ZFC) magnetization measurements under an applied magnetic field of 5 kOe were performed in the temperature range of 5–300 K. A Cr-doped sample $Zn_{1-x}Cr_xTe$ was first cooled to 5 K from room temperature at zero applied field. Then, the temperature dependent magnetization of the sample was measured at 5 kOe applied field in the warming trend from 5 K to 300 K. Optical transmission of $Zn_{1-x}Cr_xTe$ was measured

using a Varian Cary®50 UV–Vis Spectrophotometer (0.25–0.85 lm) with Dual Beam and scan rates up to 24,000 nm/min. The transmittance was measured in the mid-infrared to ultraviolet range (200–800 nm). For the optical transmittance measurements, each polycrystalline $Zn_{1-x}Cr_xTe$ sample (x = 0.00, 0.05, 0.10, 0.18, and 0.20) was pulverized into powder form and suspended in ethylene glycol. The blank, in this case, is a UV transparent cuvette (quartz), filled with the same solvent (ethylene glycol) used for suspending the polycrystalline sample powders. First, the transmittance of ethylene glycol was measured and set as the background, then the transmittance was measured for the polycrystalline $Zn_{1-x}Cr_xTe$ powder in the solvent. The transmittance spectra of the polycrystalline $Zn_{1-x}Cr_xTe$ samples were obtained automatically by subtracting the measured results from the spectrum of the solvent.

3. RESULTS AND DISCUSSION

The powder x-ray diffractions of $Zn_{1-x}Cr_xTe$ with x = 0.00, 0.05, 0.10, 0.15, 0.18, and 0.20 are shown in Figure 1(a). All the main peaks are corresponding to the Zincblende (cubic) structure. A schematic view of the Zincblende structure including a substitutional Cr for Zn atoms is shown in Figure 1(b). Powder XRD measurements are done up to a high 2-theta angle (138°) to improve the accuracy of our lattice parameter determination. The error bars shown are derived from the ESD given after Rietveld refinement of each pattern. Figure 1(c) indicates the Cr concentration dependence of the lattice parameters *a*, *b*, or *c*, where $a = b = c$ due to the cubic structure of the materials. These parameters were obtained by using the Rietveld refinement method. The lattice parameters can be calculated up to 5

or 6 decimal places in Angstrom using Rietveld refinement method [50–52]. According to Figure 1(c), the lattice parameter shows a monotonic change along with Cr concentration, which is due to the different effective ionic radii of Zn^{2+} and Cr^{3+}. Based on the structure shown in Figure 1(b) and the coordination numbers of Zn^{2+} and Cr^{3+} in this lattice, the effective ionic radii of Zn^{2+} and Cr^{3+} are 0.60 Å (with a coordination number of IV) and 0.615 Å (with a coordination number of VI), respectively [53]. Therefore, it is expected that the lattice parameter slightly increases as the Cr concentration increases in the host lattice. As the structures of the polycrystals are characterized by XRD, Raman spectroscopy is the next method to confirm the substitution of Cr atoms in ZnTe lattice. Room temperature Raman experiment was performed to determine the chemical composition and structure of the polycrystalline $Zn_{1-x}Cr_xTe$ samples. Figure 2 shows the Raman scattering effect of the polycrystalline $Zn_{1-x}Cr_xTe$ samples in the range of 100–600 cm^{-1}. The Raman spectra were registered across four different spots identified using a 100x objective lens integrated with the Raman spectrophotometer.

The intense vibrations in the range of 120–140 cm^{-1} suggest the existence of Te-rich phases in all the samples. The first and second order longitudinal optical phonon modes (1LO and 2LO) corresponding to ZnTe are weakly evolved at ~ 215 and ~ 425 cm^{-1}. Convincingly, their peak positions also appeared to be red shifted by the increase of more concentration Cr into the host structure ZnTe. Therefore, according to Raman data and the lattice parameters from XRD data, the substitution of Cr in ZnTe lattice in the polycrystalline samples of $Zn_{1-x}Cr_xTe$ has been confirmed.

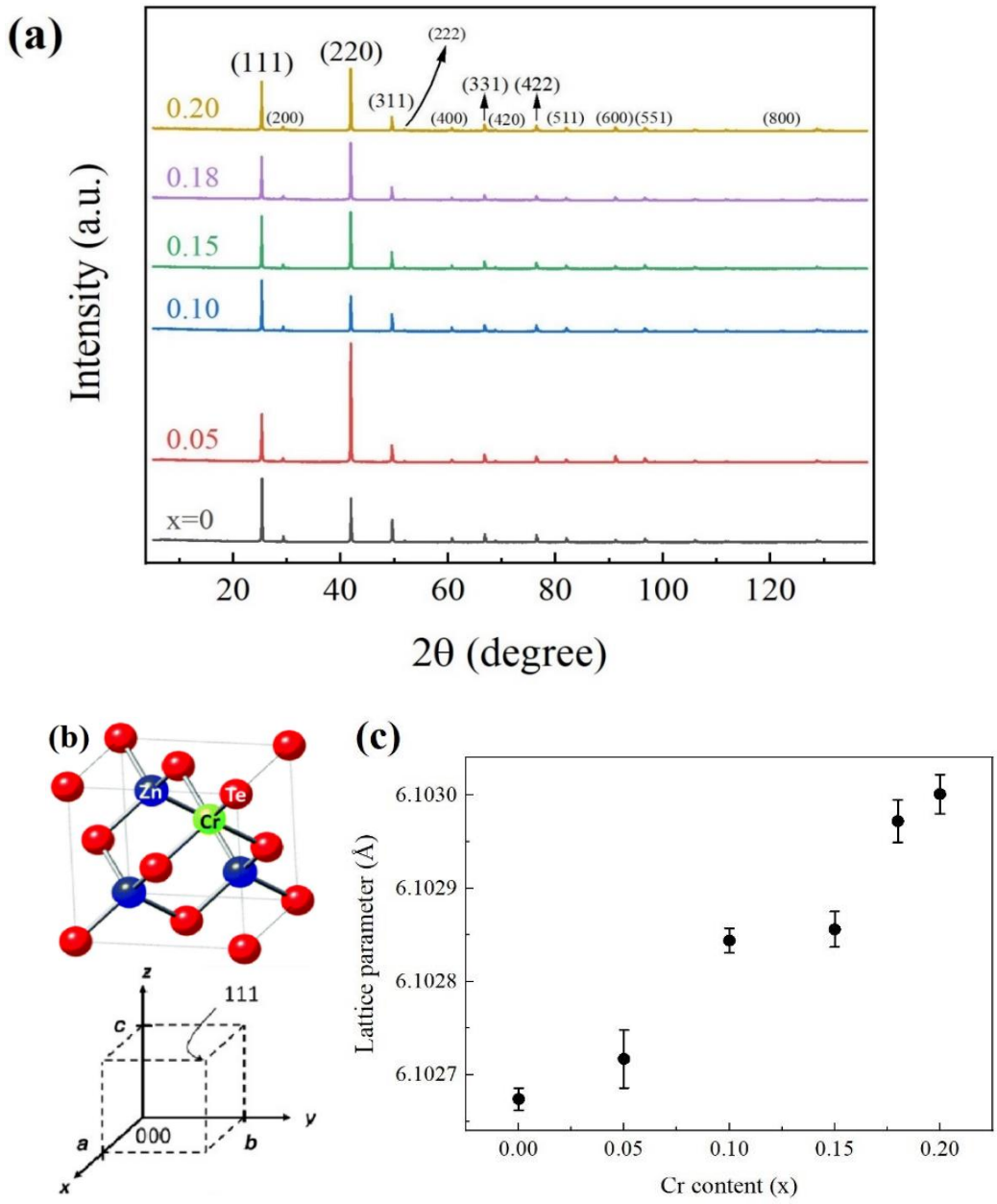

Figure 1. Crystal structure characterization of polycrystalline $Zn_{1-x}Cr_xTe$ samples for x = 0.00, 0.05, 0.10, 0.15, 0.18, and 0.20. (a) Powder x-ray diffraction for $Zn_{1-x}Cr_xTe$ (stacked with steps for easy comparison). (b) Crystal structure of $Zn_{1-x}Cr_xTe$ with *a*, *b*, and *c* parameters shown. (c) Lattice parameter (*a*, *b*, or *c*) vs. Cr concentration, x, for $Zn_{1-x}Cr_xTe$. ((b) Source: *Nanoscale, 2014, 6, 14667*).

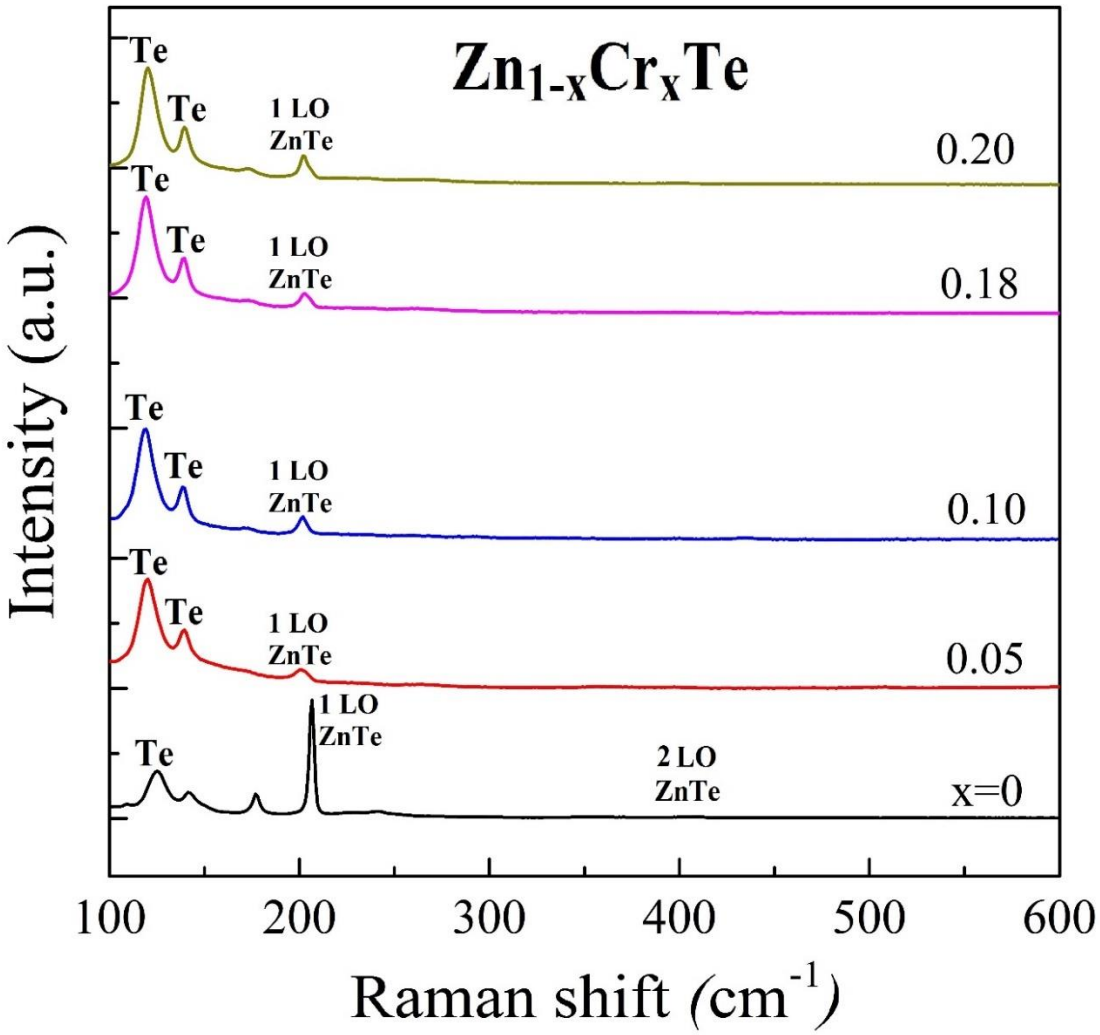

Figure 2. Raman spectra of polycrystalline $Zn_{1-x}Cr_xTe$ at room temperature for x = 0.00, 0.05, 0.10, 0.18, and 0.20 (stacked with steps for easy comparison).

Figure 3 shows the resistivity of the polycrystalline $Zn_{1-x}Cr_xTe$ samples (for x = 0.00, 0.05, 0.15, 0.18, and 0.20) as a function of temperature. Undoped ZnTe has resistivity of 2 × 105 Ωcm at room temperature. Its resistivity increases with decreasing temperature verifying that the polycrystalline $Zn_{1-x}Cr_xTe$ samples with x = 0.00, 0.05 and 0.15 are semiconductor.

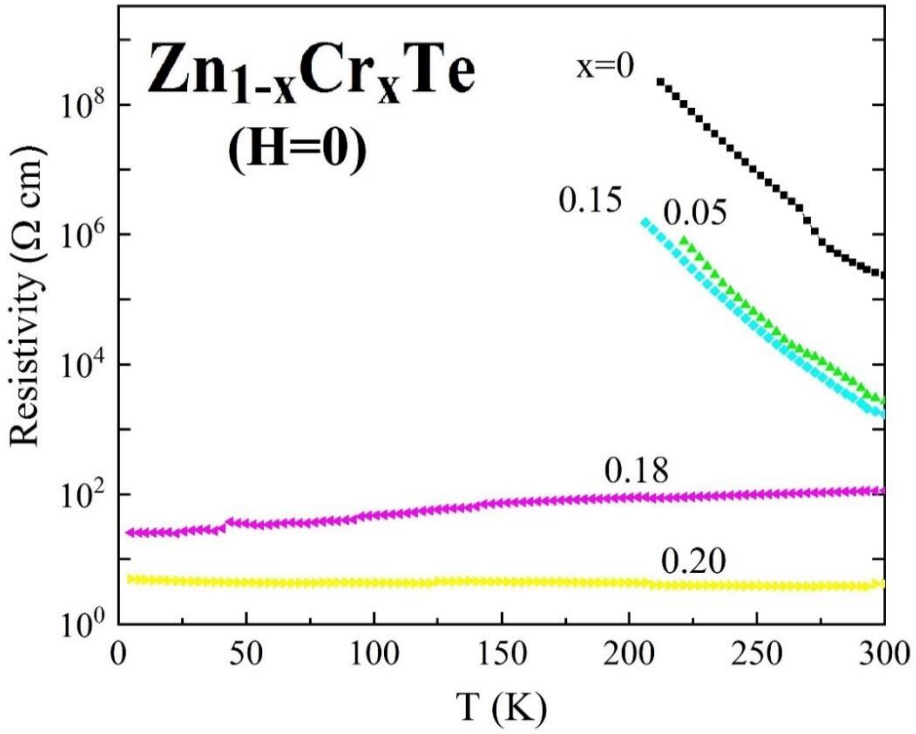

Figure 3. Temperature-dependent resistivity at zero applied magnetic field H, for polycrystalline $Zn_{1-x}Cr_xTe$ with x = 0.00, 0.05, 0.15, 0.18, and 0.20.

Increased Cr-concentration x leads to decreased resistivity in $Zn_{1-x}Cr_xTe$. The temperature dependent resistivities for the polycrystalline $Zn_{1-x}Cr_xTe$ samples with x = 0.18 and 0.20 shows enhanced conductivity. At room temperature, the resistivities of $Zn_{0.82}Cr_{0.18}Te$ and $Zn_{0.80}Cr_{0.20}Te$ are smaller than the resistivity of ZnTe by 3 or 4 orders of magnitude. As a result, $Zn_{1-x}Cr_xTe$ with x = 0.18 and 0.20 are exhibiting lower resistivities at room temperature.

Furthermore, it can be observed that the resistivity of the polycrystalline $Zn_{0.80}Cr_{0.20}Te$ is practically independent of temperature at below room temperature, which

can probably be a possible candidate as a half-metallic ferromagnet [44] i.e., it acts as a conductor to electrons of one spin orientation, but as an insulator or semiconductor to those of the opposite orientation. However, the study of half-metallicity in these polycrystalline samples is beyond the scope of this study. Further investigation about half metallicity in this polycrystalline sample is suggested. Figure 4 shows the temperature dependence of magnetization for the polycrystalline samples of $Zn_{1-x}Cr_xTe$ with x = 0.00, 0.05, 0.10, 0.15, 0.18, and 0.20. The magnetization as a function of temperature was recorded while warming the samples in the presence of the applied magnetic field of 5 kOe. Figure 4(a) shows the temperature dependence of ZFC magnetization of $Zn_{0.95}Cr_{0.05}Te$ at H = 5 kOe. The plot shows ferromagnetic transition at T_C ~ 230 K. By increasing Cr concentration, its T_C can be increased, which is shown in the inset of Figure 4(a). For the cases of $x \geq 0.10$, T_C is close to 300 K or above as the Cr content increases. These Curie temperatures are incredibly of interest since they are high enough for the purpose of device applications at room temperature. There is a second transition occurred at T ~ 100 K, which is indicated by arrows in the inset of Figure 4(a). These curves reveal that $Zn_{1-x}Cr_xTe$ structures have non- zero magnetizations well above room temperature. The magnetization vs. magnetic field were measured for $Zn_{0.80}Cr_{0.20}Te$ at 5 K and 300 K. The magnetization shown in Figure 4(b) was obtained after the subtraction of diamagnetic signal of ZnTe from the measured result. A hysteretic behavior has been observed with coercive fields of ~ 180 and ~ 220 Oe at T = 300 and 5 K, respectively. This indicates that ferromagnetism is introduced into the system by Cr concentration in ZnTe structure.

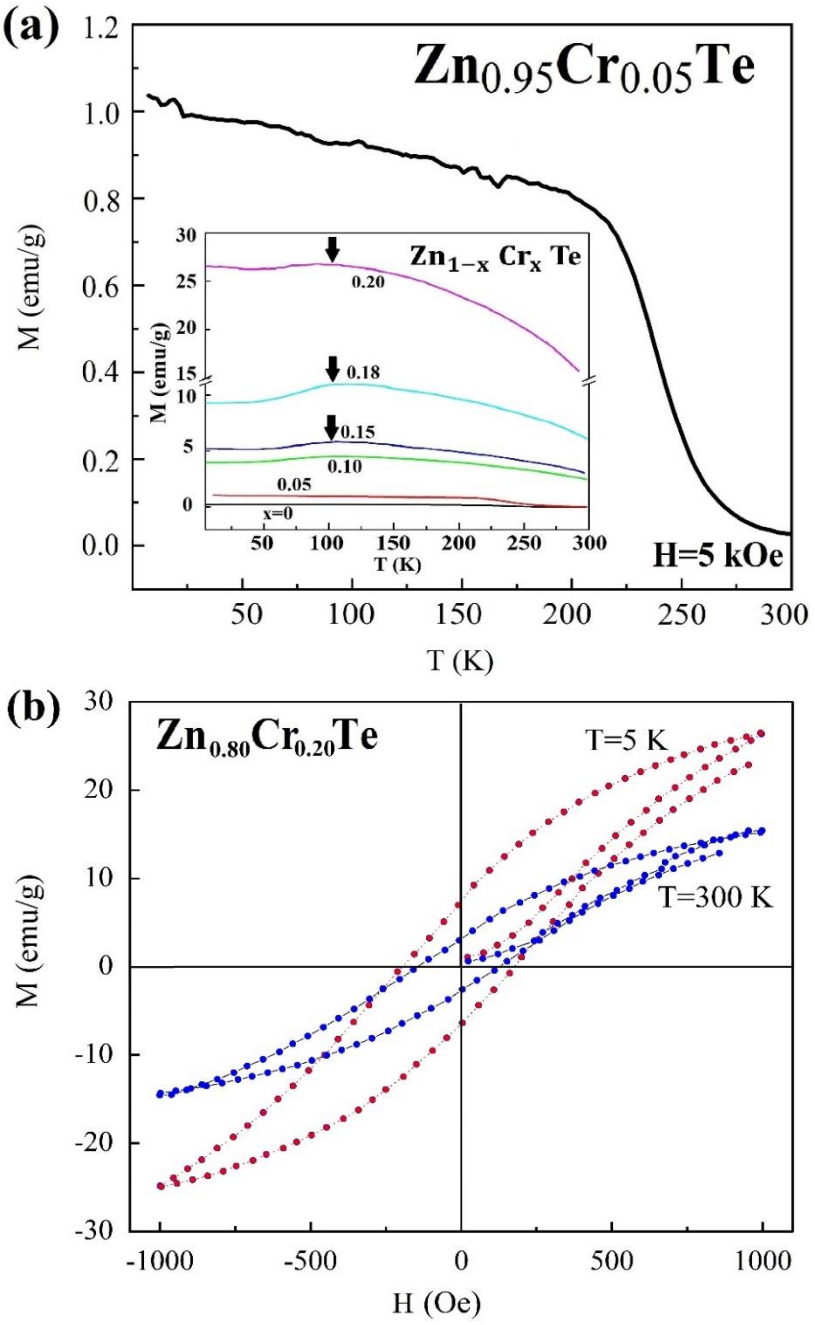

Figure 4. Magnetization of polycrystalline $Zn_{1-x}Cr_xTe$ for x = 0.00, 0.05, 0.10, 0.15, 0.18, and 0.20. (a) Temperature dependence of zero-field-cooled (ZFC) magnetization for polycrystalline $Zn_{0.95}Cr_{0.05}Te$ at H = 5 kOe. The inset shows the magnetization for polycrystalline $Zn_{1-x}Cr_xTe$. (b) Magnetic hysteresis loop for polycrystalline $Zn_{0.80}Cr_{0.20}Te$ at T = 5 K (red circles) and 300 K (blue circles) after subtracting the diamagnetic effect of ZnTe.

The origin of the ferromagnetic behavior in $Zn_{1-x}Cr_xTe$ could be due to the short-range interaction between the 3d-orbital electrons of Cr atoms hybridized with valence p electrons of the host anions, which can be an appropriate picture of a ferromagnetic DMS [31]. Figure 5 (a) shows the Tauc plots [45] extracted from the UV–vis absorbance measurements. It can be observed that the absorption bandgap in the bulk is due only to a direct gap. According to Tauc's explanation, the relation between E_g and absorption coefficient, α, of a direct-bandgap semiconductor could be expressed as $\alpha h\nu = \beta (h\nu - E_g)^n$, where β is a constant and $h\nu$ is the incident photon energy and the exponent n is a parameter dependent on the type of the electronic transition responsible for the absorption. The absorption bandgap in each $Zn_{1-x}Cr_xTe$ bulk is due only to a direct gap. For the ideal direct-bandgap semiconductor ZnTe, the value of n is 1/2. The E_g values were estimated by extrapolating the targets in Tauc plots to intercept with the hν-axis to give the values of the indirect optical energy gap (E_g). Figure 5(b) shows the direct bandgap, E_g, vs. Cr concentration. The results show that the energy bandgap decreases from 2.33 eV for ZnTe to 1.93 eV by 20% of Cr concentration. The concentration has induced a red shift of the bandgap which is in good agreement with the previous reported data of ZnTe [46,47].

Optical transmittance of $Zn_{1-x}Cr_xTe$ were measured for evaluating their optical transparency. The transmittance was measured in the mid-infrared to ultraviolet range (200–800 nm). As shown in Figure 6, UV–vis–IR spectra reveal that the optical transmittance of the $Zn_{1-x}Cr_xTe$ polycrystal depends on the Cr concentration. The undoped sample exhibits extraordinary transmittance in the UV–vis–IR regime (250–800 nm) without any sharp absorption features.

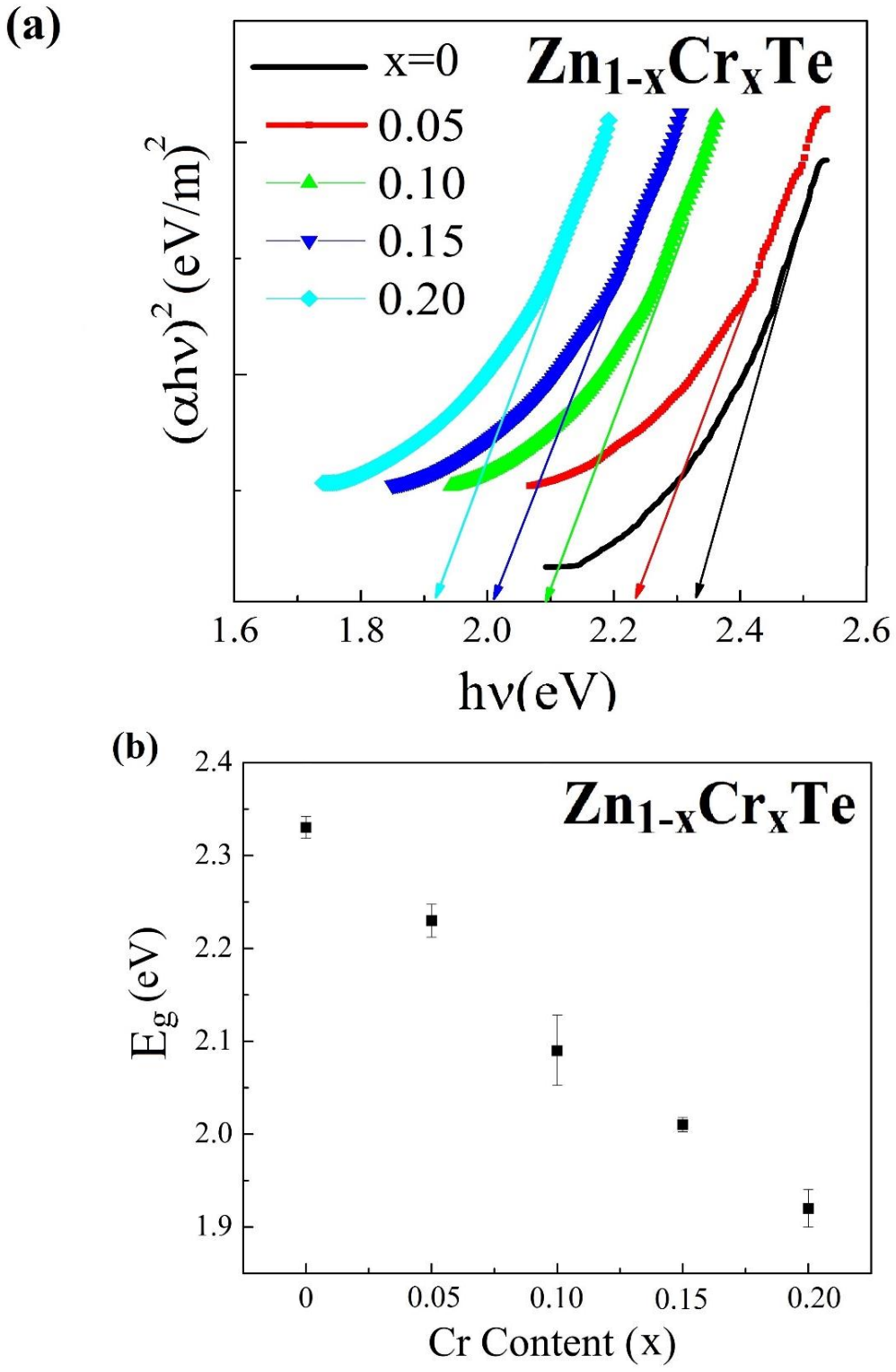

Figure 5. (a) First direct Tauc plot of polycrystalline $Zn_{1-x}Cr_xTe$ with x = 0.00, 0.05, 0.10, 0.15, and 0.20. (b) Direct band gap vs. Cr content.

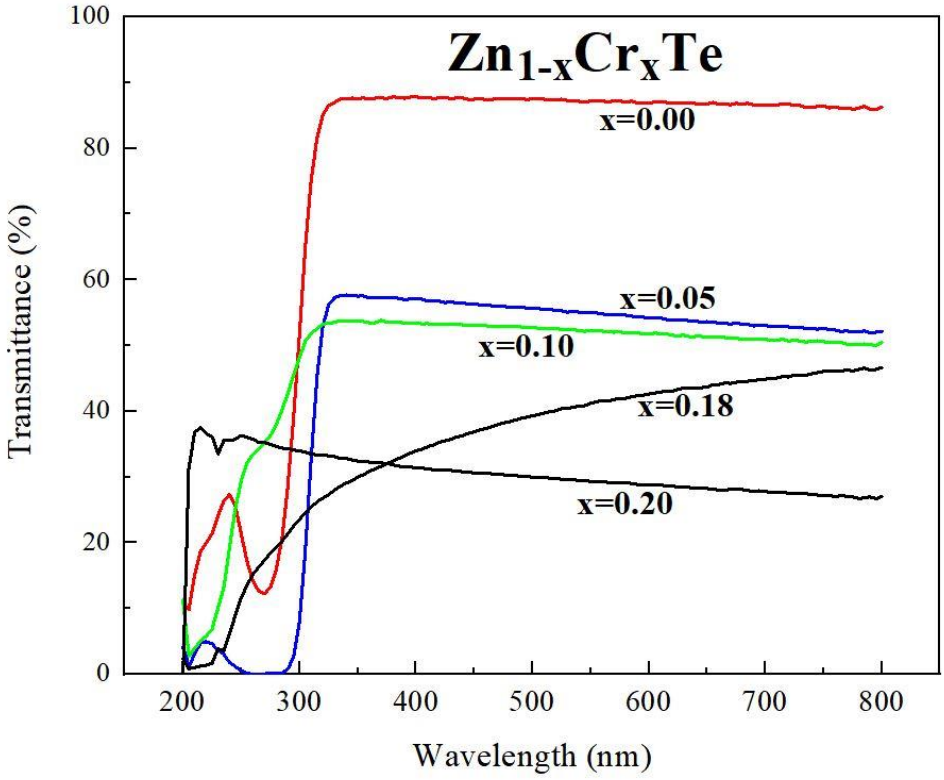

Figure 6. Optical transmittance of polycrystalline structures of $Zn_{1-x}Cr_xTe$ with x = 0.00, 0.05, 0.10, 0.18, and 0.20 at room temperature.

This sample has an average visible transmittance between 85 % and 90 %. Figure 6 shows that the transparency increases from around 0–20 % at 200–300 nm to a high uniform plateau at 300–800 nm. The direct photoexcitation of carriers within the surface state of this bulk may give rise to high optical transmission in the short-wavelength infrared region. These unique optical properties show that the $Zn_{1-x}Cr_xTe$ structure is a transparent ferromagnetic conductor.

Transparency is mainly defined by free electrons, position of Fermi energy and type of band structure in a solid. If the energy of the visible spectrum incident photon is equal

or greater than the band gap energy, then the photon can excite an electron from the valence band to the conduction band. Otherwise, the photon cannot interact with the valence band electrons. Thus, the photon goes through the material without any interaction. If the bandgap is higher than the maximum energy of the incident wave, then none of the light is absorbed and just passes through the material. Therefore, they appear transparent. Hence, wider band gap leads to higher transparency in the visible spectrum [54–59]. This is in agreement with the Tauc relation, which implies that the absorption coefficient α decreases with the enlargement of the optical band gap E_g, and also, the transmittance T lowers along with the growth of the absorption coefficient α [55,57]. Furthermore, for smaller band gaps, some colors will be absorbed. The transmitted light defines the visible color of the material. According to Figure 5(b), the band gap of ZnTe is ~ 2.3 eV, which means that in the visible range, this material absorbs blue and violet lights. Therefore, red, yellow, and partial green parts of the visible spectrum will pass through the material with no interaction, resulting in an orange-brown colored samples. In comparison, the pristine ZnTe is red-orange color. The sample $Zn_{0.80}Cr_{0.20}Te$ appears in dark gray color. This can be explained based on the band gap of this sample which is ~ 1.9 eV, (Figure 5(b)). Most of the colors are absorbed along with most of the light intensity (~ 75 % absorption). Therefore, the sample appears to look opaque and dark gray.

4. CONCLUSION

Polycrystalline samples of $Zn_{1-x}Cr_xTe$ for x = 0.00, 0.05, 0.10, 0.15, 0.18, and 0.20 have been obtained. Their magnetic and transport properties exhibit ferromagnetic

semiconducting behavior for $x \leq 0.15$ but ferromagnetic conductivity for x = 0.18 and 0.20. The transparency has been observed at a level of 30–85 % in the visible range for different Cr concentrations. With the synthesis of a transparent magnet, more advanced display devices will be innovated. As an example, speed and fuel meters and a map can be displayed directly on the front glass of a car or an airplane. The electrical transport of the polycrystalline $Zn_{0.8}Cr_{0.2}Te$ provides an inspiring idea that this material could be studied further for possible half-metallic ferromagnetism. However, the study of half-metallicity in these polycrystalline samples is beyond the scope of this study. Further investigation about half metallicity in this polycrystalline sample is suggested.

ACKNOWLEDGMENTS

The authors are thankful to Dr. N.D. Leigh for helpful support and discussion on UV–Vis. transmittance measurements. The work was supported in part by a grant from NSF DMR-1255607.

CREDIT AUTHORSHIP CONTRIBUTION STATEMENT

A. SARIKHANI: Conceptualization, Methodology, Visualization, Writing - original draft, Writing - review & editing. L. AVAZPOUR: Conceptualization, Methodology, Visualization, Writing - original draft, Writing - review & editing. W. LIYANAGE: Data curation, Formal analysis. R. FLOREZ: Data curation, Formal analysis. E. BOHANNAN: Data curation, Formal analysis. D. SATTERFIELD: Data curation,

Formal analysis. M. NATH: Data curation, Formal analysis. J. E. MEDVEDEVA: Conceptualization, Methodology, Visualization, Writing - original draft, Writing - review & editing. Y. S. HOR: Conceptualization, Methodology, Visualization, Writing - original draft, Writing - review & editing, Supervision.

REFERENCES

[1] C. Wang, J.C. Chien, K. Takei, T. Takahashi, J. Nah, A.M. Niknejad, A. Javey, Nano Lett. 12, 1527 (2012).

[2] B. Guo, Q. Yin, J. Zhou, W. Li, K. Zhang, and Y. Li, ACS Sustainable Chem. Eng. 7, 8206 (2019).

[3] S. Hung, T.T. Wang, L.W. Chu, L.J. Chen, J. Phys. Chem. C 115, 15592 (2011).

[4] C. Battaglia, J. Escarré, K. Söderström, M. Charrière, M. Despeisse, F.J. Haug, C. Ballif, Nature Photonics 5, 535 (2011).

[5] S. D. Sarma, Nature Materials 2, 292 (2003).

[6] E.Y. Tsymbal, Nature Materials 11, 12 (2012).

[7] D. Chiba, M. Sawicki, Y. Nishitani, Y. Nakatani, F. Matsukura, H. Ohno, Nature 455, 515 (2008).

[8] J. Philip, A. Punnoose, B. I. Kim, K. M. Reddy, S. Layne, J. O. Holmes, B. Satpati, P. R. LeClair, T. S. Santos & J. S. Moodera, Nature Materials 5, 298 (2006).

[9] K. L. Chopra, S. Major, D. K. Pandya, Thin Solid Films 102, 1 (1983).

[10] A. M. Nazmul, S. Sugahara, M. Tanaka, Phys. Rev. B 67, 241308 (2003).

[11] D. Roy, et al, J. Phys.: Conf. Ser. 1579 012007 (2020).

[12] R. A. Afre, N. Sharma, M. Sharon and M. Sharon, Rev. Adv. Mater. Sci. 53, 79-89 (2018).

[13] V. Sharma, R. Vyas, P. Bazylewski, G. S. Chang, K. Asokan and K. Sachdev, RSC Adv. 6, 29135 (2016).

[14] N. Sarmadian, R. Saniz, B. Partoens, D. Lamoen, K. Volety, G. Huyberechts and J. Paul, Phys. Chem. Chem. Phys. 16, 17724 (2014)

[15] P. Sakthivel, S. Asaithambi, M. Karuppaiah, R. Yuvakkumar, Y. Hayakawa, G. Ravi, Journal of Alloys and Compounds 820, 153188 (2020).

[16] B. Ouni, M. H. Lakhdar, R. Boughalmi, T. Larbi, A. Boukhachem, A. Madani, K. Boubaker, M. Amlouk, Journal of Non-Crystalline Solids 367, 1 (2013).

[17] A. Rayerfrancis, P. B. Bhargav, N. Ahmed, S. Bhattacharya, B. Chandra and S. Dhara, Silicon 9, 31 (2017).

[18] C. Guillen, J. Herrero, Thin Solid Films 520, 1 (2011).

[19] G. K. Dalapati, et al, J. Mater. Chem. A 9, 16621 (2021).

[20] J. Singh, R. Kumar, V. Verma, R. Kumar, Materials Science in Semiconductor Processing 123, 105483 (2021).

[21] R. K. M. Raghupathy, T. D. Kuhne, C. Felser and H. Mirhosseini, J. Mater. Chem. C 6, 541 (2018).

[22] D. Soundararajan, D. Mangalaraj, D. Nataraj, L. Dorosinskii, K.H. Kim, Mat. Let. 87, 113 (2012).

[23] K. Kanazawa, S. Yoshida, H. Shigekawa, S. Kuroda, Sci. Technol. Adv. Mater. 16, 015002 (2015).

[24] K. Sato, H. K. Yoshida, Semicond. Sci. Technol. 17, 367 (2002).

[25] K. Onodera, T. Masumoto, M. Kimura, Electronics Lett. 30, 1954 (1994).

[26] K. Sato, H. K. Yoshida, Jpn. J. Appl. Phys. 40, 651 (2001).

[27] W. Mac, A. Twardowski, M. Demianiuk, Phys. Rev. B 54, 5528 (1996).

[28] J. Blinowski, P. Kacman, J. A. Majewski, Crystal Growth 159, 972 (1996).

[29] L. Zhao, B. Zhang, Q. Pang, X. Zhang, W. Ge, J. Wanga, Appl. Phys. Lett. 89, 092111 (2006).

[30] Q. Wang, Q. Sun, P. Jena, Y. Kawazoe, Applied Physics 97, 043904 (2005).

[31] K. Kanazawa, T. Nishimura, S. Yoshida, H. Shigekawa, S. Kuroda, Nanoscale 6, 14667 (2014).

[32] N. Ozaki, I. Okabayashi, T. Kumekawa, N. Nishizawa, S. Marcet, S. Kuroda, K. Takita, Applied Physics Letters 87, 192116 (2005).

[33] H. Saito, V. Zayets, S. Yamagata, K. Ando, Journal of Applied Physics 93, 6796 (2003).

[34] S. Amari, S. Méçabih, B. Abbar, B. Bouhafs, Comput. Mater. Sci. 50, 2785 (2011).

[35] S. Kuroda, N. Nishizawa, K. Takita, M. Mitome, Y. Bando, K. Osuch & T. Dietl, Nature Mater. 6, 440 (2007).

[36] D. Soundararajan, D. Mangalaraj, D. Nataraj, L. Dorosinskii, J. S. Salazar, H. C. Jeon, T. W. Kang, Appl. Surf. Sci. 255, 7517 (2009).

[37] N. Ozaki, N. Nishizawa, S. Marcet, S. Kuroda, O. Eryu, K. Takita, Phys. Rev. Lett. 97, 037201 (2006).

[38] Y. Yamazaki et al, J. Phys.: Condens. Matter 23, 176002 (2011).

[39] M. Kobayashi et al, New J. Phys. 10, 055011 (2008).

[40] W. G. Wang, K. J. Han, K. J. Yee, C. Ni, Q. Wen, H. W. Zhang, Y. Zhang, L. Shah, J. Q. Xiao, Appl. Phys. Lett. 92, 102507 (2008).

[41] N. Ozaki, N. Nishizawa, S. Kuroda, K. Takita, J. Phys.: Condens. Matter 16, 5773 (2004).

[42] V. Y. Ivanov, G. Karczewski, M. Sawicki, M. Godlewski, A. R. Omel'chuk, N. Zhavoronkov, A. A. Davydov, Phys. Stat. Sol. (c) 1, 961 (2004).

[43] T. Fukumuraa, Y. Yamadaa, H. Toyosakia, T. Hasegawab, H. Koinumac, M. Kawasaki. Applied Surface Science 223, 62 (2004).

[44] R. A. de Groot, F. M. Mueller, P. G. van Engen, and K. H. J. Buschow, Phys. Rev. Lett. 50, 2024 (1983).

[45] J. Tauc, R. Grigorovici, A. Vancu, Phys. Stat. Sol. 15, 627 (1966).

[46] Y. Feng, X. Feng, Y. Ou, J. Wang, C. Liu, L. Zhang, et al., Physical review letters 115, 126801 (2015).

[47] D.A. Schwartz, D.R. Gamelin, Advanced Materials 16, 2115 (2004).

[48] N. Kobayashi, H. Masumoto, S. Takahashi, S. Maekawa, Scientific Reports 6, 34227 (2016).

[49] R. Woods-Robinson, Y. Han, H. Zhang, T. Ablekim, I. Khan, K. A. Persson, and A. Zakutayev, Chemical Reviews 120, 4007 (2020).

[50] V. Uvarov, J. Appl. Cryst. 52, 252 (2019).

[51] S. Som, and S. K. Sharma J. Phys. D: Appl. Phys. 45, 415102 (2012)

[52] I. C. Nogueira, L. S. Cavalcante, P. F. S. Pereira, M. M. de Jesus, J. M. Rivas Mercury, N. C. Batista, M. Siu Lid, and E. Longo, J. of Applied Crystallography 46, 1434 (2013).

[53] R. D. Shannon, Acta Cryst. A32, 751 (1976).

[54] A. Bouich, B. Hartiti, S. Ullah, M. Ebn Touhami, B. Mari, D.M.F.Santos, Materials Today: Proceedings 13, 663 (2019).

[55] M. Nolan, and S. D. Elliott, Chem. Mater. 20, 5522 (2008).

[56] A. S. Hassanien, A. A. Akl, Superlattices and Microstructures 89, 153 (2016).

[57] S. S. Chiad, International Letters of Chemistry, Physics and Astronomy 45, 50 (2015).

[58] A. A. Akl, S. A. Mahmoud, Optik 172, 783 (2018).

[59] X. Chen, K. Ruan, G. Wu, and D. Baoa, Appl. Phys. Lett. 93, 112112 (2008).

II. CHEMICALLY INDUCED FERROMAGNETISM NEAR ROOM TEMPERATURE IN SINGLE CRYSTAL $(Zn_{1-x}Cr_x)Te$ HALF-METAL

Jiasen Guo [1], Ali Sarikhani [2,†], Pousali Ghosh [1], Thomas Heitmann [3], Yew S. Hor [2], and Deepak Singh [1,*]

[1] University of Missouri, Department of Physics and Astronomy, Columbia, MO, USA

[2] Missouri University of Science and Technology, Department of Physics, Rolla, MO, USA

[3] University of Missouri Research Reactor, Columbia, MO, USA

* Corresponding author

† Equally contributed as the 1st author

Keywords: Cr-doped ZnTe single crystals, Half metal, Room temperature ferromagnetism, ZnCrTe single crystals, Neutron scattering, Spintronics.

ABSTRACT

Magnetic semiconductors are at the core of recent spintronics research endeavors. Chemically doped II-VI diluted magnetic semiconductors, such as $(Zn_{1-x}Cr_x)Te$, provide promising platform in this quest. However, a detailed knowledge of the microscopic nature of magnetic ground state is necessary for any practical application. Here, we report on the synergistic study of $(Zn_{1-x}Cr_x)Te$ single crystals using elastic neutron scattering measurements and density functional calculations. For the first time, our research unveils the intrinsic properties of ferromagnetic state in macroscopic specimen of $(Zn_{0.8}Cr_{0.2})Te$. The ferromagnetism is onset at Tc ~ 290 K and remains somewhat independent to modest change in the substitution coefficient x. We show that magnetic moments on Zn/Cr site

develop ferromagnetic correlation in a-c plane with large, ordered moment of $\mu = 3.08\ \mu_B$. Magnetic moment across the lattice is induced via the mediation of Te site, uncoupled to the number of dopant carriers as inferred from the density functional calculation. Additionally, the ab-initio calculations also reveal half-metallicity in x = 0.2 composition. These properties are highly desirable for future spintronic applications.

Diluted magnetic semiconductors (DMS) are attractive for spintronic applications, as the underlying ferromagnetic and electrical properties can be easily tuned by modest chemical doping [1-3]. Previous efforts in this regard have mainly focused on the exploration of III-V DMS compounds, such as Mn-doped GaAs and InAs [4-8]. In these materials, the ferromagnetic transition temperature, Curie temperature, is sufficiently far below room temperature, which is one of the key requisites for the spintronic application. So far, the highest detected Curie temperature in these compounds is $T_c \sim 170$ K in Mn-doped GaAs/Be-doped p-type AlGaAs heterostructures.[4] Also, both magnetic and electrical phenomena are interlinked and directly attributed to the carrier (hole) doping of Mn ions-holes ferromagnetically mediate between d-orbital local moments [2,8,9]. Therefore, higher doping of Mn ions, needed to enhance the ferromagnetic Curie temperature in III-V DMS, would inevitably change the semiconducting property into metallic characteristic.

In contrast to the III-V DMS, exploration of II-VI diluted magnetic semiconductors e.g. $(Zn_{1-x}Cr_x)T$ where T = Se, S, Te have revealed the persistence of near room temperature ferromagnetism.[10-12] Additionally, theoretical and experimental study of II-VI DMS have demonstrated the uncoupled nature of magnetic and electrical phenomena.[10, 13-15] In this case, magnetism is derived from the exchange interaction between the delocalized

s, p band electrons and localized d-electrons of magnetic ions, not directly from the magnetic impurity e.g. Cr [13]. A positive value of exchange interaction would indicate ferromagnetic state of the system [1]. Experimental investigation of s, p-d exchange interaction using magnetic circular dichroism measurements have revealed positive exchange constant in $(Zn_{1-x}Cr_x)Te$ thin film [10].

Among the many compositions of $(Zn_{1-x}Cr_x)T$, where T = Se, S, Te, tellurides are of special importance. ZnTe is a wide band gap nonmagnetic semiconductor with energy gap of $\Delta \sim 6$ eV [16]. It crystallizes in the zinc-blend cubic structure with lattice parameter of a = 6.103Å [13]. The compound manifests near room temperature ferromagnetism at modest Cr doping in thin film specimen of $(Zn_{1-x}Cr_x)Te$ ($x \sim 0.035$) despite a very low carrier density of 1.1015 cm^{-3} [17]. More recently, study of polycrystalline $(Zn_{1-x}Cr_x)Te$ has confirmed the occurrence of high temperature ferromagnetism [18]. It was also inferred that the DMS material at 20% Cr substitution exhibits half-metallic characteristic, which can be used to generate the fully spin-polarized current [18]. Interestingly, similar conclusions were drawn in the recent density functional calculations of analogous DMS material (ZnCr)Se [19]. Although, these properties are of strong technological importance, but the lack of fundamental understanding of the ground state magnetic configuration in $(Zn_{1-x}Cr_x)Te$ hinders practical application. We have synthesized high quality single crystal samples of various substitution coefficients that are used to elucidate the intrinsic magnetic properties. Details about the quality of single crystals can be found elsewhere [18].

In this article, we report on the synergistic investigation of two substitution coefficients, x = 0.2, 0.15, using the ab initio calculation and detailed elastic neutron scattering measurements of single crystal specimens. We find direct evidence of a long-

range ferromagnetic order with transition temperature of T_c = 290 K in the bulk material. The Curie temperature does not change for a modest variation in the Cr substitution percentage. Surprisingly, the power-law exponent of the order parameter, $\beta = 0.46(02)$, in $x = 0.2$ composition is larger than that typically found in ferromagnetic materials. Such a large β value suggests inclination to the critical behavior of correlated moments. Numerical modeling of the experimental data illustrates ferromagnetic alignment of moments in the a-c plane with an ordered moment of $\mu = 3.08\ \mu_B$. The estimated ferromagnetic moment is also consistent with the ab-initio density functional theory (DFT) calculations. Given the fact that most research works have focused on the magnetic study of epitaxial thin film of (ZnCr)Te where substrate effect and reduced dimensionality of the specimen can be playing important roles [20, 21], this is the first time we unequivocally elucidate the intrinsic magnetic nature of the chemically doped $(Zn_{1-x}Cr_x)Te$.

The density functional theory calculations are carried out using a plane-wave basis set as implemented in the QUANTUM-ESPRESSO software. [22] The simulated system, illustrated in Figure 1a, is constructed by replacing one Zn atom with Cr atom per unit cell, corresponding to 25% doping level. The Generalized Gradient Approximation (GGA) along with the revised Perdew-Burke-Ernzerhof exchange-correlation functional (PBEsol) are implemented with projector-augmented wave (PAW) pseudopotentials [23, 24]. A well-converged kinetic energy cutoff of 80 Ry for wave function and charge density of 640 Ry are used throughout the calculation. Geometry optimization is performed by relaxing the atomic positions via systematically changing the lattice parameter with energy and force convergence thresholds of 0.0001 and 0.001 a. u., respectively. Brillouin zone (BZ) integrations during the structure optimization are performed on a Monkhorst-Pack k-grid

of 8 × 8 × 4, while a uniform dense grid of 30 × 30 × 30 is used for the construction of the Fermi surface (FS) and the density of state (DOS) [25, 26]. The DFT+U+V approach is adopted to account for the localization effect in the Cr 3d manifold as well as the hybridization between Cr 3d manifold and Te 5p manifold. The on-site interaction U of Cr 3d manifold and the inter-site interaction V between Cr 3d manifold and Te 5p manifold are determined by using a q-grid of 5 × 5 × 5 within the density functional perturbation theory (DFPT), as implemented in the QUANTUM-ESPRESSO software [26].

The DFT calculation yields ferromagnetism in this system. The calculated moment on Cr and Te sites are ~ 4 μ_B and 0.1 μ_B, respectively. The ordered moment values are also consistent with other reports. Moments are antiparallel with each other on neighboring Cr and Te sites [27, 28]. The calculated spin-resolved density of states (DOS), presented in Figure 1c, show that the Fermi energy passes through the spin-up DOS while there is a gap of the spin-down DOS, confirming the half-metallic nature of this system [27, 28]. DFT calculation of ~ 19% doping level yields similar results, see Figure 1d. Three-hole pockets are observed in the spin-up Fermi surface, shown in Figure 1b, which is consistent with the p-type doping of Cr in the host ZnTe structure. Parallel surfaces are separated by (100) rlu along the crystallographic directions.

Experimental verification of the intrinsic magnetism in $(Zn_{0.8}Cr_{0.2})Te$ is obtained from elastic neutron scattering measurements. Neutron scattering measurements were performed on an 8 mg flux grown thin rectangular shape single crystal, of dimension 3 mm (length) × 2mm (width) × 1.25 mm (thickness), at the thermal Triple Axis Spectrometer, TRIAX, at the University of Missouri Research Reactor (MURR).

Elastic measurements were performed at the fixed final energy of 14.7 meV using PG (pyrolytic graphite) monochromator. The measurements on TRIAX employed a at pyrolytic graphite (PG) analyzer with collimator sequence of PG filter-60'-60'-Sample-40'-PG filter-40'. Single crystal sample was mounted at the end of the cold finger of a closed cycle refrigerator with a base temperature of T ~ 5 K. Measurements were performed with the crystal oriented in the (HHL) scattering plane. Here, H and L represent reciprocal lattice units of $2\pi/a$ and $2\pi/c$, respectively, with c = a.

Single crystal allows for a detailed examination of the intensities and magnetic scattering pattern, which reveals the nature of spin correlations that are not possible to obtain from magnetic and thermodynamic measurements. Elastic scans were obtained along both HH- and L-crystallographic directions, as shown schematically in Figure 2a. In Figure 2c-d, we show representative scans at various temperatures across [-1-13] nuclear Bragg peak along HH and L- directions. As the sample is cooled to low temperature, scattering intensity enhancement of nuclear Bragg peak becomes apparent. Neutron scattering data is well described by the resolution convoluted Gaussian line shape. Full width at half maximum at representative peaks are shown in the inset of Figure 2d.

We see that the width of the peak does not change as a function of temperature. Also, it is comparable to the resolution of the thermal triple axis spectrometer. The additional scattering, which is arising due to magnetic correlation in the sample, indicates the development of commensurate long range magnetic order in the system.

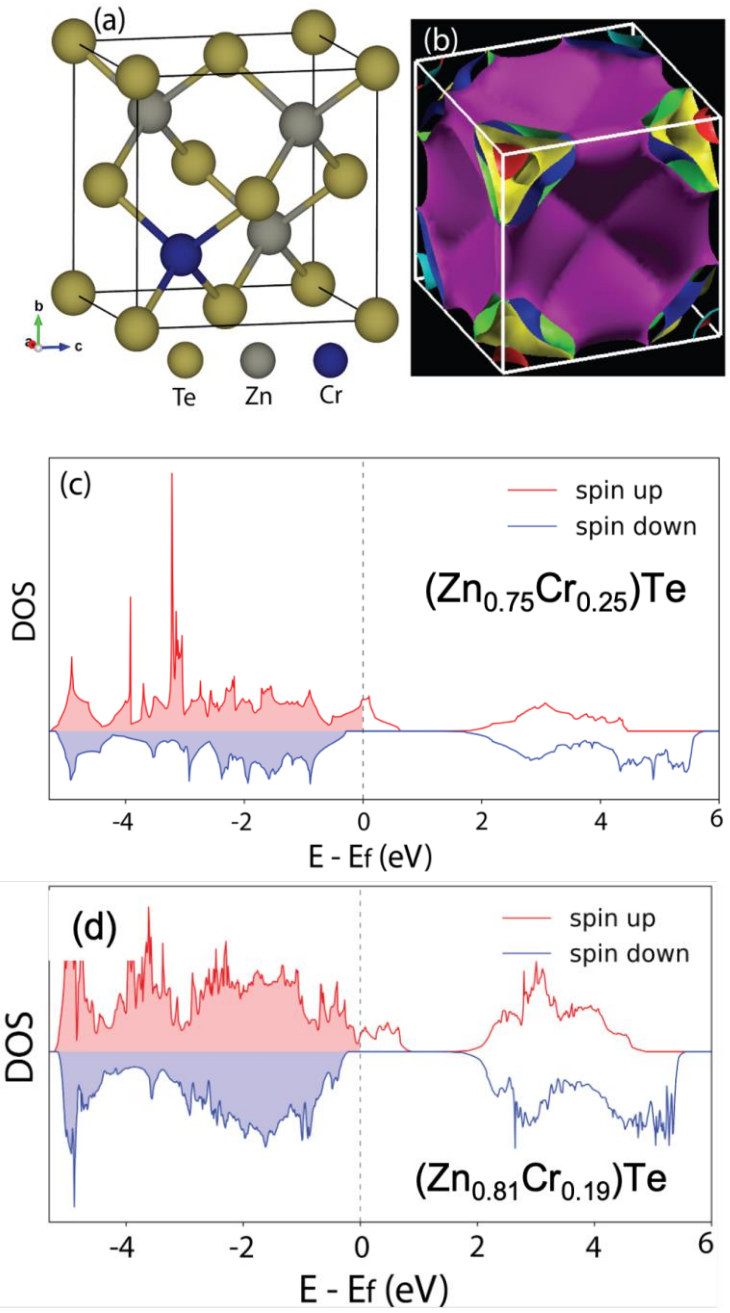

Figure 1. (color online) Density functional theory calculations. (a) Chemical structure of $(Zn_{0.75}Cr_{0.25})Te$, used for the DFT calculations. (b) Density functional theory calculated Fermi surface, viewed from the top and tilted-axes projection. Parallel surfaces in the hole pockets are separated by wave vector, $\overline{\alpha\gamma}$ = (100) rlu in the reduced units of $2\pi/a$ for the cubic structure, also consistent with experimental finding. (c) Spin polarized density of states in 25% Cr-substituted ZnTe, depicting half-metallic state. (d) Similar results are obtained in DFT calculations on $(Zn_{0.81}Cr_{0.19})Te$.

At low temperature, all nuclear peaks are found to manifest enhanced elastic intensity, limited by the form factor of Cr atom. The chemical substitution of Zn by Cr induces magnetism via the modification of the Fermi surface in $(Zn_{1-x}Cr_x)Te$, as evidenced by the DFT calculations. In fact, recent studies have revealed that the magnetism in (ZnCr)Te is onset at a doping percentage of as low as 5% of Cr atoms [17, 18]. Besides the detailed experimental investigation of 20% Cr substitution level, we have also performed neutron measurements on $(Zn_{0.85}Cr_{0.15})Te$ compound. Magnetic order parameter as a function of temperature for both 15% and 20% Cr substitutions are plotted in Figure 2b. The order parameter data are fitted with the power law equation: $I \propto \left(1 - \frac{T}{T_c}\right)^{2\beta}$, to accurately estimate the magnetic transition temperature and the critical exponents that can provide important information about the nature of the phase transition. Fitting of experimental data using the power law equation yields Curie temperature of Tc ~ 290 K in both compounds.

The value of exponent beta for the substitution coefficients of x = 0.2 and 0.15 are estimated to be 0.46(02) and 0.36(04), respectively, that suggest the three-dimensional interaction in the ordered regime. These beta values are very close to the critical phase transition exponent ~ 0.5. We also observe unusually linear-type trend in the order parameter plot of both compounds, albeit more pronounced in higher substitution coefficient of x = 0.2.

Typically, a ferromagnetic transition is accompanied by the first order phase transition. The magnetic phase transition in (ZnCr)Te clearly departs from the conventional trend. Perhaps, the nature of magnetic moment correlation can shed light on this.

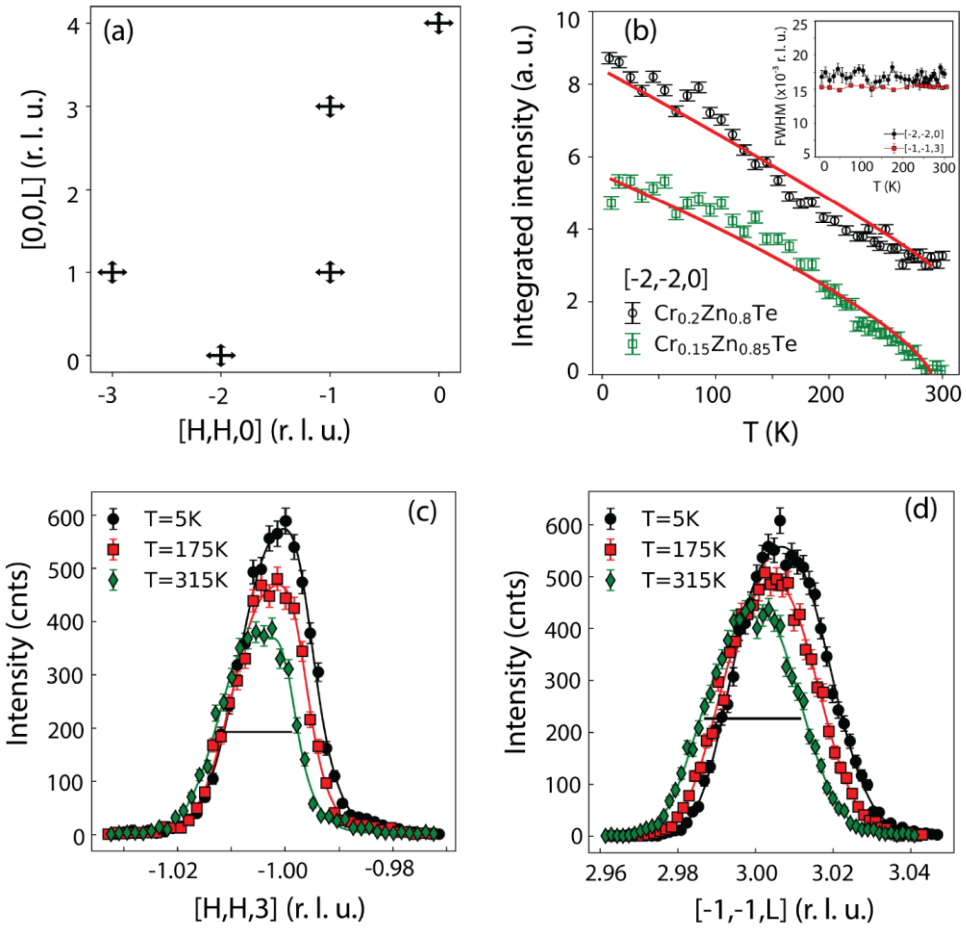

Figure 2. (color online) Neutron scattering measurement of $(Zn_{1-x}Cr_x)Te$, x = 0.2, 0.15. (a) Schematic of elastic scans across the nuclear Bragg peak positions in multiple Brillouin zones. Measurements are performed in both HH and L directions to accurately determine the integrated intensity. (b) Magnetic order parameters of $(Zn_{1-x}Cr_x)Te$, x = 0.2, 0.15 as a function of temperature. Magnetic order parameter is obtained by subtracting the high temperature data, at T = 325 K, to consecutive low temperature data. The intensity was estimated by fitting individual rocking scan at (-1-13) peak position at different temperatures. Fitting of order parameter by power law (see text for detail) yields Tc = 290 K in both x = 0.2 and 0.15 substitution coefficients with the power law exponent of 0.46(02) and 0.36(04), respectively. Inset shows the temperature dependence of FWHM. (c-d) Representative scans of neutron measurements on $(Zn_{0.8}Cr_{0.2})Te$ at different temperatures along HH- and L- directions across (-1-13) rlu. As temperature reduces, nuclear peak intensity increases; thus, suggesting the development of ferromagnetic ground state. Experimental data are well described by Gaussian line shape. In all plots, error bars represent one standard deviation.

To understand the nature of ground state spin correlation in $(Zn_{0.8}Cr_{0.2})Te$, detailed maps of nuclear and magnetic scattering peaks across several Brillouin zones were obtained at two temperatures of T = 325 K and T = 5 K on TRIAX spectrometer. We show the color plot of mesh scan data at T = 5 K in Figure 3a. Stronger magnetic scattering is observed along the [00L] direction, compared to the [HH0] positions. Since magnetic contribution to the total intensity at structural Bragg peaks are more pronounced at low temperature, we subtract the high temperature data to the low temperature data for numerical modeling purposes. The numerical modeling of experimental results is performed using the FullProf program in conjunction with the representational analysis by SARAh program [29]. In this case, the number of symmetry-allowed magnetic structures, possible for a particular crystallographic site, is simply the number of non-zero irreducible representations in the magnetic representation. The best fit to experimental data is found for a ferromagnetic configuration of magnetic moments on Zn/Cr sites that align along the diagonal direction in the a - c basal plane, defined by polar coordinates of $\theta = 120°$ and $\phi = -2°$, see Figure 4. The estimated size of ordered moment is $\mu \sim 3.08\ \mu_B$.

The ground state spin configuration was independently verified using the model calculations. The simulated scattering intensities are obtained by adding up both the nuclear scattering and the magnetic scattering contribution. For the simulation purposes, we have used multiple lattice units of the size 10 × 10 × 10. Also, a weighted average scattering length is used for the Zn/Cr sites. The magnetic structure factor is calculated using the formula of $F_M = \sum_j S_{\perp j}\, p_j\, e^{iQr_j} e^{-W_j}$, [30] where $S_\perp = \hat{Q} \times (S \times \hat{Q})$ is the spin component perpendicular to the Q, $p = \left(\frac{\gamma r_0}{2}\right) g\, f(Q)$, $\left(\frac{\gamma r_0}{2}\right) = 0.2695 \times 10^{-12}\ cm$, g

is the Lande splitting factor and was taken to be g = 2, f(Q) is the magnetic form factor and e^{-W_j} is the Debye-Waller factor and was taken to be 1. 20% of Zn sites are randomly substituted by Cr atoms in the lattice units for the calculation of the magnetic structure factor.

The simulated pattern is shown in Figure 3b. Numerically simulated scattering pattern for the spin configuration, shown in Figure 4, well describes experimental results for the ordered moment of $\mu \sim 3.08\ \mu_B$.

Such a large, ordered moment can be arising due to the clustering of Cr ions or the induced magnetism on Zn/Cr site, mediated by Te ions. The clustering of Cr ions would result in the finite size effect, often reflected by the short-range order in elastic measurements, as found in spin glass systems [31]. But this is not what we observe. Resolution limited elastic peaks suggest the presence of long-range magnetic order in the system. So, magnetism in Cr-doped compound is most likely associated to the induced magnetism mediated by the orbital overlap between Zn/Cr and Te sites. Subsequently, we expect other compositions with varying Cr percentages to manifest same or similar magnetic structure, albeit with smaller (larger) ordered moment size at small (large) Cr substitution. The argument of induced magnetism is also consistent with the DFT calculations from a string of reports, including ours as discussed above. Given the fact that 20% substitution of Zn by Cr would result in the random replacement of approximately one Zn atom by the Cr atom per unit cell, the size of ordered moment cannot be this large.

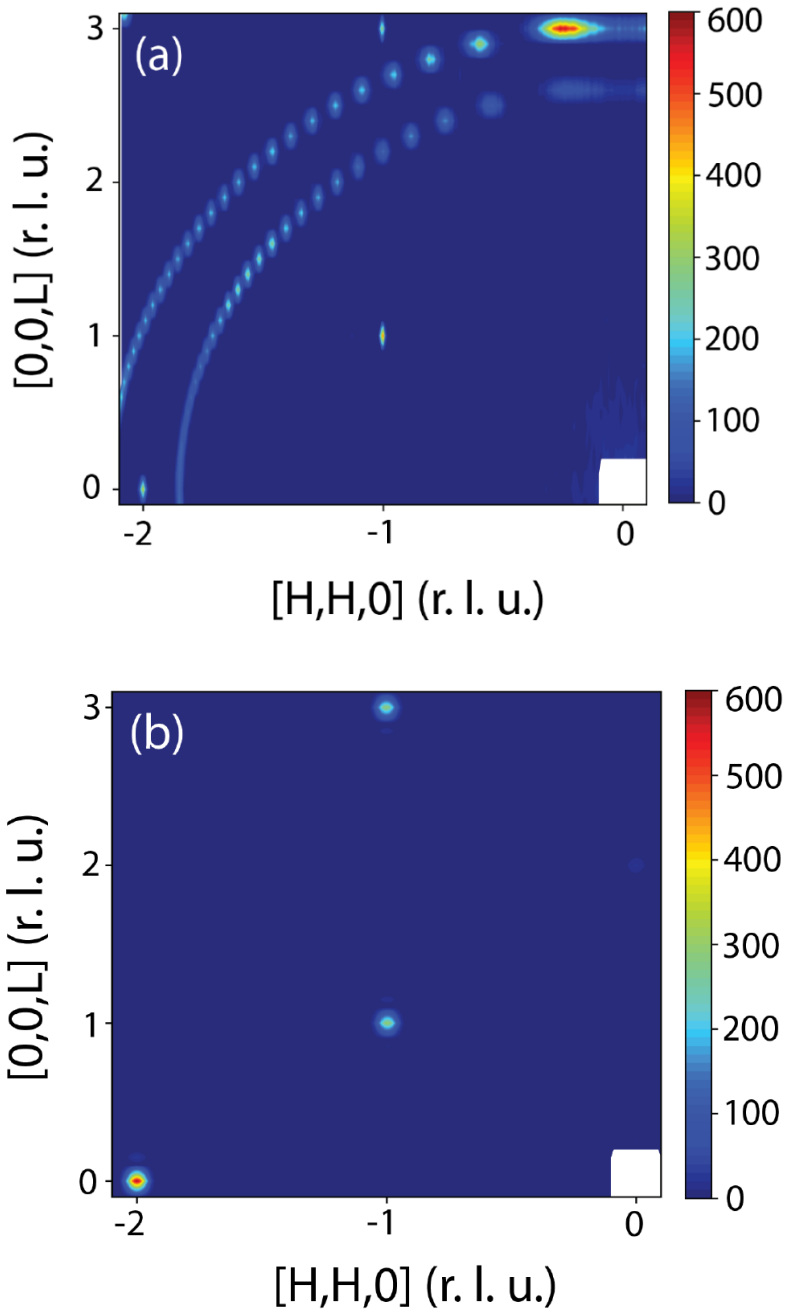

Figure 3. (color online) Numerical modeling of experimental data. (a) Detailed color map, depicting nuclear and magnetic scattering across several Brillouin zones, obtained on TRAIX spectrometer at T = 5 K. The circular streaks are arising due to aluminum powder lines from the sample holder. (b) Numerical modeling of experimental data was independently performed using model calculations. Calculated scattering pattern for moment configuration shown in Figure 4 describes experimental data.

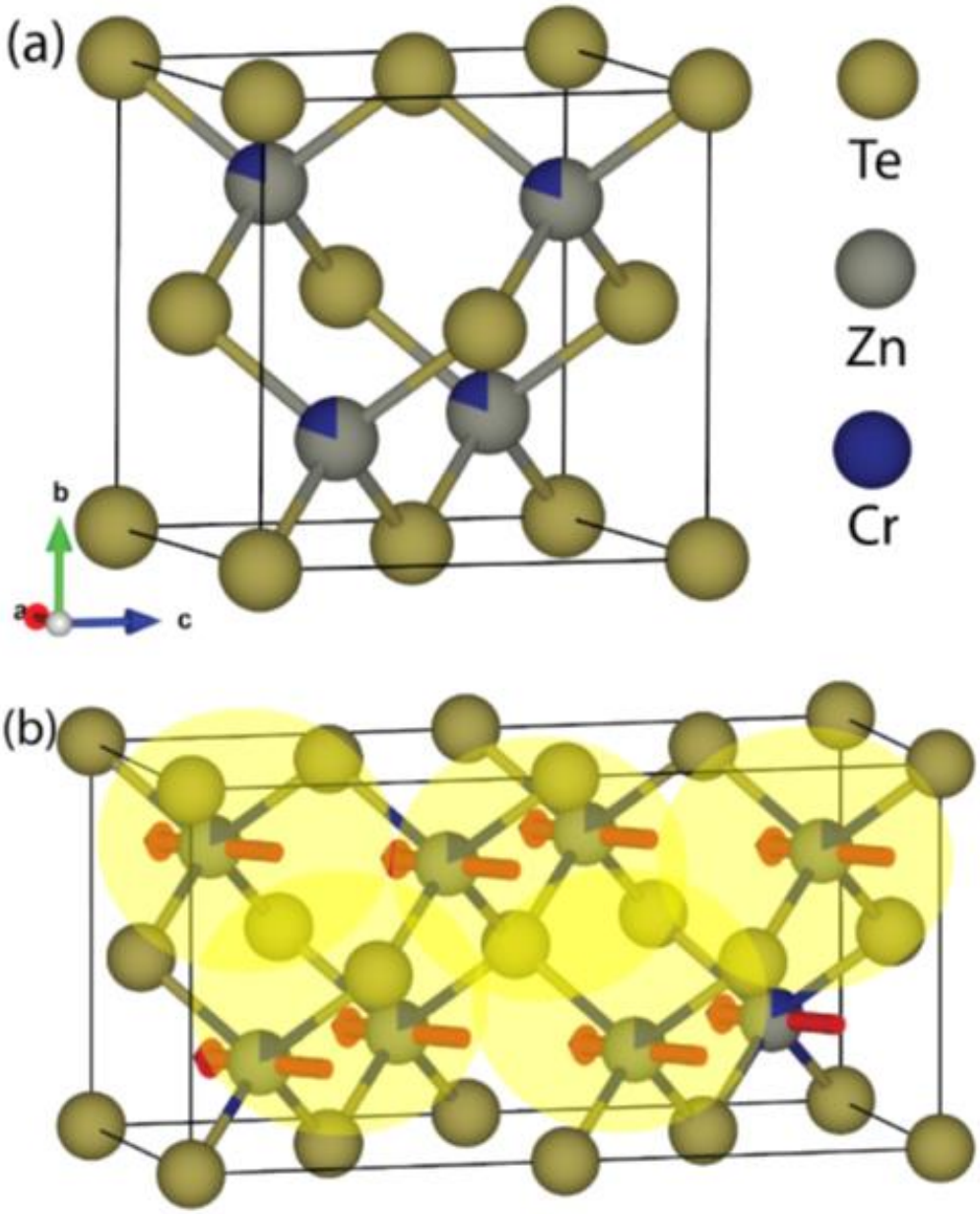

Figure 4. (color online) Ground state spin correlation and induced magnetism. Refinement using FullProf-SARAh representational analysis suggests ferromagnetic arrangement of magnetic moments on Zn/Cr site with polar angles of $\theta = 120°$ and $\phi = -2°$. The large, estimated moment, arguably, arises due to the induced magnetism mediated by orbital overlap on Te-sites, depicted by transparent circles.

Cr ion in ZnTe has 3d4 electronic configuration. Therefore, even in the case of entire unit cell being occupied by Cr ion (instead of Zn/Cr ion), the maximum ordered moment may not be larger than 4 μ_B. Hence, $(Zn_{0.8}Cr_{0.2})Te$ is expected to exhibit a much smaller ordered moment than this optimum value as less than one site per unit cell, on the average, is occupied by the Cr atom. The only explanation to this conundrum lies in the phenomena of induced magnetism. A similar behavior arises in (GaMn)As where Mn substitution induces large magnetic moment across the entire unit cell, even though the parent compound GaAs is non-magnetic [2].

In summary, we have performed detailed synergistic investigation of underlying magnetism in single crystal specimen of Cr-doped ZnTe using DFT calculation and neutron scattering measurements. Previous study of (ZnCr)Te have mainly focused on the epitaxially grown thin film samples of reduced dimensionality where the substrate can have pronounced effect on physical and magnetic properties. The study of bulk crystalline material unveils the intrinsic property of the system. Our research works reveal the ferromagnetic nature of moment correlation along the diagonal direction in a-c plane. The long-range ferromagnetic order is onset at high temperature of $T_c = 290$ K. Also, the Curie temperature does not seem to vary for a modest change in the Cr substitution percentage. Importantly, the ordered moment on Zn/Cr site is quite large, $\mu = 3.08\ \mu_B$, despite the small substitution coefficient in $(Zn_{0.8}Cr_{0.2})Te$. We argue that such large, ordered moment arises due to the induced magnetism between Zn/Cr-Te orbital overlaps and not depends on the number of dopant carriers. The qualitative explanation as well as the size of ordered moment are in good agreement with the DFT calculations. Further research works, elucidating the quantitative aspect of exchange interaction in (ZnCr)Te using inelastic

neutron scattering measurements, are highly desirable. It will require large single crystal samples that are currently not available. DFT calculations also suggest half-metallicity in $(Zn_{0.8}Cr_{0.2})Te$. The theoretical finding, although consistent with recent experimental report, [18] needs further investigation via electrical transport measurements. The chemically induced ferromagnetic property in (ZnCr)Te semiconductor can have practical implication to the spintronics research. Finding a suitable semiconducting material with chemically tunable ferromagnetism, which persists to room temperature or higher, is an important research problem. (ZnCr)Te can provide a strong platform in this endeavor.

ACKNOWLEDGMENTS

DKS thankfully acknowledges the support by the Department of Energy, Office of Science, Office of Basic Energy Sciences under the grant no. DE-SC0014461.

DATA AVAILABILITY STATEMENT

The data that support the fundings of this study are available from the corresponding author upon request.

† Author contributed equally

SUPPLEMENTARY MATERIAL

DFT calculation for a lower doping level $Zn_{1-x}Cr_xTe$ is carried out with the structure illustrated in Figure S1a. Consider the computational resources available, three Zn atoms are replaced with Cr atoms in a supercell of 2 × 2 × 1, corresponding to x ∼ 0.19. The kinetic energy cutoff as well as the charge density cutoff are set to 80 Ry and 640 Ry. The same on-site U parameter for Cr 3d manifold and inter-site V parameter between Cr 3d manifold and Te 5p manifold as determined for $Zn_{0.75}Cr_{0.25}Te$ are used in the calculations. Geometry optimization is carried out following the same procedure as for $Zn_{0.75}Cr_{0.25}Te$ with a Monkhorst-Pack k-grid of 7 × 7 × 4. Similar to those found in $Zn_{0.75}Cr_{0.25}Te$, moments of ∼ 4 μB and 0.08-0.085 μB are found on the Cr sites and neighboring Te sites of the optimized geometry, antiparallel to each other, confirming the ferromagnetism of $Zn_{0.81}Cr_{0.19}Te$. The spin resolved density of state (DOS), as is shown in Figure S1b is also calculated for the optimized geometry with the same k-grid. The Fermi level passes through the spin-up DOS while finds a gap in the spin-down DOS, confirming the hall-metallic nature of $Zn_{0.81}Cr_{0.19}Te$. Together with the DFT results calculated for $Zn_{0.75}Cr_{0.25}Te$ in Figure 1, clearly, ferromagnetism and half-metallic nature can be expected for $Zn_{1-x}Cr_xTe$ with x in between 0.19 and 0.25.

The magnetic structure refinement is carried out using the FullProf Suite in conjunction with SARAh representational analysis. The magnetic contribution of the observed peak integrated intensities is obtained as the following:

$$I_{mag} = \frac{I_{5K} - I_{325K}}{DW_{325K}}, \quad (2)$$

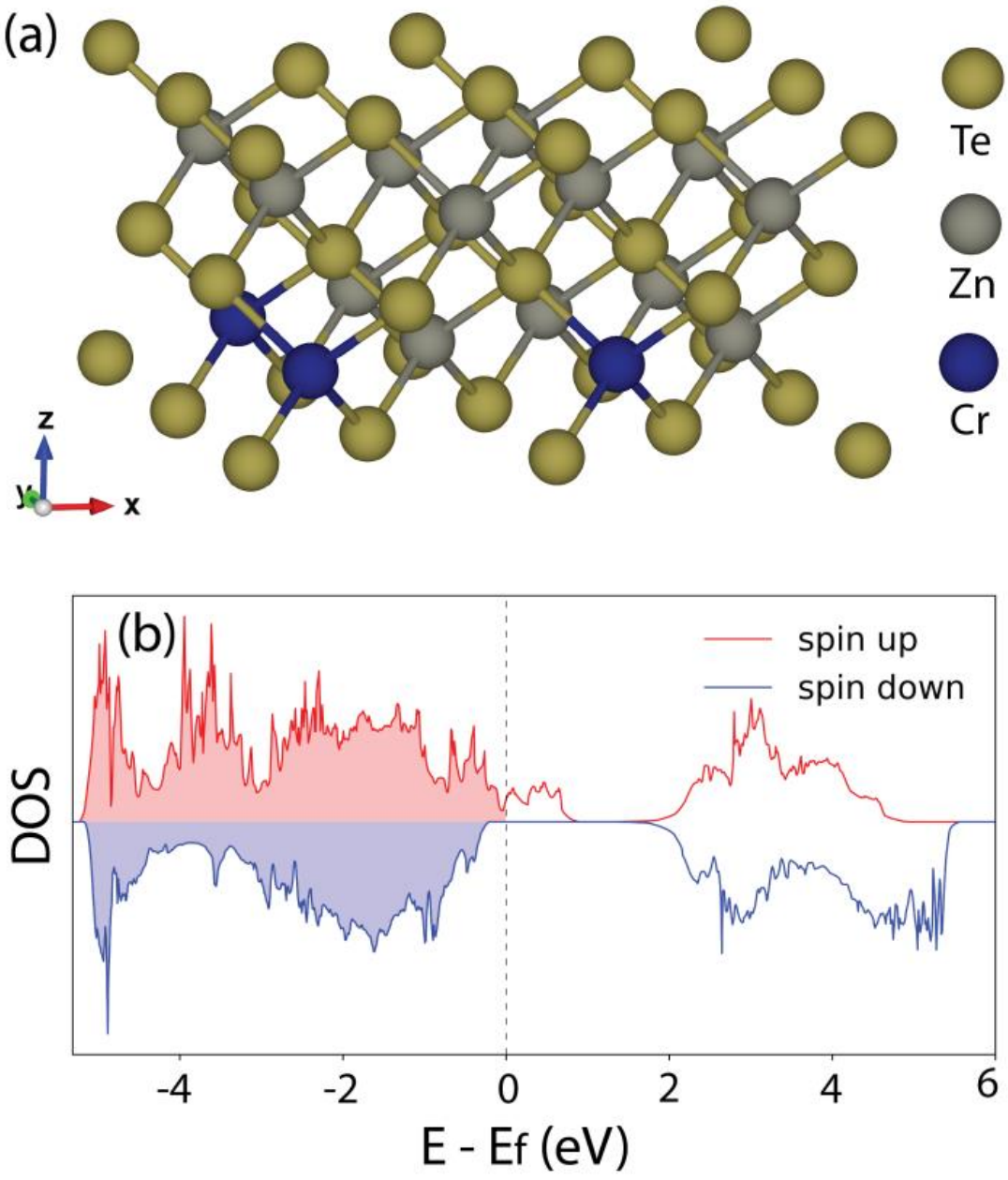

Figure S1. (a) Illustration of $Zn_{0.81}Cr_{0.19}Te$ used in the DFT calculation. (b) The corresponding calculated spin-resolved DOS shows the Fermi level passes through the spin-up DOS while finds a gap in the spin-down DOS, indicating $Zn_{0.81}Cr_{0.19}Te$ is half metallic.

where the Debye-Waller factor DW_{325K} is given by

$$DW_{325K} = \exp\left(\frac{-B_{iso}}{8\pi^2} Q^2\right). \quad (3)$$

The isotropic thermal parameter $B_{iso} \approx 0.8$ is estimated from structure refinement with single crystal XRD data collected at room temperature. Here we have assumed that at 5K, the thermal effect on the scattering intensity becomes negligible. Integrated intensities of the five scanned peaks indicated in Figure 2a are used as fitting observables for the magnetic structure determination. Magnetic phase input for FullProf refinement is prepared through SARAh representational analysis. The structural parameters are kept fixed during the refinement, with the occupation ratio of Cr set to 0.2, and that of Zn set to 0.8 on the Zn sites. The final refined magnetic moment of the Cr atoms is $m_x = 2.675$, $m_y = -0.079$, $m_z = -1.530$ in μ_B with RF ~ 0.697.

REFERENCES

[1] J. K. Furdyna, J. Appl. Phys. 64, R29 (1988)

[2] A. Macdonald, P. Schi_er and N. Samarth, Nat. Mat. 4, 195 (2005)

[3] S. Kurodai, N. Nishizawa, K. Takita, M. Mitome, Y. Bando, K. Osuch and T. Dietl, Nat. Mat. 6, 440 (2007)

[4] A. Nazmul, S. Sugahara, and M. Tanaka, Phys. Rev. B 67, 241308 (2003)

[5] H. Munekata, H. Ohno, R. R. Ruf, R. J. Gambino, and L. L. Chang, J. Cryst. Growth. 111, 1011 (1991)

[6] H. Ohno, H. Munekata, S. von Molnar, and L. Chang, J. Appl. Phys. 69, 6103 (1991)

[7] H. Akai, Phys. Rev. Lett. 81, 3002 (2004)

[8] Jurgen Konig, Hsiu-Hau Lin, and Allan H. MacDonald, Phys. Rev. Lett. 84, 5628 (2000)

[9] A. Van Esch, L. Van Bockstal, J. De Boeck, G. Verbanck, A. S. van Steenbergen, P. J. Wellmann, B. Grietens, R. Bogaerts, F. Herlach, and G. Borghs, Phys. Rev. B 56, 13103 (1997)

[10] H. Saito, V. Zayets, S. Yamagata, and K. Ando, Phys. Rev. Lett. 90, 207202 (2003)

[11] T. Pekarek, D. Arenas, B. Cooker et al., J. Appl. Phys. 95, 7178 (2004)

[12] S. P. Patel, J.C. Pivin, A.K. Chawla, R. Chandra, D. Kanjilal, and L. Kumar, J. Magn. Magn. Mater. 323, 2734 (2011)

[13] W. Mac, A. Twardowski and M. Demianiuk, Phys. Rev. B 54, 5528 (1996)

[14] B. E. Larson, K. C. Hass, H. Ehrenreich, and A. E. Carlsson, Phys. Rev. B 37, 4137 (1988)

III. SELF-INTERCALATION TUNABLE INTERLAYER EXCHANGE COUPLING IN A SYNTHETIC VAN DER WAALS ANTIFERROMAGNET

Xiaoqian Zhang, Wenqing Liu, Wei Niu, Qiangsheng Lu, Wei Wang, Ali Sarikhani, Xiaohua Wu, Chunhui Zhu, Jiabao Sun, Mitchel Vaninger, Paul. F. Miceli, Jianqi Li, David J. Singh, Yew San Hor, Yue Zhao, Chang Liu, Liang He,* Rong Zhang,* Guang Bian,* Dapeng Yu, and Yongbing Xu*

ABSTRACT

One of the most promising avenues in 2D materials research is the synthesis of antiferromagnets employing 2D van der Waals (vdW) magnets. However, it has proven challenging, due in part to the complicated fabrication process and undesired adsorbates as well as the significantly deteriorated ferromagnetism at atomic layers. Here, the engineering of the antiferromagnetic (AFM) interlayer exchange coupling between atomically thin yet ferromagnetic $CrTe_2$ layers in an ultra-high vacuum-free 2D magnetic crystal, Cr_5Te_8 is reported. By self-introducing interstitial Cr atoms in the vdW gaps, the emergent AFM ordering and the resultant giant magnetoresistance effect are induced. A large negative magnetoresistance (10%) with a plateau-like feature is revealed, which is consistent with the AFM interlayer coupling between the adjacent $CrTe_2$ main layers in a temperature window of 30 K below the Néel temperature. Notably, the AFM state has a relatively weak interlayer exchange coupling, allowing a switching between the interlayer AFM and ferromagnetic states at moderate magnetic fields. This work represents a new route to engineering low-power devices that underpin the emerging spintronic technologies, and an ideal laboratory to study 2D magnetism.

Keywords: Cr_5Te_8 single crystal, Giant magnetoresistance, Ferromagnetism, ZnCrTe single crystals, Antiferromagnet (AFM), Spintronics, 2D van der Waals (vdW) magnet, Self-intercalation.

1. INTRODUCTION

The development of engineered multilayers composed of magnetic and non-magnetic materials at nanoscale paved the way for the creation of more complicated devices. [1,2] By stacking such thin films in multilayers, one can create layered heterostructures with properties that are fundamentally distinct from those of the constitutive bulk materials. For instance, these multilayers enable the spin valves and magnetic tunnel junctions to perform high-density and nonvolatile memories.[3,4] To realize spin-polarized scattering/tunneling, one has to create an opportunity to reorient the spin of two successive ferromagnetic (FM) layers and achieve the antiferromagnetic (AFM) interlayer coupling, which is well explained with the Ruderman–Kittel–Kasuya–Yosida (RKKY) model.[5] In this model, localized spins in two FM layers interact with conduction electrons through contact exchange potential, which oscillates with the distance between them. The magnetic coupling between adjacent magnetic layers, determined by the exchange potential, therefore can be tuned by varying the thickness of the nonmagnetic spacer layers. [6,7] Due to the mechanism of AFM interlayer coupling between adjacent FM layers, memory device designs based directly on antiferromagnets have been demonstrated. Antiferromagnets offer the benefit of being insensitive to disruptive magnetic fields while emitting no stray fields as compared to ferromagnets. In contrast to

bulk antiferromagnets with large exchange fields, synthetic antiferromagnets contain a relatively low interlayer exchange coupling strength, making them ideal for studying field-induced magnetic switching.[8] At present, synthetic antiferromagnets made of transition metals have been achieved, nevertheless, the magnetic switching in synthetic antiferromagnets with van der Waals (vdW) multilayers has only been seen on rare occasions.[4,9] For this purpose, the ferromagnetism of FM layers must be maintained at atomic scale thickness. Rich varieties of magnetic and electronic properties of 2D vdW magnets offer new options in memory computing technologies, owing to the pronounced perpendicular magnetic anisotropy (PMA) and long-range magnetic order in their ultrathin limits. [10–12] Strong covalent bonds provide an in-plane stability of 2D magnets, whereas vdW forces and the resultant relatively weak coupling enable the interlayer spin re-orientations. One example is the 2D magnetic semiconductor chromium tribromide (CrBr3) with different types of stacking orders, enabling realization of either AFM or FM phases.[13] Isostructural with $CrBr_3$, CrI_3-based spin-filter magnetic tunnel junctions demonstrate an extremely large magnetoresistance (MR), with the benefit of intrinsic AFM interlayer coupling.[4] Meanwhile, antisymmetric MR has been observed in Fe_3GeTe_2/graphite/ Fe_3GeTe_2 vdW heterostructures, resulting from the spin momentum locking at the interface.[14] Utilizing the vdW gap as the spacer layer, spin valves have been realized in Fe_3GeTe_2 homojunctions with a relatively low giant magnetoresistance (GMR) ratio,[15] which could be originated from the interfacial contamination during the device fabrication. In spite of the exciting progress in vdW heterostructure devices, the limitation of complicated fabrication process and interface damages occur inevitably, and the intrinsic tuning of magnetic interlayer coupling in vdW magnets remains elusive. To

achieve the AFM interlayer exchange coupling in vdW multilayers, a promising candidate is the self-intercalated 2D magnet or quasi-2D magnet, Cr_5Te_8. The Cr_5Te_8 single crystals can be regarded as a stack of alternating $CrTe_2$ and Cr intercalated layers, as shown in Figure 1a. Within the FM host layer, $CrTe_2$ is composed of Te–Cr–Te sandwich layers stacking along c-axis, and Cr atoms are covalently bonded by six nearest-neighboring Te atoms with octahedral coordination. By intercalating Cr atoms into the vdW gap, the $CrTe_2$–Cr–$CrTe_2$ stacking is formed, which is supposed to alter the FM exchange coupling of the $CrTe_2$–$CrTe_2$. Tuning of magnetic interlayer coupling in 2D vdW magnets has so far only been observed by the exfoliation of atomic layers, the electrostatic doping, as well as the substitution of atoms on chromium trihalides with a relatively low Curie temperature (TC).[10,16,17] Recently, room-temperature ferromagnetism has been demonstrated in 2D ferromagnet $CrTe_2$ in the form of both bulk and exfoliated thin flakes.[18] Notably, the FM ordering is well preserved in $CrTe_2$ epitaxial thin films with thickness down to monolayer.[19] By means of the self-doping, Cr_5Te_8 has been reported as a weak itinerant ferromagnet with a strong PMA.[20,21] Moreover, its TC can be well manipulated by intercalating more Cr atoms due to the competition of AFM and FM coupling.[22] In this work, we demonstrate the engineering of an AFM phase associated with AFM interlayer exchange coupling in the Cr_5Te_8 vdW magnetic crystal, which functions as a self-assembled quasi-2D spin valve.

2. RESULTS AND DISCUSSION

Self-intercalated Cr_5Te_8 single crystals were synthesized using self-flux method

(see Experimental Section). As exhibited in Figure 1a, cross-sectional scanning transmission electron microscopy (STEM) high-angle annular dark-field (HAADF) images indicate the layered trigonal crystal structure.[23] The quasi-2D layered feature is also verified by atomic force microscopy characterization on exfoliated few-layer Cr_5Te_8 flakes (Figure S1, Supporting Information). The microscopic topography taken from the surface of few-layer Cr_5Te_8 flakes shows atomically flat terraces, demonstrating the layered structure of Cr_5Te_8. The high degree of crystallinity of Cr_5Te_8 is confirmed by the selected area electron diffraction (SAED) pattern (Figure S2, Supporting Information), which could be indexed according to a trigonal crystal structure with lattice parameters of a = 7.92 Å, and c = 5.98 Å. The reduced c of Cr_5Te_8 relative to that of non-intercalated $CrTe_2$ (6.10 Å) suggests an increase of the coupling along c direction, and the significant bonding of the intercalated atoms as well. Thus, it is rather interesting to investigate the interlayer magnetic coupling, as the c-axis lattice constant is reduced by ≈ 2% after inserting Cr atoms between adjacent $CrTe_2$ layers. Parental $CrTe_2$ has a 2D character, where vdW-type interlayer exchange coupling stabilizes a FM ground state.[24] The excess Cr atoms sit interstitially between $CrTe_2$ host layers and serve multiple functions, specifically, donating charge to the main layers to create new electronic order and modifying the bonding of the compound as well as the interlayer exchange coupling.

To verify the local electronic correlation and magnetic ground state of Cr_5Te_8, [25,26] a typical pair of X-ray absorption spectroscopy (XAS) and X-ray magnetic circular dichroism (XMCD) spectra at Cr $L_{2,3}$ edge was obtained at 5 K under a magnetic field of 2 T (Figure 1b). XAS exhibits remarkable multiple-peak features, which are separated by 1.3 eV at spin– orbit core levels.

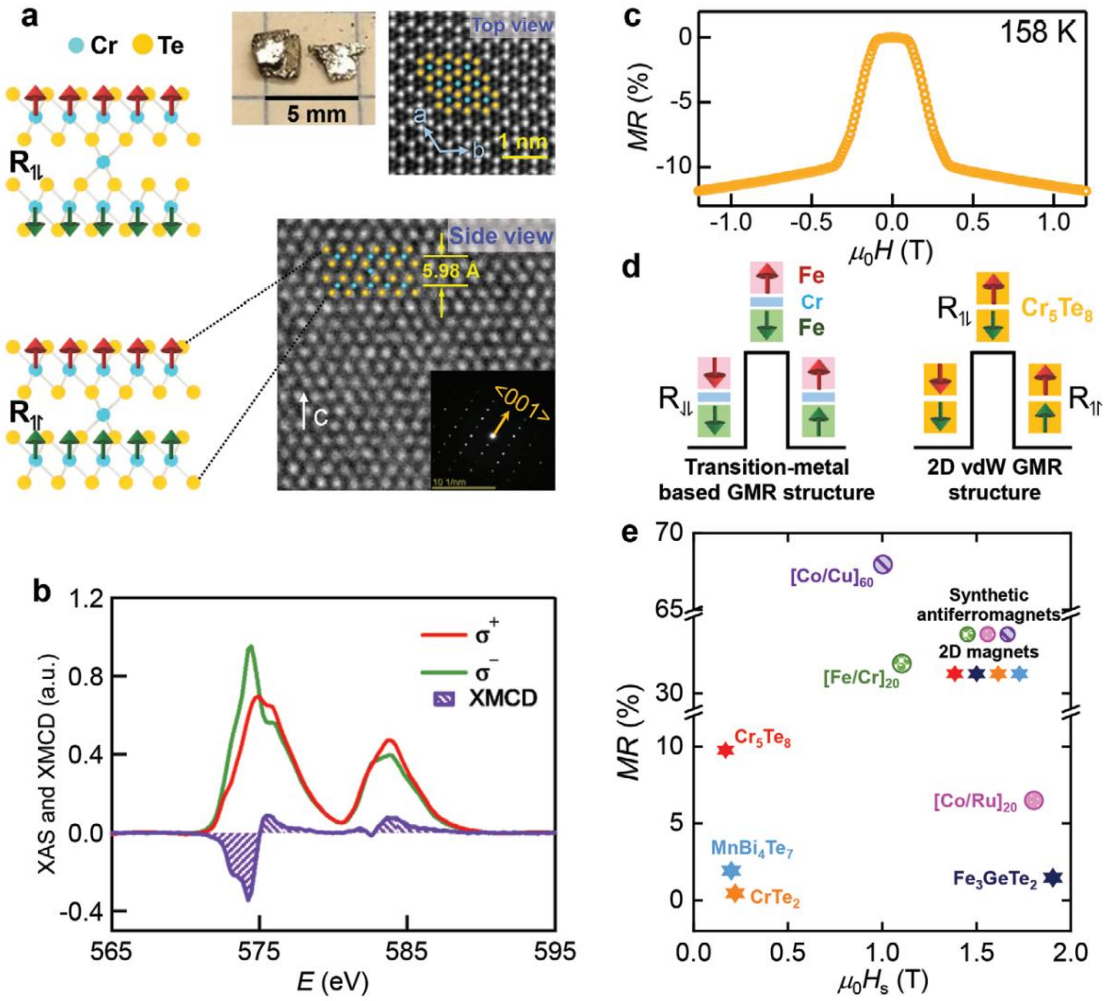

Figure 1. Crystal structure, magnetic structure, and MR of Cr_5Te_8. a) Crystal structure showing bilayer $CrTe_2$ with Cr atoms intercalated between the vdW gap. Spheres represent Te (yellow) and Cr (cyan) atoms with arrows representing interlayer magnetic exchange couplings. HAADF images from top view and side view show a trigonal lattice structure. Top panel: photo of Cr_5Te_8 single crystals. b) A typical pair of XAS for opposite circular polarizations and XMCD spectrum obtained with a magnetic field of 2 T at 5 K. c) MR curve as a function of magnetic field at 158 K. d) Schematic illustration of the transition-metal based GMR structure and the 2D vdW GMR structure. e) Plot of the MR ratio versus the saturation magnetic field (H_s), covering classic synthetic antiferromagnets ($[Co/Cu]_{60}$ (ref. [30]), $[Fe/Cr]_{20}$ (ref. [7]), $[Co/Ru]_{20}$ (ref. [7])) and 2D magnets ($MnBi_4Te_7$ (ref. [31]), Fe_3GeTe_2 (ref. [32]), $CrTe_2$ (ref. [23]), Cr_5Te_8 (this work)).

The spectral line shape resembles that of pure $CrTe_2$ thin layers,[19] suggesting that Cr^{3+} cations predominate in Cr_5Te_8. The sizable XMCD spectrum, obtained by taking the difference of XAS, manifests the intrinsic FM ground state. There is a good agreement between Cr_5Te_8 and $CrTe_2$ in both XAS and XMCD spectral line shapes, indicating that the ferromagnetism of Cr_5Te_8 mainly originate from $CrTe_2$ main layers. Furthermore, effects of self-intercalation on the magneto-transport properties were investigated (Figure 1c). Remarkably, a plateau-like feature and a large negative MR with magnitude exceeding ≈ 10% (0.5 T) at 158 K are observed, suggesting a distinct spin configuration in this plateau region. The high- and low-MR state could be interpreted in a manner qualitatively similar to the case of the "turn off" and "turn on" state, respectively, in a standard GMR spin valve device. Considering the low resistance along both in-plane and out-of-plane direction (Figure S3, Supporting Information), the possibility of a tunnel magnetoresistance effect could be ruled out.[4] When sweeping magnetic field, magnetization directions of the adjacent $CrTe_2$ host layers can have either a parallel or antiparallel alignment configuration due to the existence of the intercalated layers, providing evidence of the GMR effect and the resultant spin valve in Cr_5Te_8. Figure 1d presents schematics of the transition-metal based GMR structure and 2D vdW GMR structure, where the antiparallel and parallel spin alignment give rise to high ($R_{\uparrow\downarrow}$) and low ($R_{\uparrow\uparrow}$) resistance, respectively. In the case of conventional synthetic GMR devices composed of transition metals and alloys, electrons travel through the entire ferromagnet/metal multilayer structures, and both bulk and interfacial spin scattering are involved.[27–29] In contrast, due to the fact that the thickness of the Cr_5Te_8 GMR structure (millimeters) is much larger than the electron mean free path (tens of nanometers), the electrons are not

able to pass through the entire structure to experience bulk spin scattering. Thus, the spin scattering only occurs at the interface between $CrTe_2$ main layers and the vdW gap, which could be viewed as current channels and the spacer layer, respectively. By satisfying the condition of mean free path larger than the thickness of the spacer layer combined with adjacent $CrTe_2$ layers, electrons are able to travel through both $CrTe_2$ layers and the space layer to experience interfacial spin scattering. For comparison, we made a plot of the MR ratio versus the magnetic field for classic synthetic antiferromagnets and 2D magnets (Figure 1e). The Cr_5Te_8 single crystal, as a synthetic vdW antiferromagnet, possesses a comparable MR ratio with that of conventional synthetic antiferromagnet such as $[Co/Cu]_{60}$, [30] $[Co/Ru]_{20}$, and $[Fe/Cr]_{20}$, [7] but requires a lower saturation magnetic field. In addition, among 2D magnets including $MnBi_4Te_7$, [31] Fe_3GeTe_2, [32] and $CrTe_2$, [23] Cr_5Te_8 shows a pronounced intrinsic GMR ratio as observed in this work. The emergent antiparallel spin configuration in self-intercalated Cr_5Te_8 indicates the existence of extra magnetic states, apart from the FM phase in $CrTe_2$. [18] The magnetic order was revealed by monitoring the temperature and field dependent magnetization. Figure 2a shows the temperature dependent magnetization (M–T) curves with an applied magnetic field perpendicular to the sample surface.

The magnetization shows a general trend of decreasing with the increase of temperature, demonstrating a FM behavior with a T_C of ≈150 K. Above T_C, a cusp-like feature is observed in the M–T curve, exhibiting a typical AFM property with a Néel temperature (T_N) of 180 K. As the magnetic field increases, T_N shifts to lower temperature, and disappears when the field exceeds 0.5 T (inset of Figure 2a).

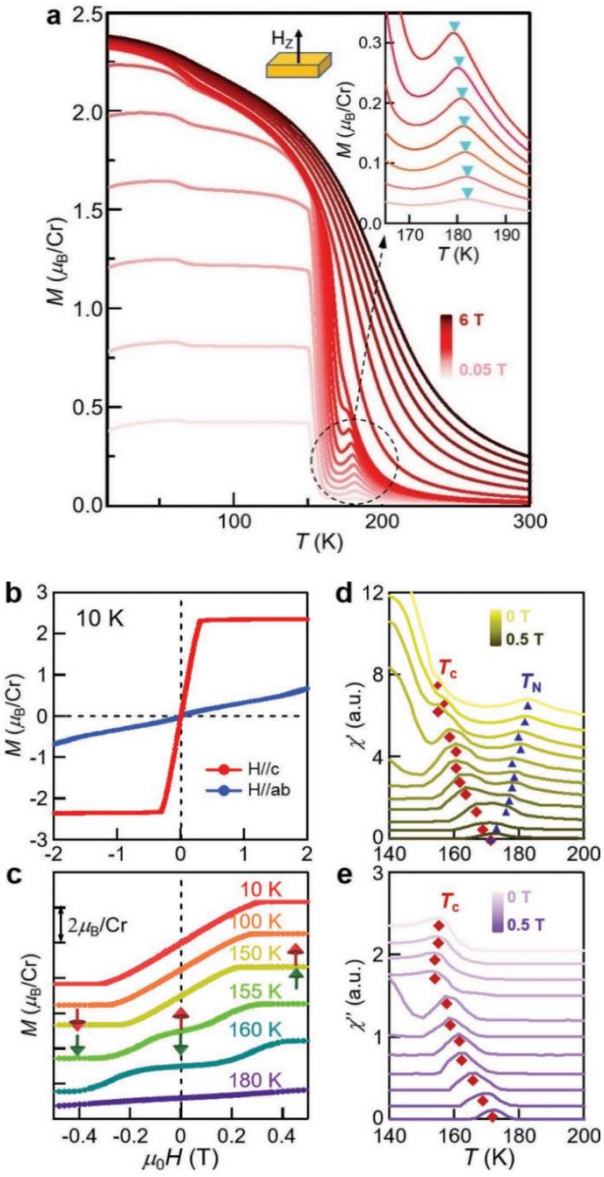

Figure 2. Demonstration of emergent AFM phase. a) Temperature dependence of the out-of-plane magnetic moment with the magnetic field ranging from 0.05 to 6 T. Samples were cooled down to 15 K without magnetic field and data was collected in the warming-up cycle. The platform-like feature and Curie-like behavior indicate that the 2D FM ordering within layers develops first. Besides, cusp-like features near 180 K (top inset) suggest development of the AFM ordering. b) Out-of-plane and in-plane magnetic hysteresis loops at 10 K, suggesting a strong PMA. c) Hysteresis loops at indicated temperatures with magnetic field along c-axis. The magnetization switching behavior at representative magnetic fields are schematically shown as insets. d, e) Temperature-dependent χ' and χ'' of AC susceptibility measured along out-of-plane direction. Phase boundaries of T_C and T_N determined from the susceptibility are illustrated by red squares and blue triangles.

In addition to M–T curves, the magnetic hysteresis loops also indicate the FM nature when the temperature is below T_C. As shown in Figure 2b, the out-of-plane magnetic moment increases linearly and saturates at a relatively low magnetic field (below 0.3 T). The saturated magnetic moment (M_s) per Cr atom and coercive field is determined to be 2.3 μ_B and 0.01 T at 10 K, respectively. An itinerant nature appears to be the reason of the discrepancy from the $M_s = 3\ \mu_B$ expected under an ionic model. In contrast, the in-plane magnetization does not saturate even with a strong magnetic field of 5 T (Figure S7, Supporting Information). This demonstrates a strong PMA, which is related to the strong overlap of Cr–Cr $3d_{z^2}$ and Cr 3d–Te 5p-orbitals along the perpendicular direction. Remarkably, when the temperature is above T_C, a plateau feature appears in the hysteresis loops at low field region (Figure 2c), indicative of an AFM coupling with almost vanishing magnetic moment. This plateau feature is also a signature of magnetic anisotropy, echoing the PMA discussed above. Further increasing the field, the AFM order is suppressed, and a spin-flip transition occurs. The AFM phase is preserved at a higher field with elevated temperature, and disappears with temperature above T_N. Because of the weak quasi-vdW interlayer exchange coupling, the magnetic properties can be easily modified by applying a low magnetic field or varying the temperature. To further investigate the magnetic states, we measured the temperature-dependent AC susceptibility under different out-of-plane fields. The real part (χ') and imaginary part (χ'') of magnetic susceptibility under magnetic field ranging from 0 to 0.5 T with a step of 0.05 T are presented in Figure 2d, e, respectively. χ' exhibits an extra peak (marked by blue triangles) beside the FM peak (red squares), while only a FM peak shows up in χ'' within the identical temperature scope. The prominent χ' and absent χ'' of the anomaly in the magnetization curve is another evidence

of an AFM character. The intriguing AFM ordering makes Cr_5Te_8 promising for engineering spin valve devices. Accordingly, electrical properties under magnetic field along the easy axis at various temperatures were assessed systematically (Figure 3a). The temperature dependent longitudinal resistance, R, decreases upon cooling (Figure 3b), indicating a typical metallic behavior. It is consistent with the band structure measured by angle-resolved photoemission spectroscopy (ARPES) where the Fermi level is located in the valence band (Figure S10, Supporting Information). As shown in Figure 3c, the magnitude of MR curves below T_C is ≈ 0.6% at 0.5 T, comparable with that of $CrTe_2$ thin flakes.[23] Notably, a sharp peak, corresponding to a large negative MR, appears at a low field when the temperature is close to T_C. With continuously increasing temperature, this peak becomes broad, and a plateau appears, which is a signature of a magnetic phase transition.[33] It is in good agreement with the emergent AFM phase shown in previous magnetization measurements. The antiparallel alignment of the magnetization in the AFM phase produces an appreciable increase of the resistance, consistent with the phenomenon observed in spin valves.[1,2] In the plateau region with AFM ordering, electrons suffer a high scattering ratio and the conductivity is suppressed.[2,31] Increasing the field, the resistance drops sharply during the process from AFM phase to FM phase, among which the transmitting electrons with the same spin direction as $CrTe_2$ layers can pass freely.

Further increasing the field, there is another slope change in the MR curves at high fields (for example, at 155 K and 0.28 T in Figure 3d, at 160 K and 0.38 T in Figure 3e), which is due to the saturation of magnetization.[34] Consistent with pure $CrTe_2$ compound, the ground state of Cr_5Te_8 is FM,[24] whereas the self-intercalation gives rise to the AFM phase at elevated temperatures.

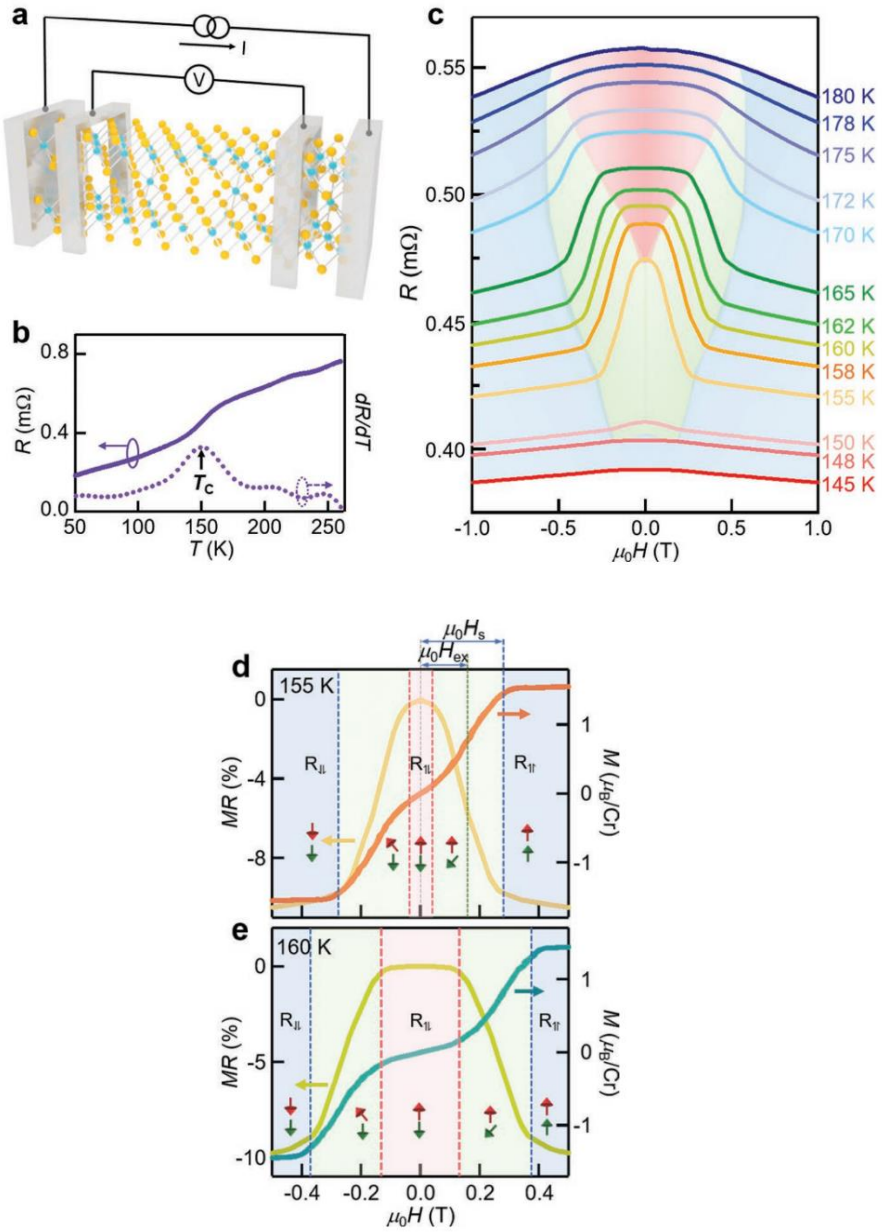

Figure 3. AFM interlayer exchange coupling in Cr_5Te_8 spin valves. a) Schematic diagram of transport measurements. b) Temperature dependent longitudinal resistance and its differential, dR/dT, exhibiting a kink at $T_C \approx 150$ K. c) Longitudinal resistance versus out-of-plane magnetic field. There is a rapid increasement of MR once entering into the AFM state. With further increasing temperature, the MR decreases and vanishes above T_N. d) Comparison of field dependent MR (yellow line) and magnetic moment M (orange line) at 155 K, demonstrating the slope change at higher field due to the saturated magnetization. The MR ratio is defined as $[\rho(H)-\rho(0)]/\rho(0)$. e) Slope change of field dependent MR (light green line) and magnetic moment M (green line) at 160 K, suggesting a phase transition.

Now we address the possible origins of this magnetic transition. The first mechanism that could lead to the observed AFM behavior is the formation of spin glass. In order to verify this possibility, frequency-dependent AC susceptibility was measured along c-axis (Figure S9, Supporting Information). The peak position of susceptibility curves (≈180 K) is independent of frequency, different from the frequency-dependent one found in spin glasses.[35] In addition, a helical AFM state could result in such a phenomenon as well.[36] The in-plane easy axis is usually a common feature of helical AFM states, contradictory to the observation of strong PMA in Cr_5Te_8. As a result, the potential of a helical AFM state could be ruled out. Another possible mechanism responsible for the AFM phase is the antiparallel interlayer coupling between adjacent $CrTe_2$ layers. Trace back to the source, the exchange interaction mechanisms of both intralayer and interlayer play a vital role in the magnetic ordering. AFM direct exchange interaction through t_{2g} orbitals and the FM Cr–Te–Cr super exchange interaction contribute to the magnetic coupling of intralayer. On the other hand, directional hybridization between Cr 3d-orbitals and Te 5p-orbitals gives rise to the interlayer super exchange coupling, which depends on the bond angles and bond distances of Cr–Te–Te–Cr path.[37] In addition, coupling through intercalated Cr is also worthy of consideration. According to previous reports, the lattice constant of $CrTe_2$ bulk along c-axis is 6.10 Å. [38] Strikingly, the vertical distance between $CrTe_2$ main layers dropped to 5.98 Å with interlayer Cr doping (Figure S2, Supporting Information). Notably, the distance between two nearest-neighbor Cr atoms plays an important role in determining the magnetic states. It has been theoretically predicted that the magnetic properties of $CrSiTe_3$ and $CrGeTe_3$ can be manipulated by modifying atomic distance under moderate strain.[39,40] Based on the

RKKY model, the interlayer magnetic coupling energy oscillates as a function of the nonmagnetic layer thickness in synthetic AFM multilayers.[7,41] Considering the temperature dependence of lattice constant included in Figure S13 (Supporting Information), the interlayer distance in a temperature window of 150–180 K may favor the antiparallel alignment among $CrTe_2$ main layers. Similarly, the oscillatory behavior of the interlayer exchange interaction versus the interlayer separation has also been revealed in the vdW $(Fe_{1-x}Cox)_4GeTe_2$ magnets.[42] Besides, the variation of carrier density (n) can also be responsible for the AFM phase. The temperature dependence of n, GMR ratio and the AFM interlayer coupling strength (J_{AFM}) are summarized in Figure 4a. There is an apparent increase of n once entering the AFM phase, while it drops from the peak value of $1.09 \times 1023\ cm^{-3}$ at 160 K to $1.07 \times 1022\ cm^{-3}$ at the AFM phase boundary. In the itinerant Cr_5Te_8 system, the local spins and itinerant electrons are entangled with each other, which governs the spin dynamics.[43] The emergent AFM spin configuration is expected to also depend on the abrupt increase of n, while the exact exchange mechanism between conduction electrons and local spins remains to be investigated. Actually, the coupling between the magnetism and carriers is not limited to $CrTe_2$ compounds, but also applicable to magnetic topological insulators $Mn(Bi_{1-x}Sb_x)_4Te_7$ with magnetic phase transitions induced by a charge carrier engineering.[44]

A notable observation in Figure 4a is that there is a rapid increase of the MR ratio once entering into the AFM state. With further increasing temperature, the GMR magnitude decreases and vanishes above the T_N, which presumably arises from two main contributions. The first one is the increased spin fluctuation at high temperature. [45,46]

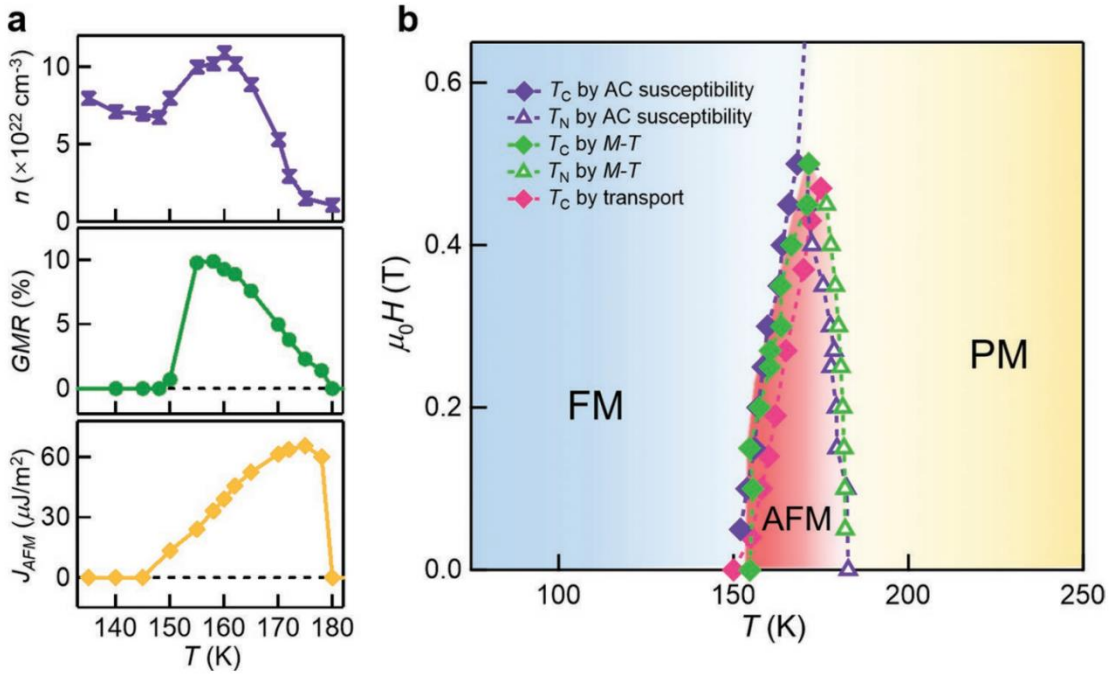

Figure 4. Temperature and magnetic field dependent magnetization reversal. a) Temperature dependence of the n, the GMR ratio and the J_{AFM}. b) Compiled magnetic field-temperature phase diagram. The green, purple, and pink symbols represent the critical points extracted from M–T curves, AC susceptibility, and electrical transport, respectively.

The other contribution comes from the reduced mean free path of electrons due to temperature dependent magnon scattering, phonon scattering and interfacial scattering. Despite GMR is related to the AFM coupling, J_{AFM} ($J_{AFM} = \mu_0 H_{ex} M_s t_{FM}$, where t_{FM} is the FM unit thickness and $\mu_0 H_{ex}$ represents the exchange field) shows an increasing trend with the increased temperature first, then reaches a peak of 66 μJ m^{-2} at 175 K, and finally reduces sharply near the T_N (Figure 4a), which is different from the temperature response of GMR ratio. J_{AFM} is governed by contributions from the spacer layers, magnetic layers, and the interfaces. Near the T_C, the interlayer exchange coupling involves the transition from the FM mode to the AFM one at a higher temperature, resulting in an enhancement

of J_{AFM}. With further increasing temperature, the softening of the Fermi edge, complex reflection coefficients at the interface as well as collective excitations within the magnetic layers make the coupling mechanism less effective.[47] The quantified J_{AFM} is one or two orders of magnitude lower than those of typical synthetic antiferromagnets composed of transition metals such as Fe/Cr (1.02 × 104 μJ m^{-2}), Co/Ru (4.83 × 103 μJ m^{-2}), and Co/Cu multilayers (2.21 × 103 μJ m^{-2}).[48] This weak J_{AFM} in Cr_5Te_8 resolves the conundrum of how to obtain changes in magnetic order with a moderate field, a behavior typically associated with weak magnetic interactions. Based on the magnetization, susceptibility, and transport measurements, we plot the field-temperature phase diagram in Figure 4b. With the emergent AFM interlayer coupling, Cr_5Te_8 can be regarded as a magnetic order competing system. Below T_C, main layers are ferromagnetically stacked along both interlayer and intralayer direction, resulting in a negligible MR. In the temperature range between T_C and T_N, the FM ordering within each $CrTe_2$ layer remains, while the interlayer coupling between adjacent $CrTe_2$ layers turns into AFM, bringing about the intrinsic GMR effect. A merger of TC and TN curves at high fields is clearly seen in the phase diagram, which is due to the enforced alignment of Cr magnetic moment by the Zeeman field.[49] Above TN, the compound becomes paramagnetic, and the MR vanishes. The presence of self-intercalation tunes the interlayer magnetic coupling between $CrTe_2$ main layers, and thereby gives rise to the rich magnetic phase diagram. Apart from switching the interlayer coupling with an applied magnetic field, it is also possible to achieve analogous effects through varying temperature near the phase transition point.

3. CONCLUSIONS

In summary, we demonstrate an effective strategy to realize AFM interlayer exchange coupling through atomic-scale self-intercalation in crystal lattice. In particular, the antiparallel spins between adjacent $CrTe_2$ layers give rise to a pronounced GMR ratio and synthetic AFM phase in Cr_5Te_8 2D magnetic crystals, without requiring complex fabrication of multilayer structures. This technique could be extended to a broad class of 2D magnets to create potentially new mechanisms and properties. The experimental platform provides a hitherto unexplored but appealing approach to obtain the AFM interlayer exchange coupling, offering a new horizon in designing desired magnetic phases and engineering functional structures for 2D magnet-based spintronics.

4. EXPERIMENTAL SECTION

Growth of Cr_5Te_8 Single Crystals: High-quality Cr_5Te_8 single crystals were synthesized using self-flux method with high-purity elemental Cr (99.99%) and Te (99.999%) materials (from Alfa Aesar). A mixture of Cr and Te with an optimized molar ratio equivalent to 1:6 was sealed in evacuated quartz ampoules. Then it was heated up to 1050 °C and maintained for 1 day to allow sufficient homogenization, followed by slow cooling to 700 °C for a period of 1 week. Once the furnace reached 700 °C, the excess flux was removed from the crystals by centrifugation. It needs to be mentioned here that the growth method and parameters are different from those of $CrTe_2$ [23] and $Cr_{1.2}Te_2$ single crystals [50] previously reported. The thicknesses of the Cr_5Te_8 bulk sample for magnetic and transport

measurements is 0.692 mm. Cr_5Te_8 bulk can be well preserved in ambient conditions for at least one month as its pristine ones. Structural and Magnetic Characterization: The crystal structure was examined by a high-resolution single crystal X-ray diffractometer (Bruker D8 Discover). The incident X-ray is from Cu-Kα emission and has a wavelength of 1.5418 Å. The scan mode is θ-2θ. The magnetization and susceptibility measurements were performed using a Quantum Design superconducting quantum interference device (SQUID) magnetometer with a base temperature 2 K and magnetic field up to 7 T. The magneto-transport devices were confined to the Hall-bar geometry using the standard four-point probe method with room temperature cured silver paste as contacts. The MR measurements were performed on a Quantum Design Physical Property Measurement System (PPMS) with a base temperature 2 K and magnetic field up to 9 T. X-Ray Absorption Spectroscopy and X-Ray Magnetic Circular Dichroism: XAS and XMCD measurements at the Cr $L_{2,3}$ absorption edges in total-electron yield (TEY) mode were performed at beamline I10 at Diamond Light Source, U.K. Oppositely circular polarized X-rays with 100% polarization were used to resolve XMCD signals in normal incidence. The light-helicity was switched in a magnetic field of 2 T, which was applied at 90° with respect to the film plane and in parallel with the incident beam. The dichroic spectrum was obtained by taking the difference of XAS spectra, i.e., $\sigma^+ - \sigma^-$. Angle-Resolved Photoemission: After being cleaved in the load lock, the sample was transferred into the ARPES measurement chamber. ARPES measurements were performed with a SPECS PHOIBOS 150 hemisphere analyzer at 100 K with an energy resolution of 40 meV. A SPECS UVS 300 helium discharge lamp (He Iα = 21.2 eV) is used as the light source.

SUPPORTING INFORMATION

Supporting Information is available from the Wiley Online Library or from the author.

ACKNOWLEDGMENTS

X.Z., W.L., and W.N. contributed equally to this work. This work was supported by the National Key Research and Development Program of China (No. 2016YFA0300803, No. 2017YFA0206304), the National Basic Research Program of China (No. 2014CB921101), the National Natural Science Foundation of China (No. 61427812, 11774160, 11574137, 61474061, 61674079), Jiangsu Shuangchuang Program, the Natural Science Foundation of Jiangsu Province of China (No. BK20140054, BK20192006), UK EPSRC (EP/S010246/1), Leverhulme Trust (LTSRF1819\15\12), and Royal Society (IEC\NSFC\181680). X.Z. acknowledges the support of the fellowship of China Postdoctoral Science Foundation (2021M701590). G.B. was supported by the US National Science Foundation (NSF-DMR#1809160). Work of D.S. was supported by the U.S. Department of Energy, Basic Energy Sciences, Award Number DE-SC0019114. W.N. was supported by the Natural Science Foundation of China (Grant No. 11904174), Natural Science Foundation of Jiangsu Province (Grant No. BK20190729), NUPTSF (Grant No. NY220203). Diamond Light Source is acknowledged to I10 under proposal MM22532. The authors acknowledge the assistance of SUSTech Core Research Facilities.

REFERENCES

[1] M. N. Baibich, J. M. Broto, A. Fert, F. Nguyen Van Dau, F. Petroff, P. Etienne, G. Creuzet, A. Friederich, J. Chazelas, Phys. Rev. Lett. 1988, 61, 2472.

[2] G. Binasch, P. Grunberg, F. Saurenbach, W. Zinn, Phys. Rev. B 1989, 39, 4828.

[3] J. S. Moodera, L. R. Kinder, T. M. Wong, R. Meservey, Phys. Rev. Lett. 1995, 74, 3273.

[4] T. Song, X. Cai, W.-Y. M. Tu, X. Zhang, B. Huang, N. P. Wilson, K. L. Seyler, L. Zhu, T. Taniguchi, K. Watanabe, M. A. McGuire, D. H. Cobden, D. Xiao, W. Yao, X. Xu, Science 2018, 360, 1214. L. (2013). *Microsoft Word 2013 bible* (4th ed.). Indianapolis, Ind: John Wiley & Sons, Inc.

[5] Q. Y. Jin, Y. B. Xu, H. R. Zhai, C. Hu, M. Lu, Q. S. Bie, Y. Zhai, G. L. Dunifer, R. Naik, M. Ahmad, Phy. Rev. Lett. 1994, 72, 768.

[6] D. M. Edwards, J. Mathon, R. B. Muniz, M. S. Phan, Phys. Rev. Lett. 1991, 67, 493.

[7] S. S. Parkin, N. More, K. P. Roche, Phys. Rev. Lett. 1990, 64, 2304.

[8] S. G. te Velthuis, J. S. Jiang, S. D. Bader, G. P. Felcher, Phys. Rev. Lett. 2002, 89, 127203.

[9] H. H. Kim, B. Yang, S. Li, S. Jiang, C. Jin, Z. Tao, G. Nichols, F. Sfigakis, S. Zhong, C. Li, S. Tian, D. G. Cory, G. X. Miao, J. Shan, K. F. Mak, H. Lei, K. Sun, L. Zhao, A. W. Tsen, Proc. Natl. Acad. Sci. USA 2019, 116, 11131.

[10] B. Huang, G. Clark, E. Navarro-Moratalla, D. R. Klein, R. Cheng, K. L. Seyler, D. Zhong, E. Schmidgall, M. A. McGuire, D. H. Cobden, W. Yao, D. Xiao, P. Jarillo-Herrero, X. Xu, Nature 2017, 546, 270.

[11] C. Gong, L. Li, Z. Li, H. Ji, A. Stern, Y. Xia, T. Cao, W. Bao, C. Wang, Y. Wang, Z. Q. Qiu, R. J. Cava, S. G. Louie, J. Xia, X. Zhang, Nature 2017, 546, 265.

[12] C. Gong, X. Zhang, Science 2019, 363, 706.

[13] W. Chen, Z. Sun, Z. Wang, L. Gu, X. Xu, S. Wu, C. Gao, Science 2019, 366, 983.

[14] S. Albarakati, C. Tan, Z.-J. Chen, J. G. Partridge, G. Zheng, L. Farrar, E. L. H. Mayes, M. R. Field, C. Lee, Y. Wang, Y. Xiong, M. Tian, F. Xiang, A. R. Hamilton, O. A. Tretiakov, D. Culcer, Y.u-J. Zhao, L. Wang, Sci. Adv. 2019, 5, eaaw0409.

[15] C. Hu, D. Zhang, F. Yan, Y. Li, Q. Lv, W. Zhu, Z. Wei, K. Chang, K. Wang, Sci. Bull. 2020, 65, 1072.

[16] S. Jiang, L. Li, Z. Wang, K. F. Mak, J. Shan, Nat. Nanotechnol. 2018, 13, 549.

[17] T. A. Tartaglia, J. N. Tang, J. L. Lado, F. Bahrami, M. Abramchuk, G. T. McCandless, M. C. Doyle, K. S. Burch, Y. Ran, J. Y. Chan, F. Tafti, Sci. Adv. 2020, 6, eabb9379.

[18] L. Meng, Z. Zhou, M. Xu, S. Yang, K. Si, L. Liu, X. Wang, H. Jiang, B. Li, P. Qin, P. Zhang, J. Wang, Z. Liu, P. Tang, Y. Ye, W. Zhou, L. Bao, H. J. Gao, Y. Gong, Nat. Commun. 2021, 12, 809.

[19] X. Zhang, Q. Lu, W. Liu, W. Niu, J. Sun, J. Cook, M. Vaninger, P. F. Miceli, D. J. Singh, S.-W. Lian, T.-R. Chang, X. He, J. Du, L. He, R. Zhang, G. Bian, Y. Xu, Nat. Commun. 2021, 12, 2492.

[20] Y. Wang, J. Yan, J. Li, S. Wang, M. Song, J. Song, Z. Li, K. Chen, Y. Qin, L. Ling, H. Du, L. Cao, X. Luo, Y. Xiong, Y. Sun, Phys. Rev. B 2019, 100, 024434.

[21] C. Chen, X. Chen, C. Wu, X. Wang, Y. Ping, X. Wei, X. Zhou, J. Lu, L. Zhu, J. Zhou, T. Zhai, J. Han, H. Xu, Adv. Mater. 2022, 34, 2107512.

[22] L.-Z. Zhang, X.-D. He, A.-L. Zhang, Q.-L. Xiao, W.-L. Lu, F. Chen, Z. Feng, S. Cao, J. Zhang, J.-Y. Ge, APL Mater. 2020, 8, 031101.

[23] X. Sun, W. Li, X. Wang, Q. Sui, T. Zhang, B. Wang, Z. Han, X. Han, Z. Zhang, Nano Res. 2020, 13, 3358.

[24] H. Y. Lv, W. J. Lu, D. F. Shao, Y. Liu, Y. P. Sun, Phys. Rev. B 2015, 92, 214419.

[25] C. T. Chen, Y. U. Idzerda, H. Lin, N. V. Smith, G. Meigs, E. Chaban, G. H. Ho, E. Pellegrin, F. Sette, Phys. Rev. Lett. 1995, 75, 152.

[26] W. Liu, D. West, L. He, Y. Xu, J. Liu, K. Wang, Y. Wang, ACS Nano 2015, 9, 10237.

[27] S. M. Thompson, J. Phys. D: Appl. Phys. 2008, 41, 093001.

[28] S. S. Parkin, Phys. Rev. Lett. 1993, 71, 1641.

[29] L. Jogschies, D. Klaas, R. Kruppe, J. Rittinger, P. Taptimthong, A. Wienecke, L. Rissing, M. C. Wurz, Sensors-Basel 2015, 15, 28665.

[30] S. S. P. Parkin, Z. G. Li, D. J. Smith, Appl. Phys. Lett. 1991, 58, 2710.

[31] J. Wu, F. Liu, M. Sasase, K. Ienaga, Y. Obata, R. Yukawa, K. Horiba, H. Kumigashira, S. Okuma, T. Inoshita, H. Hosono, Sci. Adv. 2019, 5, eaax9989.

[32] Y. Wang, C. Xian, J. Wang, B. Liu, L. Ling, L. Zhang, L. Cao, Z. Qu, Y. Xiong, Phys. Rev. B 2017, 96, 134428.

[33] D. Liang, J. P. DeGrave, M. J. Stolt, Y. Tokura, S. Jin, Nat. Commun. 2015, 6, 8217.

[34] Q. Wang, S. Sun, X. Zhang, F. Pang, H. Lei, Phys. Rev. B 2016, 94, 075135.

[35] K. Binder, A. P. Young, Rev. Mod. Phys. 1986, 58, 801.

[36] S. Kobayashi, Phys. Rev. Lett. 2011, 106, 057207.

[37] N. Sivadas, S. Okamoto, X. Xu, C. J. Fennie, D. Xiao, Nano Lett. 2018, 18, 7658.

[38] C. D. Freitas, R. Weht, A. Sulpice, G. Remenyi, P. Strobel, F. Gay, J. Phys.: Condens. Matter 2015, 27, 176002.

[39] N. Sivadas, M. W. Daniels, R. H. Swendsen, S. Okamoto, D. Xiao, Phys. Rev. B 2015, 91, 235425.

[40] X. Li, J. Yang, J. Mater. Chem. C 2014, 2, 7071.

[41] S. S. P. Parkin, Annu. Rev. Mater. Sci. 1995, 25, 357.

[42] J. Seo, E. S. An, T. Park, S. Y. Hwang, G. Y. Kim, K. Song, W. S. Noh, J. Y. Kim, G. S. Choi, M. Choi, E. Oh, K. Watanabe, T. Taniguchi, J. Park, Y. J. Jo, H. W. Yeom, S. Y. Choi, J. H. Shim, J. S. Kim, Nat. Commun. 2021, 12, 2844.

[43] I. A. Zaliznyak, Z. Xu, J. M. Tranquada, G. Gu, A. M. Tsvelik, M. B. Stone, Phys. Rev. Lett. 2011, 107, 216403.

[44] B. Chen, F. Fei, D. Wang, Z. Jiang, B. Zhang, J. Guo, H. Xie, Y. Zhang, M. Naveed, Y. Du, Z. Sun, H. Zhang, D. Shen, F. Song, arXiv 2020, 2009, 00039.

[45] R. Kienberger, E. Goulielmakis, M. Uiberacker, A. Baltuska, V. Yakovlev, F. Bammer, A. Scrinzi, T. Westerwalbesloh, U. Kleineberg, U. Heinzmann, M. Drescher, F. Krausz, Nature 2004, 427, 817.

[46] J. Ventura, J. P. Araujo, J. B. Sousa, A. Veloso, P. P. Freitas, Phys. Rev. B 2008, 77, 184404.

[47] S. Schwieger, W. Nolting, Phys. Rev. B 2004, 69, 224413.

[48] S. S. Parkin, Phys. Rev. Lett. 1991, 67, 3598.

[49] Q. L. He, X. Kou, A. J. Grutter, G. Yin, L. Pan, X. Che, Y. Liu, T. Nie, B. Zhang, S. M. Disseler, B. J. Kirby, W. Ratcliff Ii, Q. Shao, K. Murata, X. Zhu, G. Yu, Y. Fan, M. Montazeri, X. Han, J. A. Borchers, K. L. Wang, Nat. Mater. 2017, 16, 94.

[50] M. Huang, L. Gao, Y. Zhang, X. Lei, G. Hu, J. Xiang, H. Zeng, X. Fu, Z. Zhang, G. Chai, Y. Peng, Y. Lu, H. Du, G. Chen, J. Zang, B. Xiang, Nano Lett. 2021, 21, 4280.

SUPPORTING MATERIALS

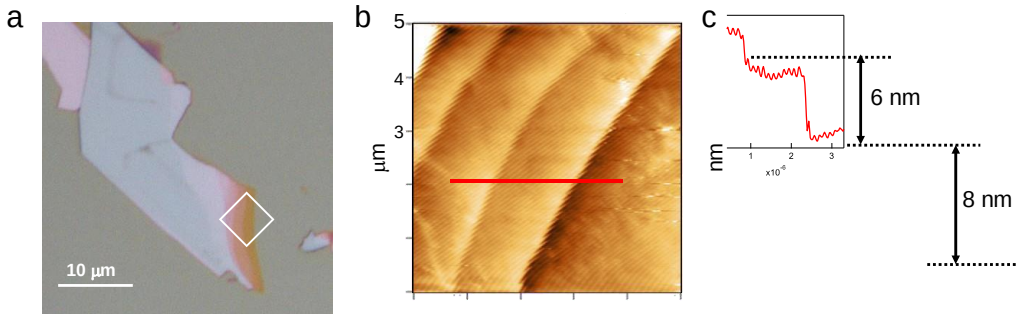

Figure S1. Atomic force microscopy characterization on exfoliated few-layer Cr_5Te_8 flakes. a) Optical image of typical Cr_5Te_8 thin flakes. The white box highlights the region for the atomic force microscopy measurement. b) Topography image of the selected thin flakes. c) Topography line profile taken along the red line in (b).

An optical image of exfoliated few-layer Cr_5Te_8 flakes is exhibited in Figure S1a. Regions of different thicknesses are clearly resolved by the optical contrast. The layer identification is corroborated by direct topography measurements with an atomic force microscope. The microscopic topography taken from the surface of few-layer Cr_5Te_8 flakes shows atomically flat terraces (Figure S1b). A Line profile extracted from the topography image exhibits the step heights between adjacent layers (Figure S1c). The measured step heights are 6 nm and 8 nm, corresponding to about 10 layers and 13 layers, respectively. Therefore, it is proved that Cr_5Te_8 is a quasi-2D layered material.

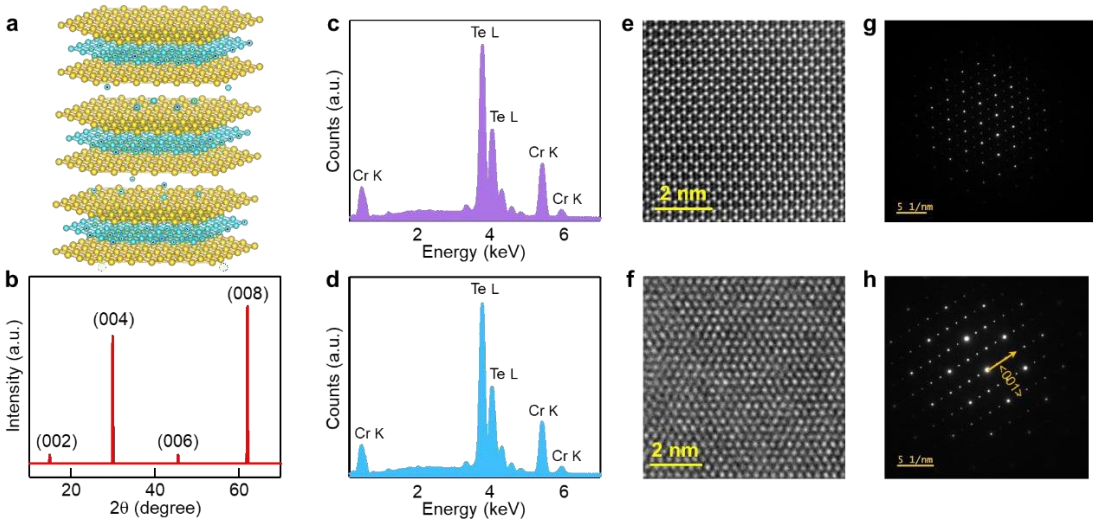

Figure S2. Elemental and structural characterization. a) Crystal structure of Cr_5Te_8, which can be considered as few Cr atoms intercalated between $CrTe_2$ layers. Cyan and yellow spheres correspond to Cr and Te atoms, respectively. b) XRD 2θ-ω scan, from which only (00*l*) peaks are detected. It indicates that the plate-shaped surface is parallel to the *ab* plane. The lattice constant (c = 5.98 Å) from XRD is identical with the STEM result. c,d) Energy dispersive spectroscopy (EDS) spectra give a consistent Cr:Te ratio of 5:8. e-h) HAADF image and SAED pattern from top view (e,g) and side view (f,h), showing the highly ordered structure with lattice parameters of a = 7.92 Å, and c = 5.98 Å. Note that Cr has a smaller atomic number than Te, leading to a lower intensity contribution.[1] The combination of XRD scan and TEM image confirms the single- crystalline Cr_5Te_8.

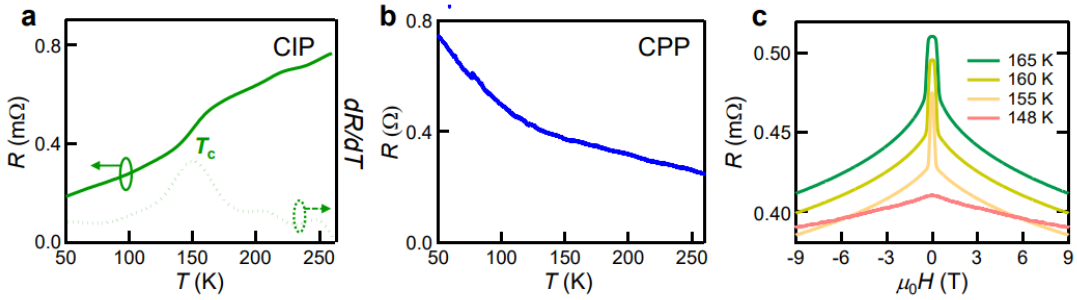

Figure S3. Temperature and field dependent resistance. a,b) Temperature dependence of current in-plane (CIP) resistance and current perpendicular-plane (CPP) resistance at zero field, showing a metallic and semiconducting behavior, respectively. The corresponding *dR*/*dT* exhibits a kink at T_C ~ 150 K. c) MR at high magnetic field, from which the slope change close to the transition temperature can be identified. Cr_5Te_8 in the FM phase exhibits a weak negative MR (for example, ~1.5% at 1 T at 148 K) at temperature below 150 K, and shows no sign of saturation up to 9 T.

For the out-of-plane ***M-T*** curves, the magnetization drops nearly vertically at ~150 K. On the contrary, for the in-plane ***M-T*** curves, an abrupt increase in magnetization is observed at the same temperature. Compared with the out- of-plane one, the absolute value of in-plane magnetization change is much smaller. It suggests a small portion of the magnetic moment flipping from the *c*-axis to the *ab*-plane at the critical temperature. As temperature increases, the thermal fluctuation weakens the out-of-plane anisotropy, which leads to the disordered arrangement of the magnetic moment. Therefore, the out-of-plane magnetization decreases. When the magnetic field is applied along in-plane direction, a small portion of the disordered magnetic moments rearrange in the *ab*-plane and the in-plane magnetization increases accordingly.[5]

To investigate the possibility of another magnetic phase form interstitial Cr atoms, we have conducted magnetic field and temperature dependent XAS and XMCD measurements at the Cr $L_{2,3}$ absorption edges.

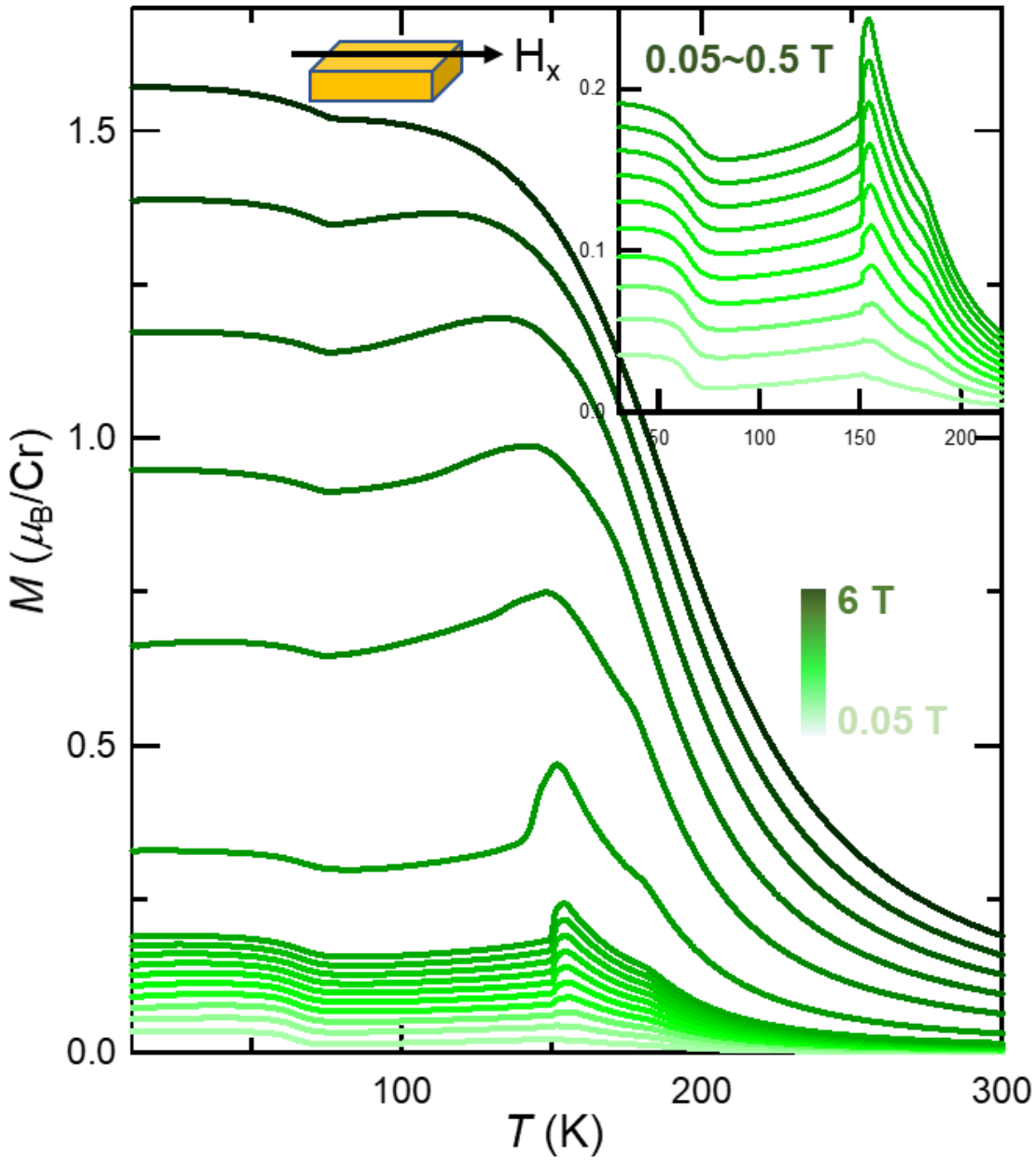

Figure S4. In-plane magnetic response. Temperature dependence of the magnetic moment with magnetic field ranging from 0.05 T to 6 T along in-plane direction. The in- plane magnetic moment is significantly smaller than the out-of-plane value. This suggests the existence of a uniaxial magnetic anisotropy, which is essential for the formation of 2D FM phase.[2-4] Apart from the FM order, the slow decrease of the magnetization below T_C is related to the canted AFM structure along the in-plane direction.[5] The canted AFM order is suppressed by the increasing external magnetic field.[6]

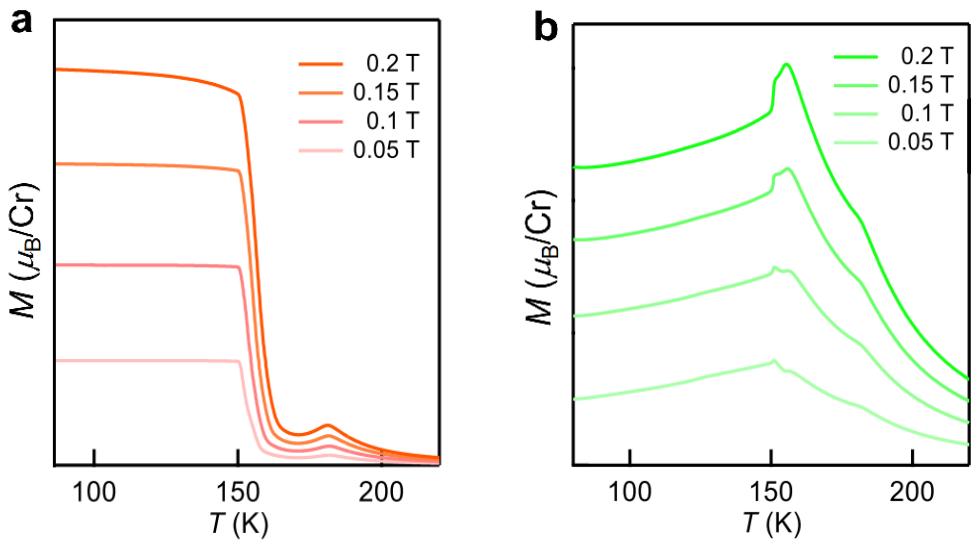

Figure S5. Temperature dependence of the out-of-plane (a) and in-plane (b) magnetic moment with field ranging from 0.05 T to 0.2 T.

As presented in Figure S6, the multiple- peak feature of XAS and XMCD resembles that of pure $CrTe_2$ thin layers and is related to the Cr^{3+} (d^3) configuration with half-filled t_{2g} states. It demonstrates that the intrinsic ferromagnetism of Cr_5Te_8 comes from Cr^{3+} ions, rather than other valence states. The XMCD measurements were repeated at elevated temperatures, and the dichroism was observable up to 200 K (Figure S6a). The multiple-peak feature of XMCD spectra remain unchanged with the rising temperature, despite the decreased intensity. Furthermore, the magnetic field dependent XMCD spectra were also revealed (Figure S6b). The XMCD line shape is invariable with the magnetic field ranging from 1 to 14 T. The consistent magnetic behavior under various magnetic fields and temperatures suggests that interstitial Cr atoms do not contribute to another magnetic phase.

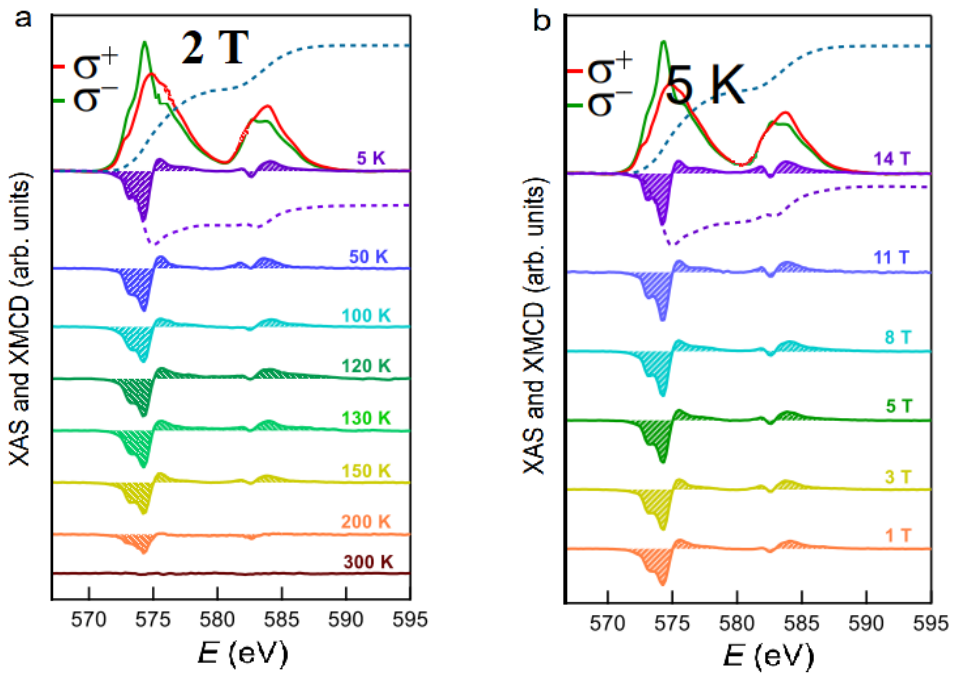

Figure S6. Magnetic field and temperature dependent XMCD characterization of Cr_5Te_8. a) Typical pairs of XAS and XMCD spectra of Cr_5Te_8 from 5 K to 300 K at a magnetic field of 2 T and the integrals at 5 K, where the dichroism at Cr L_3 edge can be traced to 200 K. b) Typical pairs of XAS and XMCD spectra from 1 T to 14 T at 5 K and the integrals at 14 T. XMCD spectra at different temperatures and magnetic fields are offset for clarify.

The AC magnetic susceptibility can be used as an indicator of magnetic phase transitions, and it can be written as

$$\chi_{ac} = \chi' - i\chi'', \tag{4}$$

where χ' and χ'' are the real and imaginary components of AC magnetic susceptibility, respectively. Figure S8 presents the temperature-dependent contour map of the AC susceptibility. If a peak exists in χ' and χ'' at the same location in the map, it is in a ferromagnetic phase. Therefore, the red line indicates the T_C of the FM phase. On the other hand, if a peak is present in χ' but absent in χ'', the system is in an AFM phase.

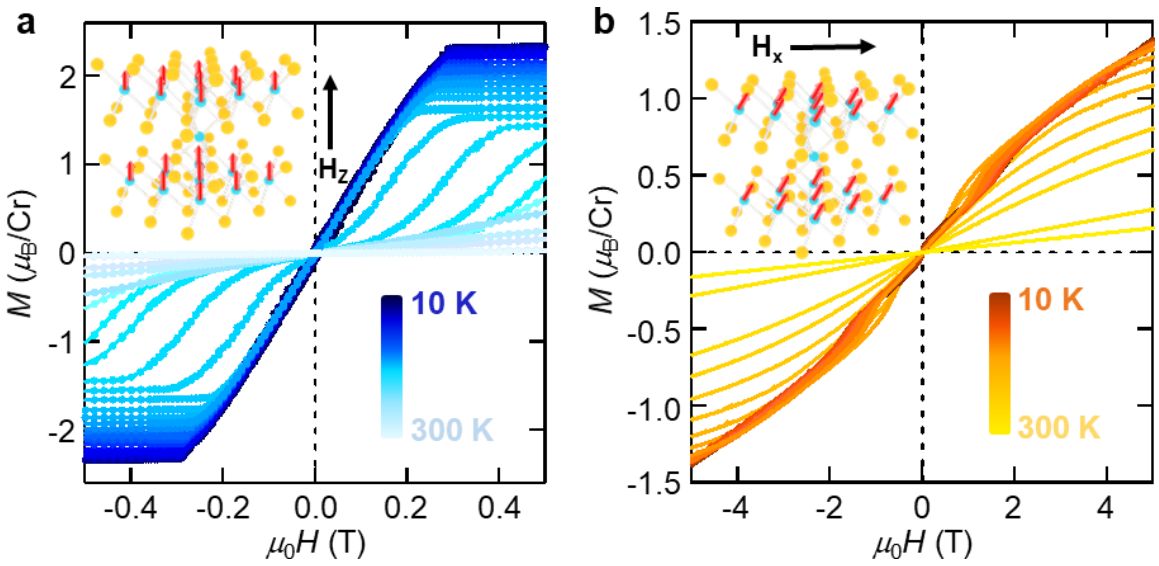

Figure S7. Out-pf-plane and in-plane magnetic characterization. a,b) Hysteresis loops at indicated temperatures with magnetic field along *c* axis (a) and *ab* plane (b), presenting a strong PMA. The heterostructures and spin configurations at representative magnetic fields are schematically shown as insets.

As shown in Figure S8, the blue line corresponds to an AFM phase transition. Since the applied field suppresses the AFM ordering, the transition temperature T_N decreases as the field increases. In the χ' contours, one can see two sharp peaks (red and blue), which correspond to the phase transitions at T_C and T_N, and a dome between 100 K and 150 K. We note that, the peak of the dome decreases in amplitude and shifts to lower temperature as the field increases. It is called Hopkinson maximum,[7] which arises from processes associated with coherent rotation of magnetic moments and motions of domain walls.

Interestingly, there is another kink feature in the out-of-plane *M*-*T* curves at a relatively low temperature (below 70 K), below which the magnetization decreases as the temperature falls at low fields (for example, 0.05 T). On the contrary, it changes into an upturn at relatively high fields (> 0.3 T). To rule out possibility of spin-glass, we did

frequency dependent AC susceptibility measurements. Figure S9 shows the χ' as a function of temperature under a magnetic field of 0.2 T with different frequencies. There are three kinks locating at around 66 K, 159 K and 180 K, all of which are frequency independent. It illustrates a long-range magnetic order rather than a spin-glass behavior with short range. Similar kinks were observed in the two-step magnetic ordering transitions in other vdW type FM materials, such as Fe_3GeTe_2,[8] which might be attributed from the formation of magnetic domains. Theoretical calculations and magnetic force microscopy (MFM) characterizations are needed to clarify the origin of this low-temperature kink in the future. In this work we will focus on the emergent AFM phase above the T_C.

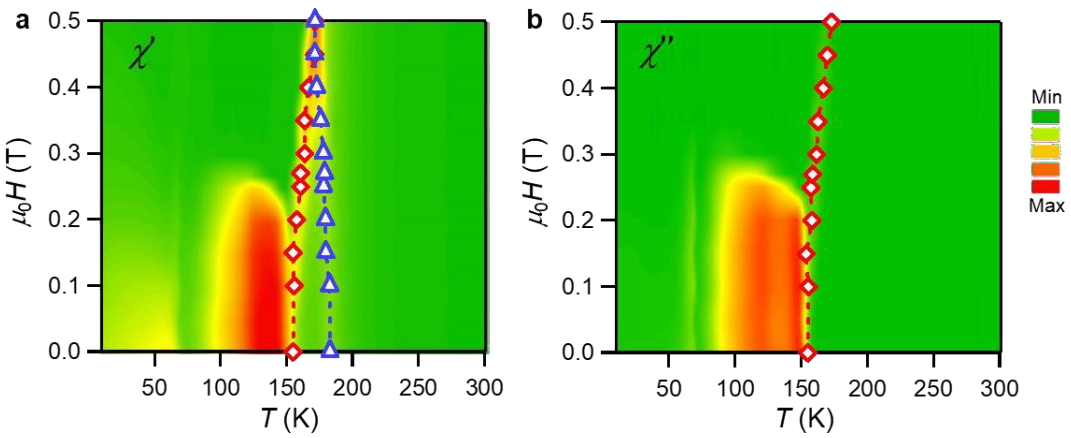

Figure S8. Phase diagram from AC magnetic susceptibility. a,b) Contour plots of χ' (a) and χ'' (b) measured at a frequency of 100 HZ. The phase boundaries determined from the susceptibility are illustrated by the symbols and dashed lines.

According to the band dispersions along M–Γ–K direction of freshly cleaved Cr_5Te_8, the electronic structure shows a metallic behavior with Te 5*p* bands crossing the Fermi level. Therefore, itinerant magnetic interactions also contribute to the magnetization

due to the interplay of conduction electrons, and its long-range nature can make the exchange coupling complicated.

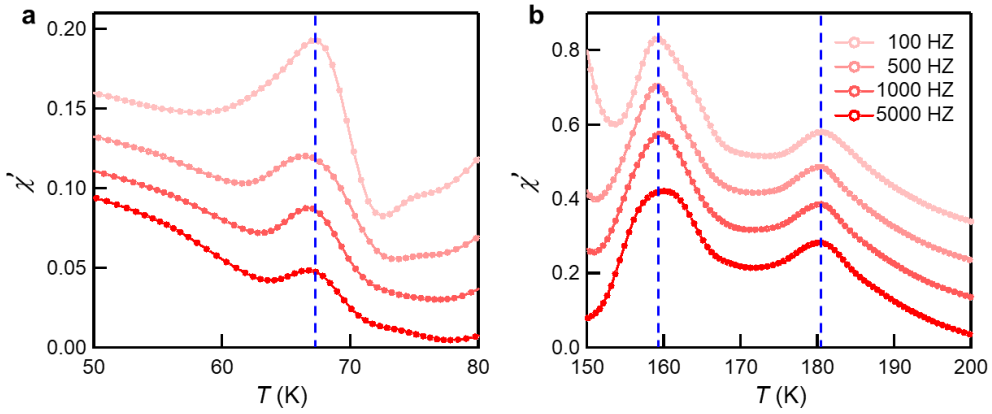

Figure S9. Frequency dependent AC susceptibility. a,b) χ' focusing on low temperature (a) and high temperature region (b), including T_C and T_N, at magnetic field of 0.2 T with frequencies from 100 HZ to 5000 HZ. χ' is frequency independent over the entire frequency range, despite the increased magnitudes.

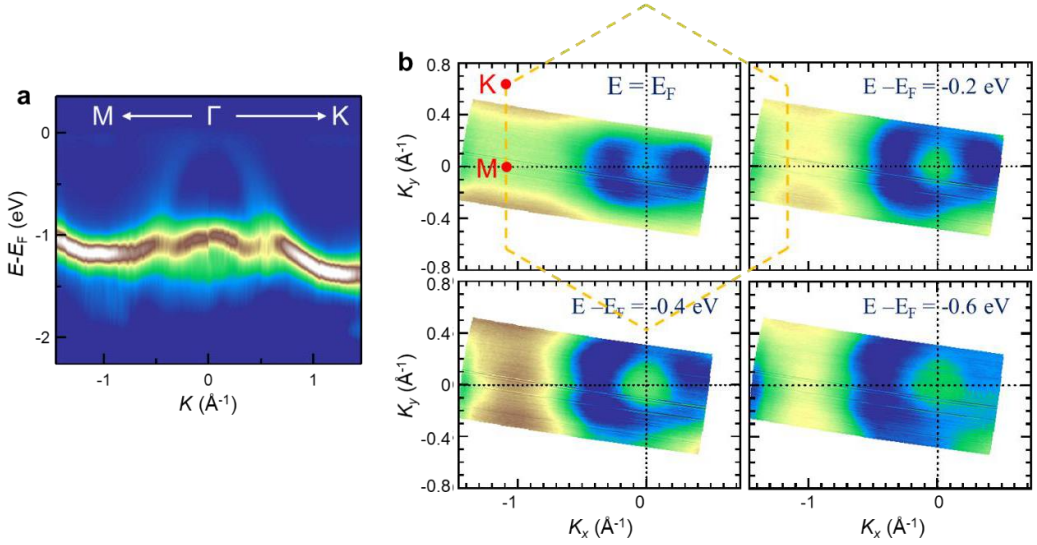

Figure S10. Band structure by ARPES characterization. a) Plots of valence-band dispersion along high symmetry direction M-Γ-K. b) ARPES-intensity mapping at Fermi level. The hexagonal Brillouin zone (yellow dashed lines) and high-symmetry points (green dots) are marked.

In addition, there are significant similarities between Cr_5Te_8 and $CrTe_2$ thin layers in the band dispersions, including hole-like valence bands at Γ point as well as electron pockets at M and K point.[9] It indicates that the electronic structure of Cr_5Te_8 is dominated by $CrTe_2$ layers, which is also confirmed by XMCD characterizations.

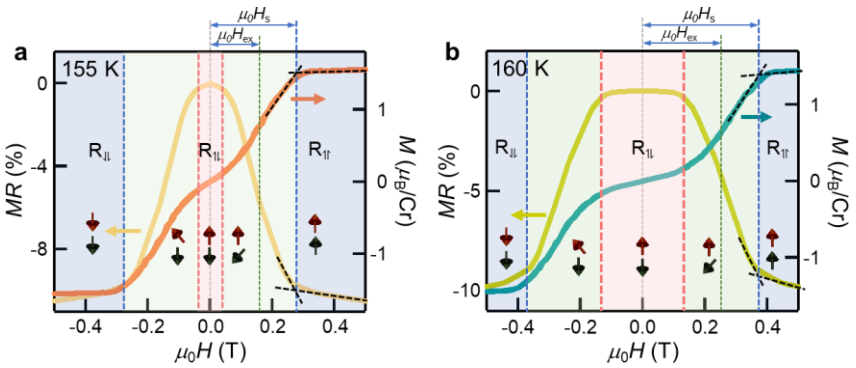

Figure S11. The definition of H_{ex}, H_s and GMR ratio. a,b) Field dependent MR and magnetic moment at 155 K (a) and 160 K (b). The H_s is defined as the crossing of the extensions (dash lines) to the linear parts of the curves. The GMR ratio is extracted from the corresponding MR value at H_s. The H_{ex} is defined as the mid-point between the end of the low-field plateau and the H_s.

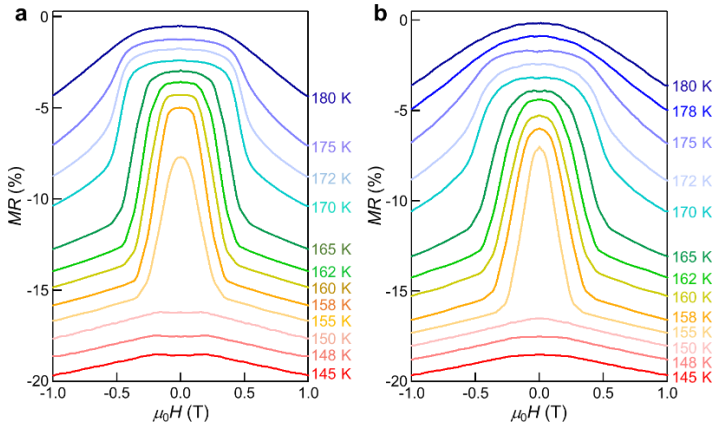

Figure S12. Additional two Cr_5Te_8 GMR devices. a,b) MR at temperature between 145 K and 180 K from two additional Cr_5Te_8 devices. Lines are shifted for clarity. We observe similar GMR effect in AFM phase region. The largest GMR value for sample (a) and (b) is 9.2% at 0.33 T and 9.5% at 0.35 T, respectively.

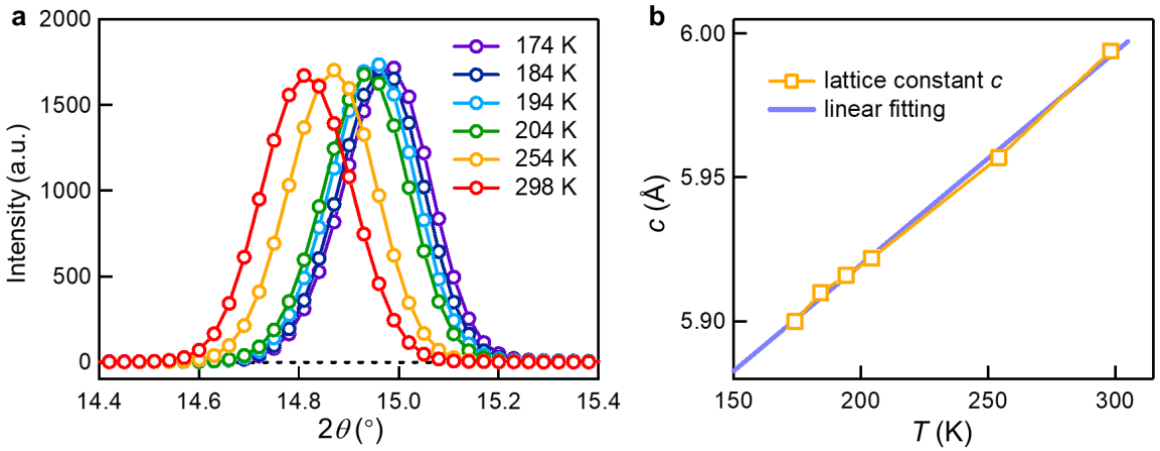

Figure S13. Temperature dependent diffraction peak of Cr_5Te_8 single crystal. a) A mono shift to higher angle as temperature decreases. b) A linear relationship between temperature and lattice constant calculated from diffraction peaks, suggesting that the magnetic phase transition cannot be attributed to the structural transition.

REFERENCES FOR SUPPORTING MATERIALS

[1] S. Lazar, Y. Shao, L. Gunawan, R. Nechache, A. Pignolet, G. A. Botton, Microsc. Microanal. 2010, 16, 416.

[2] L. D. Casto, A. J. Clune, M. O. Yokosuk, J. L. Musfeldt, T. J. Williams, H. L. Zhuang, M.W. Lin, K. Xiao, R. G. Hennig, B. C. Sales, J. Q. Yan, D. Mandrus, APL Mater. 2015, 3, 041515.

[3] C. Gong, L. Li, Z. Li, H. Ji, A. Stern, Y. Xia, T. Cao, W. Bao, C. Wang, Y. Wang, Z. Q. Qiu, R. J. Cava, S. G. Louie, J. Xia, X. Zhang, Nature 2017, 546, 265.

[4] B. Huang, G. Clark, E. Navarro-Moratalla, D. R. Klein, R. Cheng, K. L. Seyler, D. Zhong, E. Schmidgall, M. A. McGuire, D. H. Cobden, W. Yao, D. Xiao, P. Jarillo-Herrero, X. Xu, Nature 2017, 546, 270.

[5] L.-Z. Zhang, X.-D. He, A.-L. Zhang, Q.-L. Xiao, W.-L. Lu, F. Chen, Z. Feng, S. Cao, J. Zhang, J.-Y. Ge, APL Mater. 2020, 8, 031101.

[6] Y. Wang, J. Yan, J. Li, S. Wang, M. Song, J. Song, Z. Li, K. Chen, Y. Qin, L. Ling, H. Du, L. Cao, X. Luo, Y. Xiong, Y. Sun, Phys. Rev. B 2019, 100, 024434.

[7] S. H. Baek, K. Y. Choi, A. P. Reyes, P. L. Kuhns, N. J. Curro, V. Ramanchandran, N. S. Dalal, H. D. Zhou, C. R. Wiebe, J. Phys.: Condens. Matter 2008, 20, 135218.

[8] Z. Fei, B. Huang, P. Malinowski, W. Wang, T. Song, J. Sanchez, W. Yao, D. Xiao, X. Zhu, A. F. May, W. Wu, D. H. Cobden, J. H. Chu, X. Xu, Nat. Mater. 2018, 17, 778.

[9] X. Zhang, Q. Lu, W. Liu, W. Niu, J. Sun, J. Cook, M. Vaninger, P. F. Miceli, D. J. Singh, S.-W. Lian, T.-R. Chang, X. He, J. Du, L. He, R. Zhang, G. Bian, Y. Xu, Nat. Commun. 2021, 12, 2492.

SECTION

2. CONCLUSIONS

Multi-functional quantum materials are inevitable components for the technology advancement of spintronics and opto-electronics since their physical behaviors enhance the performance of modern devices. Ferromagnetic half-metals, Giant Magnetoresistants (GMR), non-oxide Transparent Conductors (TC), and Diluted Magnetic Semiconductors (DMS), are some of the most exemplary types of these multi-functional quantum materials that have been extensively investigated due to their interesting physical properties.

For this purpose, $Zn_{1-x}Cr_xTe$ polycrystalline samples with x = 0.00, 0.05, 0.10, 0.15, 0.18, and 0.20 have been synthesized and studied. The magnetic and transport properties measurements have revealed ferromagnetic semiconducting behavior for $x \leq 0.15$ but ferromagnetic conductivity for x = 0.18 and 0.20. Also, a level of 30–85 % optical transmittance has been observed in the visible range for different level of Cr dopants. The electrical transport inspired the further study of the polycrystalline or monocrystalline $Zn_{0.8}Cr_{0.2}Te$ for possible half-metallic ferromagnetism for the next research.

Further investigation about half metallicity in the monocrystalline $Zn_{0.8}Cr_{0.2}Te$ sample is carried out on the synergistic investigation of using ab-initio density functional calculations and neutron scattering measurements to elucidate the ground state magnetism. The results reveal important properties of $(Zn_{1-x}Cr_x)Te$ diluted magnetic semiconductors: first, long-range near room temperature (T_C ~ 290 K) ferromagnetism has been exhibited. The Cr concentration in the sample i.e., x = 0.2 and 0.15, does not influence the Curie

temperature for $(Zn_{1-x}Cr_x)Te$ single crystals. Also, the ferromagnetic alignment of moments on Zn/Cr sites along the diagonal direction in the a-c plane best describe the ground state ferromagnetic property. Moreover, the system depicts large, ordered moment, ~ 3.08 μB, which is possibly due to the induced magnetism between Zn/Cr and Te sites because of the orbital overlap, which is consistent with the DFT calculations. Furthermore, half-metallic behavior has been shown with the ab-initio calculations of $(Zn_{0.8}Cr_{0.2})Te$. Finally, a critical tendency to ferromagnetic ordering transition has been indicated, stemmed from the estimation of power law exponent of order parameter. Therefore, the results not only reveal the intrinsic magnetic properties of $(Zn_{1-x}Cr_x)Te$, independent of the substrate effect, but also inspire new ideas into the microscopic nature of magnetic ground state.

The synthesis and physical study of Cr_5Te_8 single crystals demonstrated an effective strategy to realize AFM interlayer exchange coupling through atomic-scale self-intercalation in crystal lattice. The antiparallel spins between adjacent $CrTe_2$ layers result in a GMR ratio and synthetic AFM phase in Cr_5Te_8 2D magnetic crystals, without requiring complex fabrication of heterostructures, which could be generalized to a wide range of 2D magnets to create potentially new mechanisms and properties. The experimental platform obtains the AFM interlayer exchange coupling, which give rise to new insights for fabricating 2D magnetic structures useful for spintronic purposes.

BIBLIOGRAPHY

[1] S. Hung, T.T. Wang, L.W. Chu, L.J. Chen, J. Phys. Chem. C 115, 15592 (2011).

[2] C. Battaglia, J. Escarré, K. Söderström, M. Charrière, M. Despeisse, F.J. Haug, C. Ballif, Nature Photonics 5, 535 (2011).

[3] C. Wang, J.C. Chien, K. Takei, T. Takahashi, J. Nah, A.M. Niknejad, A. Javey, Nano Lett. 12, 1527 (2012).

[4] B. Guo, Q. Yin, J. Zhou, W. Li, K. Zhang, and Y. Li, ACS Sustainable Chem. Eng. 7, 8206 (2019).

[5] E.Y. Tsymbal, Nature Materials 11, 12 (2012).

[6] S. D. Sarma, Nature Materials 2, 292 (2003).

[7] D. Chiba, M. Sawicki, Y. Nishitani, Y. Nakatani, F. Matsukura, H. Ohno, Nature 455, 515 (2008).

[8] J. Philip, A. Punnoose, B. I. Kim, K. M. Reddy, S. Layne, J. O. Holmes, B. Satpati, P. R. LeClair, T. S. Santos & J. S. Moodera, Nature Materials 5, 298 (2006).

[9] K. L. Chopra, S. Major, D. K. Pandya, Thin Solid Films 102, 1 (1983).

[10] A. M. Nazmul, S. Sugahara, M. Tanaka, Phys. Rev. B 67, 241308 (2003).

[11] X. Yu, T. J. Marks, and A. Facchetti, Nature Materials 15, 383 (2016).

[12] P. P. Edwards, A. Porch, M. O. Jones, D. V. Morgan, and R. M. Perks, Dalton Trans., 2995 (2004).

[13] J. F. Wager, D. A. Keszler, and R. E. Presley, Transparent Electronics, Springer (2008).

[14] K. Nomura, H. Ohta, K. Ueda, T. Kamiya, M. Hirano, and H. Hosono, J. Science 300, 1269 (2003).

[15] L. Castañeda, Materials Sciences and Applications 2, 1233 (2011).

[16] J. E. Medvedeva, D. B. Buchholz, and R. P. H. Chang, Journal of Adv. Electron. Mater 3, 1700082 (2017).

[17] D. S. Ginley and C. Bright, MRS Bulletin 25, 15 (2000).

[18] C. G. Granqvist, Applied Physics A 57, 19 (1993).

[19] A. Facchetti, and T. Marks, Transparent Electronics: From Synthesis to Applications, Wiley (2010).

[20] D. S. Ginley, H. Hosono, D. C. Paine, Handbook of Transparent Conductors, Springer (2010).

[21] K. Ellmer. Nature Photonics 6, 809 (2012).

[22] D. Soundararajan, D. Mangalaraj, D. Nataraj, L. Dorosinskii, K.H. Kim, Mat. Let. 87, 113 (2012).

[23] K. Kanazawa, S. Yoshida, H. Shigekawa, S. Kuroda, Sci. Technol. Adv. Mater. 16, 015002 (2015).

[24] K. Sato, H. K. Yoshida, Semicond. Sci. Technol. 17, 367 (2002).

[25] K. Onodera, T. Masumoto, M. Kimura, Electronics Lett. 30, 1954 (1994).

[26] K. Sato, H. K. Yoshida, Jpn. J. Appl. Phys. 40, 651 (2001).

[27] W. Mac, A. Twardowski, M. Demianiuk, Phys. Rev. B 54, 5528 (1996).

[28] J. Blinowski, P. Kacman, J. A. Majewski, Crystal Growth 159, 972 (1996).

[29] L. Zhao, B. Zhang, Q. Pang, X. Zhang, W. Ge, J. Wanga, Appl. Phys. Lett. 89, 092111 (2006).

[30] Q. Wang, Q. Sun, P. Jena, Y. Kawazoe, Applied Physics 97, 043904 (2005).

[31] K. Kanazawa, T. Nishimura, S. Yoshida, H. Shigekawa, S. Kuroda, Nanoscale 6, 14667 (2014).

[32] N. Ozaki, I. Okabayashi, T. Kumekawa, N. Nishizawa, S. Marcet, S. Kuroda, K. Takita, Applied Physics Letters 87, 192116 (2005).

[33] H. Saito, V. Zayets, S. Yamagata, K. Ando, Journal of Applied Physics 93, 6796 (2003).

[34] S. Amari, S. Méçabih, B. Abbar, B. Bouhafs, Comput. Mater. Sci. 50, 2785 (2011).

[35] S. M. Yakout, Jour. of Superconductivity and Novel Magnetism 33, 2557 (2020).

[36] J. M. D. Coey and S. Sanvito, Jour. Phys. D: Appl. Phys., 37, 988 (2004).

[37] K. M. Krishnan, Fundamentals and Applications of Magnetic Materials, Oxford University Press (2016).

[38] https://chem.libretexts.org/Bookshelves/Analytical_Chemistry.html. Feb. 2023.

[39] J. Tauc, R. Grigorovici, A. Vancu, Phys. Stat. Sol. 15, 627 (1966).

[40] T. Heitmann and W. Montfrooij, Practical Neutron Scattering at a Steady State Source, Mizzou Media Press (2012).

[41] R. Woods-Robinson, Y. Han, H. Zhang, T. Ablekim, I. Khan, K. A. Persson, and A. Zakutayev, Chemical Reviews 120, 4007 (2020).

VITA

Ali Sarikhani was born in Varamin, Iran. He completed his high school education at Dr. Hesabi Top High School, Varamin, Iran. He earned a bachelor of science degree in Physics from University of Tehran (ranked 1st university in Iran) in June 2018. He performed experimental nanophysics research under supervision of Dr. Yaser Abdi in University of Tehran.

In 2018, he moved to the United States to pursue a Ph.D. in physics in Rolla, MO at the Missouri University of Science and Technology. He joined Dr. Yew San Hor's research group in 2018 in collaboration with Materials Research Center. Under the supervision of Dr. Hor, he performed experimental condensed matter research and materials physics to have explored the synthesis and physical measurements of novel quantum materials. He successfully defended his Ph.D. dissertation in March 2023. He received his Ph.D. in Physics from Missouri S&T in May 2023.